Theoretical approach towards accurate molecular interactions with low-dimensional substrates

Yasmine Shauket Al-Hamdani

A dissertation submitted for the degree of

Engineering Doctorate

Department of Chemistry

University College London

December 2016

Declaration

I, Yasmine Shauket Al-Hamdani, confirm that the work presented in this thesis is my own. Where information has been derived from other sources, I confirm that this has been indicated in the thesis. The work contains nothing which is the outcome of work done in collaboration except where specifically indicated in the text.

Yasmine Shauket Al-Hamdani

December 2016

Acknowledgements

Alas, my time at UCL has come to an end after some wonderful years. I have had the pleasure of working with my supervisor, Angelos Michaelides. I could not be more grateful for the guidance and care that he has provided during my PhD. I also extend my gratitude to my co-supervisors Dario Alfè and Anatole von Lilienfeld, who have advised me and given me their invaluable insights throughout my PhD. I would also like to thank Mariana Rossi, Alexander Tkatchenko, Georg Kresse, Andreas Grüneis, Ming Ma, and Laurent Joly for helpful discussions and collaborations. In addition, the work in this thesis would not have been possible without the generous computational resources provided by Argonne National Lab on MIRA, Oak Ridge National Lab on TITAN, and the LCN services at UCL.

I truly value my time in the ICE group and thank all members, past and present, for the great environment in which we work. In particular, I would like to thank my friends and peers: Stephen Cox, Gabriella Graziano, Gabriele Tocci, and Erlend Davidson, for offering their support when I first joined the group. In addition, I have made life-long friends here, perhaps too many to name, but I cherish them and thank them dearly for making the last few years of my life the happiest.

Finally, I dedicate this work to my mother, Dr. Alia Al-Hamdani, and my father, Dr. Ali Shauket. They have made countless sacrifices in order for me to have opportunities, and have raised me to value academia as one. I am eternally grateful for their never-ending love and encouragement.

Contents

List of Figures

List of Tables

Publications

Parts of this dissertation have been published, or submitted for publication, as follows.

Chapter 3: Yasmine S. Al-Hamdani, Dario Alfè, O. Anatole von Lilienfeld, and Angelos Michaelides, *"Water on BN doped benzene: A hard test for exchange-correlation functionals and the impact of exact exchange on weak binding."*, J. Chem. Phys. 141, 18C530 (2014)

Chapter 4: Yasmine S. Al-Hamdani, Ming Ma, Dario Alfè, O. Anatole von Lilienfeld, and Angelos Michaelides, *"Water on hexagonal boron nitride from diffusion Monte Carlo"*, J. Chem. Phys. 142, 181101 (2015)

Chapter 7: Yasmine S. Al-Hamdani, Dario Alfè, O. Anatole von Lilienfeld, and Angelos Michaelides, *"Tuning dissociation using isoelectronically doped graphene and hexagonal boron nitride: water and other small molecules."*, J. Chem. Phys. 144, 154706 (2016)

Chapter 1

Introduction

Whether it is to convert heavy oil into petroleum, enhancing semi-conductor performance, or to develop biomaterials in medicine: molecular adsorption on surfaces clearly has a major role in a remarkable number of physical processes, both natural and man-made. Understanding adsorption helps us to understand our environment and to create better and more advanced technologies for the future. For instance, adsorption plays a critical role in heterogeneous catalysis - a process that we heavily rely on for manufacturing ammonia, antifreeze, synthetic rubbers, and plastics amongst many others [1]. The knowledge of adsorption energies and preferences for different chemicals on surfaces allowed us to develop high-impact 3-way catalytic converters that have helped to counteract environmental pollution immensely [1].

Amongst the many materials being studied for chemical applications, low dimensional materials like graphene and hexagonal boron nitride (h-BN) stand out in terms of versatility and novelty, displaying a range of exotic structural and electronic properties. Properties of graphene and h-BN manifest themselves in various important applications such as desalination [2], water purification [3, 4], energy storage [5], energy generation [6–10] and catalysis [11–13].

For almost any concievable application of a material, it is important to understand the interactions of water on the exposed surfaces. Water is indeed ubiquitous and in the absence of an ultra high vacuum (UHV), materials inevitably come into contact with water molecules, which can have a substantial impact. For example, sizeable voltages have been measured across graphene sheets and nanotubes [6–9] due to the formation of water salinity gradients. In BN nanotubes, Siria *et al.* demonstrated that water flowing osmotically through the tube produces remarkably large electric currents [10]. This was attributed to the possible dissoci-

ation and adsorption of water on the interior of the nanotube which influences the dynamics inside the nanotube. Such experimental observations are interesting, but are not yet completely understood on a molecular level. Major gaps in our understanding of these materials still exist, and it appears that for the full potential of such vdW materials to be realised on an industrial scale, a great deal of fundamental understanding should be established [14–16].

In this thesis, two important areas are addressed to some degree. First, the adsorption of water on carbon and boron nitride based low dimensional substrates. Adsorption on these surfaces is especially intriguing because vdW materials exhibit peculiar long-range correlation interactions compared to bulk solids or molecules [17], that are challenging to accurately predict. By seeking accurate theoretical predictions of physisorption interactions, we also assess the predictive power of various computational methods for molecular adsorption. Second, there is a great deal more to be understood about how doping in graphene and h-BN materials alters their interaction with molecules. Furthermore, this is motivated by the emergence of experimental routes to produce hybrid composites of h-BN and graphene [18, 19], with high levels of control being reported on the nanometre scale. Therefore, it is timely to develop our understanding of adsorption at doped graphene and h-BN surfaces on a molecular level. Although theoretical approaches are used in this thesis to gain insights at the molecular level, it is important to consider the experimental context.

Studying adsorption in the laboratory requires state-of-the-art surface sensitive techniques that can provide us with information on adsorption configurations, sites, and energies. This is no trivial task, and many systems at the frontiers of materials design lack reference adsorption data from experiments. Reference information is particularly important for understanding the fundamental interactions of adsorbates at surfaces, and to use that knowledge-base to further technologies. Furthermore, reference values are essential for improving theoretical models that allow us to predict the properties of materials and to gain atomistic level understanding. It has been emphasized by Somorjai *et al.* [20], that combining experiments with theoretical calculations certainly helps bridge the gaps in our understanding, and paves the way for more guided research.

Experimentally, adsorption energies have been derived for thousands of materials, usually from adsorption isotherms, but accurate adsorption energies on clean surfaces are much less common. Surface science plays the role of providing the all-important surface structures

that are needed to establish adsorption energies for a well-defined system. This entails the use of ultra-high vacuums for maintaining ultra-clean surfaces and examining them using: scanning tunnelling microscopy (STM); low energy electron diffraction (LEED); reflection absorption infra-red spectroscopy (RAIRS); and electron energy loss spectroscopy (EELS). By establishing the surface structure we learn which surfaces are present and can perform precise experiments on the faces we are interested in.

Temperature programmed desorption (TPD) is a widely used technique for measuring the adsorption energy on a clean surface and works by monitoring the desorbed molecules using a mass spectrometer, as a function of the temperature. TPD spectra tell us about: i) number of adsorbed species ii) binding energy of species and iii) reaction products. As a result, TPD is a very useful technique, but it does contain uncertainties. Firstly, it is the desorption temperature, not the adsorption energy, that is measured. A desorption energy is inferred from the measured temperature, and the difference between that energy and the adsorption energy is the activation energy for adsorption. Normally, it is assumed that the barrier for adsorption is low and therefore the desorption energy is equal to the sum of the adsorption enthalpy and $^1/_2$RT, where T is the average temperature of the sample. Secondly, the prefactor related to the rate of desorption is usually assigned an assumed value (related to the vibrational frequency of the surface-molecule vibration) for use within the Redhead formula. Recently, Campbell and Sellers [21] have discovered a more reliable way to derive the prefactor by making use of the direct relation between the prefactor and the entropy of the transition state of the adsorbed species (derived from statistical mechanics). In this way, TPD adsorption energies from previous years have been systematically corrected by Campbell and Sellers [22].

Alternatively, single crystal adsorption calorimetry (SCAC) is an experimental technique [22, 23] that rather elegantly measures the heat transfer on adsorption of molecules on a single crystal surface. Without making assumptions about prefactors, or taking differentials of functions, the direct heat of adsorption is obtained from the temperatures of the samples and the heat transfer. Until now, this technique has mostly been used for the adsorption energies of molecules like water and carbon monoxide on metal and metal oxide surfaces [23, 24]. Unfortunately, the process of obtaining the adsorption energy of a molecule on a surface involves preparing a clean surface and undertaking a careful calibration of the setup

for each different material being studied. This precise but painstaking approach can amount to a great deal of time ($\sim$ 1 year).

In contrast to experiments, computational methods are more easily applied to materials that are clean and defect-free than materials that are not. Thus, computational techniques can provide key information for pristine systems especially. The main techniques within *ab initio* methods are: quantum chemistry, density functional theory (DFT) [25, 26], the random phase approximation (RPA) and quantum Monte Carlo (QMC). DFT is the most efficient in theory because total energies of a system, in principle, are calculated directly from the electron density – a single, three-dimensional function. This is considerably simpler than solving the Schrödinger equation using many-body wavefunctions as in quantum chemistry and QMC. Another direct advantage is the ability to apply DFT fairly efficiently to periodic systems (e.g. crystalline surfaces), which are otherwise very expensive to calculate using quantum chemistry, the RPA or QMC. However, a well-known and rather important limitation in practical DFT is the unknown form of the exchange-correlation (xc) functional, and the problems that arise from it.

The xc functional has been approximated in a variety of ways, including the local density approximation (LDA), which is the first and simplest; the generalised gradient approximation (GGA) and also hybrid functionals, which contain a portion of exact exchange based on Hartree-Fock (HF) theory. However, because xc functionals are approximate, practical DFT suffers from a number of problems, perhaps most notably the delocalisation error. This is also referred to as self-interaction error and in general, leads to more diffuse orbitals and underestimated band gaps. The Hubbard U [27] is a method that attempts to correct the delocalisation error by including a penalty for the formation of diffuse orbitals. The U parameter can be chosen to match experimental data or computed from first principles using the RPA [28].

Even so, DFT has been a powerhouse within *ab initio* methods over the last decades [29, 30]. An example of DFT success is its use in high throughput screening of materials. Whether it is to search for better electrolytes in batteries or to find the most stable crystal polymorphs for drug molecules, efficient computational high throughput screening allows important candidate systems to be identified. Greeley *et al.* made one such discovery by screening through hundreds of binary surface alloys and predicting that BiPt is a more active catalyst

than traditionally used pure Pt for the hydrogen evolution reaction [31]. Indeed, this was then verified experimentally, demonstrating how modelling and experiments are complementary.

Nonetheless, there are numerous systems where DFT xc functionals fail to provide adequate description of the true underlying physics. Importantly, none of the aforementioned xc functionals include long-range correlation, and hence vdW interactions are completely neglected. Although vdW interactions are typically weak, their role in adsorption is often considerable. The gecko famously uses weak vdW interactions for adhesion to defeat gravity and climb walls. Recognising the critical role of vdW interactions in certain systems, a number of different vdW-functionals and dispersion corrections [32–42] have been developed over the years to try to account for some of the missing vdW interactions. Several reviews discuss the performance of different vdW DFT methods [43–47]. Generally however, a vast amount of disagreement can be found amongst vdW functionals.

A key challenge lies in the ability to capture small energy differences – on the order of a few meV – that can have drastic effects on the structure of a complex system. For example, water has several distinct ice polymorphs that have lattice energies within 35 meV/H_2O of each other [48–53]. Likewise for water clusters, most notably the water hexamer, there are several isomers that have energies within just 5 meV/H_2O [52, 54, 55]. Furthermore, in biological applications there can be numerous shallow energy minima with different conformations. Particularly for complex organic systems, predicting the exact lowest energy conformation is crucial to determine the crystal structure of drugs [56, 57], and the mechanisms by which proteins function [58]. The development of better xc functionals is paramount in enabling practical DFT to be a reliable and consistent predictive method. For this, we need accurate reference values for benchmarks, and these we can obtain from high-level (though expensive) methods such as the RPA, QMC, second order Møller-Plesset (MP2) theory, and coupled cluster with single, double and perturbative triple excitations (CCSD(T)).

These *ab initio* methods have had numerous successes including for example, the RPA prediction of the adsorption site for CO on metal surfaces [59] where GGAs within DFT fail. It has also been demonstrated that the RPA provides a marked improvement over DFT predictions of bulk properties, such as lattice constants [60, 61] and bulk moduli [61]. Another example is the QMC adsorption energy of water on LiH crystal [62] - a material that spontaneously oxidises in moist air, making any experimental measurement extremely difficult.

Accurately calculated reference adsorption energies are informative for experimentalists and essential to developers of computational methods.

Ideally, the aformentioned reference computational methods produce the same predictions but this has mostly been demonstrated for interactions between small molecules only. The main challenge to computing surface adsorption energies has been the modelling of large unit cells that are more expensive, sometimes prohibitively so, to compute accurately. However, thanks to the surge in computing power and even more so, great improvements in codes, surface adsorption problems have become increasingly accessible in recent years [59, 62–71]. Water adsorption on graphene is an exemplary case that has been computed with the RPA, QMC [63] and CCSD(T) [64]. However, the reported adsorption energies span a range of up to 40%; likely due to a number of limitations and approximations that have not yet been quantified. In addition, large unit cells (typically with more than 50 atoms) are needed to study molecular adsorption on surfaces computationally, for which some of the benchmark methods become intractable.

In essence, the accurate determination of energies for solids and surfaces with electronic structure methods is one of the most interesting, challenging, and exciting areas of the physical sciences right now. Accurate methods are needed to make truly quantitative predictions and to accurately inform experimentalists. A significant part of this thesis presents work that is aimed at establishing accurate benchmarks of molecular interactions on substrates composed of carbon, BN, and mixtures of them. In Chapters 3, 4, 5 and 6, physisorption interactions of water are the main focus, with a mind to provide accurate reference information from QMC and insight into the predictive power of various *ab initio* methods. In Chapter 7 we use conventional DFT methods to study the dissociative adsorption of water and other industrially relevant molecules such as hydrogen, methane, and methanol, on graphene and h-BN. In addition, we investigate the trends in the dissociative adsorption energies as a function of isoelectronic doping in these surfaces. Later in Chapter 8, we demonstrate how alchemical derivatives can be used to efficiently screen through different doping topologies to identify favourable dissociative adsorption sites. We conclude the thesis with a brief outlook and summerise the key findings in this work.

Chapter 2

Theoretical background

The work that is laid out in this thesis is aimed primarily at understanding adsorption interactions at a molecular level and making careful assessments of the tools for doing so. Where experimental reference data is scarce, this is made possible through the great progress that has been made in the field of quantum mechanics and computational chemistry. A theoretical context is given in this chapter, beginning with the Schrödinger equation and drawing on the relevant theorems, developments, and approximations that have been made since, to find practical solutions to the many-body wavefunction.

2.1 Quantum mechanics

First, the non-relativistic Hamiltonian (in atomic units) for a system containing N_n nuclei and N_e electrons is given by,

$$\begin{aligned}\hat{H} = -\frac{1}{2}\sum_{i}^{N_e}\nabla_i^2 - \frac{1}{2}\sum_{A}^{N_n}\frac{1}{M_A}\nabla_A^2 - \sum_{i,A}^{N_e,N_n}\frac{Z_A}{|r_i - R_A|} \\ + \sum_{i<j}^{N_e}\frac{1}{|r_i - r_j|} + \sum_{A<B}^{N_n}\frac{Z_A Z_B}{|R_A - R_B|},\end{aligned} \tag{2.1}$$

where indices i, j run over electrons and A, B run over nuclei, such that $i \neq j$ and $A \neq B$. M is the mass of the nucleus, Z is its charge, and r and R are the positions of the electrons and nuclei, respectively. The first two terms on the right-hand side are the expressions for the kinetic energy of the electrons and nuclei, respectively. The third term is the attractive

electrostatic interaction between electrons and nuclei whilst the fourth term describes the electrostatic interaction between electrons themselves. The final term is the electrostatic interaction between nuclei.

In wavefunction based methods, the aim is to solve the Schrödinger equation,

$$\hat{H} \left|\Psi(\mathbf{r}, \mathbf{R}, t)\right\rangle = i\hbar \frac{\partial}{\partial t} \left|\Psi(\mathbf{r}, \mathbf{R}, t)\right\rangle \tag{2.2}$$

where $\Psi(r, R, t)$ is the wavefunction defined by the positions of electrons and ions, and time (t). Equation 2.2 describes the time evolution of a quantum mechanical system. The time evolution of a system is indeed important for dynamic properties but, in general, the time dimension is not necessary to evaluate the energy of a system. As such, the solution is often sought for the time-independent Schödinger equation instead,

$$\hat{H}\Psi(\mathbf{r}, \mathbf{R}) = E\Psi(\mathbf{r}, \mathbf{R}). \tag{2.3}$$

This is an eigenvalue equation wherein the eigenvalues correspond to the energies of the eigenstates of the Hamiltonian. For a given system, the lowest energy arrangement of electrons and ions forms the ground state wavefunction, $\Psi_0(\mathbf{r}, \mathbf{R})$. By the Born rule, the probability density of the particles is $\rho(\mathbf{r}, \mathbf{R}) = \Psi^*(\mathbf{r}, \mathbf{R})\Psi(\mathbf{r}, \mathbf{R})$.

Only the simplest of systems can be solved analytically because crucially, electrons are indistinguishable and interact with each other through the fourth term in Eq. 2.1. This is a two-body term in the Hamiltonian that makes any eigenfunction not factorisable in terms of one-body solutions. As such, a many-body solution to the wavefunction is needed and this poses a challenge computationally in terms of time and memory. A year after Schrödinger's equation was revealed in 1926, there emerged two important paths for solving it: the quantum chemical route starting with Hartree-Fock (HF) theory [72, 73] and separately, the method of using the electron density, beginning with the Thomas-Fermi model [74, 75]. Quantum chemical methods are described briefly in Section 2.2 and density functional theory is discussed in Section 2.3. In addition, a powerful method that is used to solve for the many-body wavefunction, namely quantum Monte Carlo, is described in Section 2.4. First, the Born-Oppenheimer approximation is an underlying approximation in all of the calculations

that have been undertaken as part of this work and is discussed in the following section.

2.1.1 Born-Oppenheimer approximation

Reducing the number of degrees of freedom ($3N_e + 3N_n$) is the first step towards simplifying the problem. This is done by recognising that electrons are (> 3) orders of magnitude lighter than nuclei and hence the electrons can be considered to be moving instantaneously with respect to the motion of nuclei [76]. Thus the nuclear degrees of freedom can be treated separately such that,

$$\Psi(\mathbf{r}, \mathbf{R}) = \Psi^e(\mathbf{r}, \mathbf{R})\Psi^n(\mathbf{R}), \tag{2.4}$$

where $\Psi^e(\mathbf{r}, \mathbf{R})$ is the electronic wavefunction for which the nuclear coordinates, R, are just classical parameters. The corresponding electronic Schrödinger equation can be expressed as,

$$\left(-\frac{1}{2}\sum_{i}^{N_e} \nabla_i^2 + \sum_{i,A}^{N_e,N_n} \frac{Z_A}{|r_i - R_A|} + \sum_{i,j}^{N_e,N_e} \frac{1}{|r_i - r_j|} \right) \Psi^e(\mathbf{r}, \mathbf{R}) = E^{el}(\mathbf{R})\Psi^e(\mathbf{r}, \mathbf{R}), \tag{2.5}$$

where $E^{el}(\mathbf{r})$ is the electronic energy that constitutes a potential in which nuclei move,

$$\left(-\frac{1}{2}\sum_{A}^{N_n} \frac{1}{M_A}\nabla_A^2 + E^{el}(\mathbf{R}) + \sum_{A,B}^{N_n,N_n} \frac{Z_A Z_B}{|R_A - R_B|} \right) \Psi^n(\mathbf{R}) = E^{nuc}\Psi^n(\mathbf{R}), \tag{2.6}$$

where E^{nuc} is the nuclear energy for a given electronic potential. In ground state Born-Oppenheimer dynamics, the nuclei are treated like classical particles moving in an electronic potential given by the energy of the electrons.

There are important instances where the Born-Oppenheimer approximation is not suitable. For example when the mass of the nuclei is small, they behave less classically. Such quantum nuclear effects (as they are often referred to) are more prevalent at low temperatures at which the kinetic energy is lower and the nuclei are more delocalised, giving rise to proton sharing and tunelling phenomena [77]. The Born-Oppenheimer approximation can also fail when calculating certain properties of systems with small energy gaps between the ground state and the excitated states [78].

2.2 Quantum chemistry

The electronic wavefunction we have introduced thus far is many-body in nature, *i.e.* it consists of N_e interacting electrons and solving the electronic Schrödinger equation would therefore involve $3N_e$ variables. Drawing on the principle that electrons occupy discrete states or *orbitals* within a system, Hartree proposed an important approximation: to treat each electron as occupying its own independent spin-orbital whereby the total wavefunction is given by the product of single-particle, orthogonal orbitals,

$$\Psi(\{r_i\}) \approx \phi_1(r_1)\phi_2(r_2)...\phi_{N_e}(r_{N_e}), \tag{2.7}$$

where $\phi_1(r_1)$ indicates a single-particle spin orbital occupied by electron 1 with spatial coordinate r_1. However, Eq. 2.7 does not obey Pauli's exclusion principle according to which the wavefunction must be antisymmetric with respect to the exchange of fermionic particles. Instead, Slater determinants are used as a viable means of representing a wavefunction composed of single-particle orbitals,

$$\Psi(\{r_i\}) \approx \frac{1}{\sqrt{N_e!}} \begin{vmatrix} \phi_1(r_1) & \phi_2(r_1) & \cdots & \phi_{N_e}(r_1) \\ \phi_1(r_2) & \phi_2(r_2) & \cdots & \phi_{N_e}(r_2) \\ \vdots & \vdots & \ddots & \vdots \\ \phi_1(r_{N_e}) & \phi_2(r_{N_e}) & \cdots & \phi_{N_e}(r_{N_e}) \end{vmatrix}. \tag{2.8}$$

The advantage of expressing the HF wavefunction as a Slater determinant is that Pauli's exclusion principle is fulfilled. In applying the electronic Schrödinger equation to the HF wavefunction, the orthogonality of orbitals means that only terms with identical Hartree products on both sides of an operator are non-zero. As a result, the action of single-particle operators given by the first two terms in Eq. 2.5, is simply the sum of the expectation values of the single-particle states,

$$\sum_i^{N_e} \langle \phi_i(r_i)| -\frac{1}{2}\nabla_i^2 + V_i^{ext} |\phi_i(r_i)\rangle \,, \tag{2.9}$$

leaving aside only the two-particle operator that describes the interaction between two electrons. The action of the Coulomb operator with the Slater determinant gives rise to two

terms,

$$\sum_{i,j}^{N_e} \langle \phi_i(r_i)\phi_j(r_j)| \frac{1}{|r_i - r_j|} |\phi_j(r_j)\phi_i(r_i)\rangle \,, \tag{2.10}$$

which is the Coulomb interaction between electrons in single-particle states and is known as the Hartree term. In addition, because of the antisymmetry of the wavefunction there is an exchange term,

$$-\sum_{i,j}^{N_e} \langle \phi_i(r_i)\phi_j(r_j)| \frac{1}{|r_i - r_j|} |\phi_j(r_i)\phi_i(r_j)\rangle \,. \tag{2.11}$$

The operators that produce the expectation values in Eqs. 2.9, 2.10, and 2.11, are known collectively as the Fock operator when acting on a single-particle state.

Let us comment on a few important features of HF theory. First, note that for $i = j$, the Hartree and exchange terms are equal and opposite therefore cancelling out. This is physically understood as electrons interacting with all other electrons but not themselves. Second, HF theory is a mean field approach because each electron interacts with an average charge distribution of all other electrons. As a consequence, this theory neglects completely the interaction that occurs because of the instantaneous correlated motion of electrons. This is known as dynamic correlation and although it is only a small part of the total energy, it can have a significant impact on energy differences such as adsorption energies. Moreover, the HF wavefunction as represented by a single Slater determinant is not always sufficient to describe the total wavefunction for molecules with near degenerate states or for stretched bonds. The error arising from such a situation is referred to as static correlation.

We should keep in mind that electronic correlation is still a form of Coulomb interaction and arises separately here, solely, due to the mean field treatment of the many-body wavefunction. Indeed, whilst HF theory is a useful starting point, its accuracy is severely limited by the lack of electronic correlation. Various post-HF methods have been introduced since to address this shortfall.

2.2.1 Post Hartree-Fock methods

The conceptually simplest improvement upon HF theory is to use more than a single Slater determinant, *i.e.* using a linear combination of the HF wavefunction and all determinants corresponding to its excited configurations. Such a procedure is known as full configuration

interaction (CI) and in the limit of a complete basis set representing the one-electron states, this theory is exact. That is because every possible electronic configuration is explicit in the full-CI wavefunction and thus every form of Coulombic interaction is accounted for. Unfortunately full-CI scales factorially and in practice it is not feasible to include all possible excitations or to reach a complete basis representation. Instead, truncation levels are introduced to only include certain orders of excitations such as single, double, triple *etc.* Whilst this reduces the scaling of the method to $N^6 - N^8$, with N being the number of basis functions representing the electrons, it is no longer size-consistent. In other words, the energy of two fragments calculated separately does not equate to the energy of the fragments far apart. More promisingly, a novel method has been developed in recent years to achieve full-CI accuracy, known as full-CI quantum Monte Carlo (FCIQMC). With this method, a parallelisable Monte Carlo algorithm is used to explore Hilbert space and determine the relevant Slater determinants and their weights in the overall wavefunction [79]. FCIQMC is more efficient but is still some way from being applied to systems with large numbers of atoms. To date, FCIQMC has been used to calculate dissociation energies diatomics from the first row of the periodic table [80] and to calculate the ionization potentials of first row transition metals [81].

Another method known as coupled cluster theory, also accounts for correlation energy by including determinants of higher excitations,

$$\Psi_{cc} = e^T \Psi_{HF} = (1 + T + \frac{1}{2!}T^2 + \frac{1}{3!}T^3 + ...)\Psi_{HF}, \tag{2.12}$$

where Ψ_{cc} is the coupled cluster wavefunction and T denotes a series of connected operators which project out excitations of the Slater determinant, Ψ_{HF}. Like CI, the inclusion of more determinants can quickly make the method intractable, already scaling as N^6 when single and double excitation operators are included. Let us emphasize that the Taylor expansion of an excitation operator in Eq. 2.12 produces higher order excitations. For example, if T is a single and double excitation operator, then the T^2 and T^3 terms produce higher order *disconnected* quadruples, hextuples and so on. Crucially however, it is a size-extensive method even when truncated, and is often used for calculating accurate energy differences. Coupled cluster with single, double and perturbative triple excitations (CCSD(T)) is often used for benchmark interaction energies. In CCSD(T) the perturbed triple excitations are treated approximately

through the single and double excitation operators. Helgaker *et al.* have shown that this tends to overestimate the effect of triple excitations by roughly the same amount as the underestimation from not using the quadruple excitation operator, leading to a favourable error cancellation. Even so, CCSD(T) scales as N^7 and without further approximations, it is typically applied to systems with less than 30 atoms. Shortly we will discuss some increasingly successful ways to avoid the unfavourable scaling in wavefunction based methods, but first we must mention another widely used quantum chemical theory.

Better scaling is achieved with Møller-Plesset theory but with less accuracy and without adhering to the variation principle. This theory is based on Rayleigh-Schrödinger perturbation theory and when taken to the 2^{nd} order (MP2) scales as N^5. MP2 introduces the following correction to the HF energy,

$$E^{MP2} = \frac{1}{4} \sum_{i,j,a,b} \frac{[\langle \phi_i \phi_j | \phi_a \phi_b \rangle - \langle \phi_i \phi_j | \phi_b \phi_a \rangle]^2}{\epsilon_i + \epsilon_j - \epsilon_a - \epsilon_b}, \tag{2.13}$$

where ϕ_a, ϕ_b are unoccupied virtual orbitals and ϕ_i, ϕ_j are occupied orbitals, and ϵ indicates the corresponding orbital energies. One can see that MP2 theory introduces correlation from double excitations only. In fact by Brillouin's theorem, the effect of single excitations vanishes within this perturbation method.

One useful approximation that is often made in practice is the correction of a good quality MP2 energy, *i.e.* with a complete basis set (CBS) extrapolation, by CCSD(T) with a smaller and more affordable basis set,

$$E^{\Delta CCSD(T)} = E^{MP2@CBS} + (E^{CCSD(T)} - E^{MP2}). \tag{2.14}$$

Here, $E^{CCSD(T)}$ and E^{MP2} are energies calculated by the respective methods using the same basis set size. This general approximation [82] has been found to work well [82–84] because the difference between MP2 and CCSD(T) energies converges faster than the energies themselves with respect to basis set size.

In general, CCSD(T) is regarded as the gold standard within computational chemistry and MP2 is understood to be less robust. Indeed MP2 fails to describe metallic systems since in these cases the MP2 correlation energy diverges [85]. In addition, MP2 significantly

overestimates the correlation energy for $\pi - \pi$ stacked systems such as a benzene dimer in a sandwich configuration [85]. Hence, despite the gains in the computational efficiency of quantum chemical methods, MP2 is not always suitable.

Furthermore, for conventional quantum chemical methods, poor scaling enables only smaller systems with less than $\sim$ 50 atoms to be computed, and renders them impracticable for most systems of interest in materials science. Significant progress has been made however in the last 20 years, to circumvent the problems with scaling. Before discussing some of the developments, let us distinguish between the types of scaling that quantum chemical methods suffer from:

- Computational time with respect to system size, *i.e.* number of electrons
- Computational time with respect to N number of basis functions per atom
- Slow reduction of error in energies with respect to basis set size per atom

The steep scaling with the number of electrons is due to terms like the 2-electron 4-index integral in Eq. 2.13. In methods known as local MP2 (LMP2) [86–88] and local coupled cluster (LCC) [89–91], the number of 2-electron integrals to be evaluated is significantly reduced by localising the orbitals and considering only spatially close pairs [92], referred to as domains. How the size of the domains is chosen depends on the localisation scheme and the system. By localising the orbitals into domains, an error is introduced in the correlation energy that, for instance, is not necessarily the same in initial and final states of a reaction. Different localisation schemes exist [91, 93, 94], and continuous effort has been made to reduce domain errors [95, 96]. Staggeringly for MP2, the scaling of computational time falls from N^5 to scaling roughly linearly ($\sim N$) with LMP2. The same linear scaling can be achieved with LCC methods too.

Localising the orbitals still does not change the number of basis functions needed per atom, for which the scaling remains poor. Reformulating the electron repulsion integrals in terms of generalised electron densities instead of individual orbitals allows further savings to be made [92]. This method is known as density-fitting and approximates the electron densities using an auxiliary basis set such that 2-electron 4-index integrals are expressed in terms of 2-electron 3-index integrals instead. Local approximations can be combined with density-fitting in techniques like DF-LMP2 [86] and DF-LCCSD [97].

Regarding the slow convergence of energies with basis set size, this is intricately related to the large number of basis functions needed to describe correlation cusps. Cusps arise from charged particles approaching each other causing a divergence in the Coulomb interaction. However, this is offset by the kinetic energy operator resulting in Ψ being linear in r_{ij} when the interlectronic distance approaches zero. It follows that a better description of the cusps avoids the need for large basis sets. The R12 method does precisely that by augmenting the space of virtual orbitals in MP2 theory with explicitly correlated terms that depend on interelectronic distances, see Ref. [98] for a review of R12 methods.

2.3 Density functional theory

The Thomas-Fermi model introduced the concept of obtaining the energy of a system from the density of electrons as opposed to the wavefunction [74, 75]. It is clear to see that the density of electrons ($\rho(\mathbf{r})$), having only 3 degrees of freedom, is much less complex to process computationally than the wavefunction with $3N_e$ degrees of freedom. However, the Thomas-Fermi model is only correct for describing a homogeneous electron gas (HEG) and fails to describe molecules binding or even the shell structure of atoms.

It was the two Hohenberg-Kohn (HK) theorems [25] which showed that the density of electrons is indeed an exact and useful construct for solving Schrödinger's equation. First, for a system of N_e interacting electrons experiencing an external potential ν_{ext}, there exists a unique corresponding ground state ρ_0. This one-to-one correspondence between ν_{ext} and ρ_0 is the HK existence theorem. Note that ν_{ext} is determined by the positions and charges of nuclei. Hence, if ρ_0 is unique for a given configuration of nuclei, it follows that the ground state wavefunction of the system can be written as a functional of ρ_0,

$$\Psi_0 = \Psi[\rho_0], \tag{2.15}$$

and the ground state electronic energy, E_0^{el}, is therefore,

$$E_0^{el} = E^{el}[\rho_0]. \tag{2.16}$$

Remarkably, the second HK theorem, otherwise known as HK variational theorem, states that

the density that minimises the energy is the ground-state density. That is, for a density ρ' that is different to ρ_0, *i.e.* $\rho' \neq \rho_0$, it follows that:

$$E^{el\prime}[\rho'] \geq E_0^{el}[\rho_0], \tag{2.17}$$

and therefore, ρ_0 can be found variationally by minimization of the total electronic energy.

From the HK theorems it is given that there is a universal (system independent) functional of the ground state electronic density, but the form of this functional is unknown. The Kohn-Sham equations have made DFT practicable by prescribing an exact procedure to express the unknown functional. Recalling the terms defining the electronic Schrödinger equation in Eq. 2.5, E_0^{el} can be expressed as,

$$E_0^{el} = T^{el}[\rho_0] + E^{el-nuc}[\rho_0] + E^{el-el}[\rho_0], \tag{2.18}$$

where T^{el} is the kinetic energy of electrons, E^{el-nuc} is the electrostatic energy between the electrons and the nuclei, and E^{el-el} is the interaction energy between electrons. Both the kinetic energy and electron-electron interaction functionals are not known for interacting electrons. This dilemma is similar to that which lead to the single-particle approximation in HF theory and similarly in the Kohn-Sham equations, single-particle operators are utilised. From the HK theorems, it follows that the Kohn-Sham density of electrons that minimises the total energy is the same as that of the true ground-state electron density.

For a given density of non-interacting electrons $\rho_s(\mathbf{r})$, the Kohn-Sham orbitals are defined as,

$$\rho_s(\mathbf{r}) = \sum_i^{N_e} |\phi_0^i(\mathbf{r})|^2 = \rho_0(\mathbf{r}), \tag{2.19}$$

where $\phi_0^i(\mathbf{r})$ are single-particle states. The kinetic energy of the reference system of non-interacting electrons can be written,

$$T_s^{el}[\rho_s] = -\frac{1}{2}\sum_i^{N_e} \langle\phi_i| \nabla^2 |\phi_i\rangle\,, \tag{2.20}$$

where T_s^{el} is clearly not the same as the kinetic energy of interacting electrons. In combination

with other terms, the energy functional can be written,

$$E^{el}[\rho] = T_s^{el}[\rho] + E^{el-nuc}[\rho] + E^{Hartree}[\rho] + E^{xc}[\rho], \tag{2.21}$$

where $E^{Hartree}[\rho]$ is the classical Coulomb repulsion between electrons. All remaining non-classical interaction that arises within a real system of interacting electrons, including correlation and exchange energy, is placed within $E^{xc}[\rho]$. Up till this point, DFT is exact and every term in Eq. 2.21 can be calculated from the density of electrons exactly, with the important exception of $E^{xc}[\rho]$. In the following section some widely used approximations for the exchange-correlation (xc) functional are introduced.

2.3.1 Exchange-correlation functionals

Unlike post-HF methods in quantum chemistry, there is no unique systematic way to approximate E^{xc} and indeed, a large number of xc functionals have been developed over the years with varying degrees of success [99, 100]. A large part of the work undertaken focuses on the shortfalls of xc functionals and necessitates a brief introduction to those that have been used.

The first suggestion for E^{xc} was made by Kohn and Sham, and based on the homogeneous electron gas (HEG). A HEG has a positive background charge distribution, with a volume and number of electrons that approaches infinity, whilst the density of electrons remains constant for an infinitesimally small volume within. The form of the exchange energy is known exactly for such a system and the correlation energy can be calculated very accurately from explicitly correlated methods such as quantum Monte Carlo or the random phase approximation. In the local density approximation (LDA), we consider an inhomogeneous system of infinitesimally small volumes of constant density. The xc energy corresponding to a given density is taken from the HEG with the same density,

$$E_{LDA}^{xc}[\rho] = \int \rho(\mathbf{r})\epsilon_{xc}(\rho(\mathbf{r}))dr, \tag{2.22}$$

where $\epsilon_{xc}(\rho(\mathbf{r}))$ is the xc energy per particle in a HEG of density $\rho(\mathbf{r})$. The LDA works better for metallic systems where the density of electrons is slowly-varying as in a HEG, but is a rather poor approximation for molecules and insulators in general, where the density changes

rapidly.

To better approximate the non-homogeneity in realistic systems, the gradient of the density is introduced in what is known as the generalised gradient approximation (GGA),

$$E^{xc}_{GGA}[\rho] = \int f(\rho(\mathbf{r}), \nabla\rho(\mathbf{r}))dr, \tag{2.23}$$

where f is some xc functional of $\rho(\mathbf{r})$ and its gradient, $\nabla\rho(\mathbf{r})$. There are many ways to construct such a functional and typically the exchange and correlation components are expressed separately. Given that there is no strictly systematic approach to increase the accuracy, some GGAs have physical constraints implemented and some have variables that are fitted empirically to reference data. Some prominent examples of GGAs include PW91[1], BLYP[2] and PBE[3]. Generally, the performance amongst different GGAs is comparable, showing an improvement over the LDA for some properties such as the atomisation energies of molecules and lattice constants. However, the LDA is known to fortuitously predict better surface energies [101, 102] and also weak interaction energies where GGAs tend to underbind [103].

The LDA and GGAs are the most commonly used approximations in DFT calculations, and warrant a brief discussion of two salient short-falls therein. Specifically, we address the inherent delocalisation error and the lack of long-range correlation energy. Both of these have motivated the development of more sophisticated xc functionals.

First, intrinsic to practically all approximations of the xc functional is the spurious interaction of electrons with themselves. This originates from the mean-field treatment of the Hartree repulsion between electrons, in the same way as in HF theory. Whereas in HF theory this spurious self-interaction is exactly cancelled by the exchange term, in DFT, the cancellation is prevented by the absence of the exact exchange functional for an interacting system. As a result of the increased repulsion, the predicted electronic configuration is more delocalised, hence it is referred to here as the delocalisation error. Noting the comparison that has been made with HF theory, it is not surprising that one of the common methods to alleviate delocalisation is by the inclusion of some exact exchange evaluated using the Kohn-Sham orbitals. Such functionals are called hybrids and include notable examples such

[1]PW91 is based on Becke's B88 exchange functional and Perdew and Wang's correlation functional.
[2]BLYP is composed of B88 exchange also and Lee-Yang-Par correlation functional.
[3]PBE is the Perdew-Burke-Ernzerhof functional that has been derived without any empiricism.

as PBE0 with 25% exact exchange, B3LYP with 20% exact exchange, and the range separated hybrid known as Heyd-Scuseria-Ernzerhof (HSE) functional. The HSE functional and similar range-separated functionals have a varying amount of exact exchange depending on the electron-electron distance, in order to improve the computational efficiency. The amount of exact exchange to include is somewhat of an arbitrary choice and has been shown to be system dependent. Furthermore, hybrid functionals are considerably more expensive than GGAs (or the LDA) because of the evaluation of exchange integrals. In practice hybrid functionals are used for particular instances such as when accurate band gaps are desired or strongly correlated systems are modelled.

Second, all of the xc functionals discussed thus far do not account for non-local correlation energy between electrons. The correlation functionals are local, and only produce non-zero correlation energy for overlapping electron densities. However in real systems, dynamic correlation interactions can extend to nanometres [104], and certainly far beyond the overlap of electron densities. Note that long-range correlation is a form of Coulomb interaction that arises from the instantaneous dipole produced by the fluctuating positions of electrons that induce a dipole elsewhere. These long-range correlation interactions can be referred to as van der Waals (vdW) or dispersion interactions. The dispersion interaction is difficult to approximate within DFT, partly because it is a many-body phenomenum with non-additive behaviour that we do not know how to express in terms of the density of electrons. Moreover, it may require very large simulation cells to capture entirely, due to its slow decay (typically $1/r^6$ for molecules and atoms). A considerable amount of development in DFT xc functionals has allowed for a much improved description of systems where dispersion interaction is prevalent and we discuss two general approaches here. For a more comprehensive review see references [43–47].

In a particularly computationally efficient approach, the energy, typically from a hybrid functional or GGA, is supplemented with a dispersion correction. Such methods can be referred to as dispersion corrected xc functionals and the correction is usually of the form,

$$E_{disp} = -\frac{1}{2}\sum_{A,B} f_{d,6}(r_{AB})\frac{C_{6,AB}}{r_{AB}^6}, \tag{2.24}$$

where E_{disp} is the dispersion energy correction, $f_{d,6}$ is a damping function that reduces the

dispersion correction at short bonding distances, and $C_{6,AB}$ is the dispersion coefficient for an atom pair A, B. In the D2 method of Grimme, the C_6 dispersion coefficients are tabulated according to the free atomic species and independent of the chemical environment in the system. The coordination environment of atoms in the simulation is taken into account in the more sophisticated D3 correction of Grimme. Moreover a second term is introduced in Eq. 2.24 that accounts for three-body interactions in the D3 method. In a more recent method known as the Tkatchenko-Scheffler (TS) scheme, the C_6 coefficients are self consistently determined. This is done by expressing the atomic C_6 coefficient in terms of the effective atomic volume using a Hirshfeld partitioning of the total electron density of a system. In this way, the C_6 coefficients are explicitly dependent on their chemical environment. A further correction to the TS scheme is self-consistent screening (scs), which approximates the response of a system to a dynamic electric field arising from polarisable atoms in the sorroundings. Even more sophisticated is the many-body dispersion (MBD) correction of Tkatchenko. The MBD method is based on the RPA correlation energy of quantum harmonic oscillators representing atomic contributions. Unlike other dispersion corrections, the MBD method is able to approximate all higher order dispersion interactions as well as long-range screening.

Although dispersion corrections have been shown to alleviate the underestimation of interaction energies by GGAs and hybrid functionals, they are not consistently accurate. The underlying xc functional and the damping function in Eq. 2.24 can both have a considerable impact on the predictive power.

Another method for approximating dispersion interactions are the vdW density functionals (vdW-DF). Unlike dispersion corrections, the vdW-DFs seamlessly integrate two-body dispersion into the xc energy using the electron density of a system. The xc energy is defined as,

$$E_{xc} = E_x^{GGA} + E_c^l + E_c^{nl}, \tag{2.25}$$

where E_c^{nl} is the non-local correlation energy and E_c^l is the local correlation energy. The non-local correlation energy is evaluated using the electron density,

$$E_c^{nl} = \frac{1}{2} \int \rho(\mathbf{r}) \Phi(\mathbf{r}, \mathbf{r}') \rho(\mathbf{r}') dr dr', \tag{2.26}$$

where $\Phi(r, r')$ is a correlation kernel that is based on the plasmon-pole model. The original

vdW-DF of Dion *et al.* uses the revPBE exchange functional and the LDA for local correlation, but it was found to underestimate the interaction energy between molecules and correspondingly, overestimate minimum binding distances. During the last decade, several modifications have been proposed for the exchange functional in Eq. 2.25 whilst maintaining the same correlation functionals. In this thesis, the optB88-vdW, optPBE-vdW, and optB86b-vdW functionals have been used. Furthermore, the vdW-DF2 and rev-vdW-DF2 have also been used. These are developed with a different non-local correlation functional as well as a different exchange functional.

Several reviews and perspectives are available comparing different dispersion approximations in DFT, but generally the performance of xc functionals varies considerably. Indeed it has been accepted, alhough sometimes overlooked, that the performance of xc functionals is somewhat system dependent and cannot be expected to hold across different system sizes or electronic properties. Understanding the scope of xc approximations is therefore very important in making useful predictions.

Comparing post-HF methods like CCSD(T) and FCIQMC with DFT, there is an unfortunate negative correlation between accuracy and affordability of these methods. An outcome of this is that there is a vacuum of reference information for large periodic systems. In the following sections, we introduce two, much less commonly used methods, that can be applied to periodic systems with relatively large unit cells and maintain high accuracy.

2.3.2 Random phase approximation

In some chapters, results from random phase approximation calculations have been provided by collaborators. These RPA results form an important part of some of the discussion later and so it is useful to briefly introduce the method here.

The RPA is a method that can be derived either from perturbation theory or from the adiabatic-connection fluctuation-dissipation theorem [105–107]. To understand the fluctuation-dissipation theorem in this context, consider this: *"...the frequencies at which charges spontaneously fluctuate are the same as those at which they naturally move, or resonate, to adsorb external electromagnetic waves."* – from Van Der Waals Forces by V. Adrian Parsegian [108]. This connection between the absorption behaviour of a system and the instantaneous fluctuation of electrons is utilised in the RPA (see below).

By the adiabatic-connection fluctuation-dissipation theorem, a system of non-interacting electrons is directly connected to a system of fully correlated electrons, and it is in principle exact. A coupling constant, λ, dictates the electron-electron interaction strength from non-interacting to fully interacting,

$$E^{el} = \int_0^1 d\lambda \left\langle \Psi_\lambda \right| V^{el} \left| \Psi_\lambda \right\rangle, \tag{2.27}$$

where V_{el} is the electron-electron interaction potential and Ψ_λ is the ground-state wavefunction of a system with a scaled electron-electron interaction. To remain exact, the electron density is kept constant at the fully interacting density. This is achieved by varying the local potential such that for $\lambda = 0$ the potential is simply the Kohn-Sham potential and when $\lambda = 1$, it is the external potential.

The total electron-electron interactions can be expressed in terms of the classical electrostatic repulsion (Hartree term), the exchange interaction, and the correlation of electrons. The Hartree term is already calculated in DFT from the electron density and the Fock exchange interaction can be calculated for the Kohn-Sham orbitals. Crucially, it is the correlation energy component that is expressed in the RPA using the adiabatic connection. For this, the fluctuation-dissipation theorem states that the frequencies at which charges (*i.e.* electrons) resonate to absorb light are the same as those at which they spontaneously fluctuate. Thus the correlation energy can be expressed in terms of imaginary frequencies,

$$E^{el} = E^{Hartree}[\rho] + E^{x}[\phi_i] - \int_0^1 d\lambda \int_0^\infty \frac{d\omega}{2\pi} Tr\big[V^{el}(\chi^\lambda(i\omega) - \chi^0(i\omega))\big]. \tag{2.28}$$

The last term on the right hand side is the RPA correlation energy and includes the response functions of the Kohn-Sham system χ^0, and that of a system with a given coupling constant, χ^λ.

Calculating χ^λ is non-trivial. Firstly, the form of the exchange-correlation kernel that is needed to know the Kohn-Sham response is unknown. Secondly, it would be computationally expensive if the kernel were known. Thus in the direct RPA method it is simply assumed to be zero. Direct RPA is still not self-consistent in practice and is therefore massively dependent on the Kohn-Sham orbitals that we put in. The performance of direct RPA depends on the

property of interest. For atomization energies, direct RPA is no better than GGAs in DFT and is therefore not worth the increased computational effort. On the other hand, the RPA is able to predict the experimentally observed adsorption site of CO molecules on a Pt(111) surface, where almost all DFT xc functionals have failed [59, 109]. In addition, the RPA accounts for correlation energy explicitly and can therefore describe vdW interactions with superior accuracy and consistency compared to DFT xc functionals. Let us note that binding energies are generally underestimated by direct RPA [60, 110, 111]. It has been shown that the inclusion of single excitations correction goes some way to alleviate the underbinding [110]. Similarly, the inclusion of the second-order screened exchange (SOSEX) has been shown to improve the description of electron correlation [105]. For an overview of the RPA see reference [106].

2.4 Quantum Monte Carlo

Some common computational approaches to solving the Schrödinger equation for a many-body wavefunction have been presented in Sections 2.2 and 2.3. All of the methods discussed therein use single-particle operators on the many-body wavefunction and as a result, correlation manifests separately. Quantum Monte Carlo (QMC) encompasses various wavefunction based approaches that do not resort to single-particle operators and provide a many-body solution to the Schrödinger equation, using the Monte Carlo technique. The key machinery of QMC methods is highlighted here, followed by a description of two QMC methods, namely, variational Monte Carlo (VMC) and diffusion Monte Carlo (DMC).

2.4.1 The Monte Carlo technique

"*The question was what are the chances that a Canfield solitaire laid out with 52 cards will come out successfully? After spending a lot of time trying to estimate them by pure combinatorial calculations, I wondered whether a more practical method than "abstract thinking" might not be to lay it out say one hundred times and simply observe and count the number of successful plays.*" – Stanisław Ulam, 1946

When multi-dimensional integrals are solved numerically, traditional methods based on quadrature have errors scaling as $n^{-4/d}$ where n is the number of points sampled and d is

the dimension. As the dimensions of the integral increases (in our context that is the number of electrons), the error scaling becomes tedious computationally. In contrast, the error from Monte Carlo integration is independent of the dimensions of the integral and is always $n^{-1/2}$. As Ulam discovered, this means that finding the value of an integral with many dimensions can be done by stochastically sampling n random points within the volume of the integral and averaging,

$$\tilde{I} = \frac{1}{n}\sum_{i}^{n} f(x_i), \tag{2.29}$$

here $\tilde{I}$ is the estimate of the integral with n number of sampled points x. The important implication is that Schrödinger's equation can be solved using the Monte Carlo technique with the same efficiency for any number of electrons, given a multidimensional integral (see below).

Monte Carlo sampling can be further improved if one has *a priori* knowledge of the function's approximate shape. The shape can be expressed as a probability distribution $p(x)$, and by randomly sampling this distribution the estimate of the integral is,

$$\tilde{I} = \frac{1}{n}\sum_{i}^{n} \frac{f(x_i)}{p(x_i)}. \tag{2.30}$$

The closer $p(x)$ matches $f(x)$, the more efficiently $f(x)$ is sampled and hence, the lower the statistical error becomes. This is known as importance sampling. As it will be seen, importance sampling is especially useful in QMC methods, where a good estimate of the electron probability distribution can be taken from DFT or HF calculations.

Sampling of the probability distribution is often done using the Metropolis algorithm: Random walkers are used to explore a given probability distribution where each walker visits x_i points. First, a transition probability $T(x';x)$ is defined that must be ergodic. Second, given an initial point x, a new trial point x' is generated according to $T(x';x)$. To satisfy detailed balance, this trial point x' is accepted with the probability,

$$p = \min\left(1, \frac{p(x')T(x';x)}{p(x)T(x;x')}\right), \tag{2.31}$$

where after some equilibration time, the points generated are distributed as $p(x)$. In this way, the walkers mostly explore points where the probability distribution is high - complementing

the importance sampling method.[4]

The Monte Carlo integration method along with the Metropolis accept/reject scheme and importance sampling form the core numerical mechanism behind QMC methods. Different QMC methods exist for evaluating various many-body problems. An important focus of this work has been to establish accurate reference energies for weak interactions. For this, variational and diffusion Monte Carlo are especially useful and deserve further discussion in the following sections.

2.4.2 Variational Monte Carlo

The energy associated with a trial wavefunction $\Psi_T(\mathbf{r})$ for the exact ground-state wavefunction can be written as,

$$E_{VMC} = \frac{\int \Psi_T^*(\mathbf{r})\hat{H}\Psi_T(\mathbf{r})d\mathbf{r}}{\int \Psi_T^*(\mathbf{r})\Psi_T(\mathbf{r})d\mathbf{r}}, \tag{2.32}$$

where E_{VMC} is an upper bound for the exact ground state energy by the variational principle. Recalling Eq. 2.30, an expression of the expectation value for the Born-Oppenheimer, all-electron Hamiltonian in terms of the probability density (*i.e.* $|\Psi(\mathbf{r})|^2/\int|\Psi(\mathbf{r})|^2d\mathbf{r} = \Pi(\mathbf{r})$) is ideal. Thus we can write,

$$E_{VMC} = \frac{\int |\Psi_T(\mathbf{r})|^2 \frac{\hat{H}\Psi_T(\mathbf{r})}{\Psi_T(\mathbf{r})}d\mathbf{r}}{\int |\Psi_T(\mathbf{r})|^2 d\mathbf{r}}, \tag{2.33}$$

where $\frac{\hat{H}\Psi_T(\mathbf{r})}{\Psi_T(\mathbf{r})} = E_L(\mathbf{r})$, that is the local energy. Note that $E_L(\mathbf{r})$ diverges at the nodes of $\Psi_T(\mathbf{r})$ and this has important consequences that we shall visit later. The Metropolis algorithm is used in Eq. 2.33 to generate electron configurations defined by a set of coordinates $\mathbf{r}$ with probability distribution $\Pi(\mathbf{r})$, for which $E_L(\mathbf{r})$ is averaged. The wavefunction can be optimised to lower the variational energy. In addition, as Ψ_T is optimised towards Ψ_0, the variance in E_L approaches zero. This is known as the zero variance principle and it can be used to minimise the variance instead of the energy. An advantage of minimising the variance is that the lower bound (zero) is given. Secondly, one can use the variance of $E_L(\mathbf{r})$ to compare the quality of different trial wavefunctions for a given system.

Although VMC is a straightforward method, its accuracy is strongly dependent on the functional form of the trial wavefunction and hence the quality of the basis set. Typically

[4] In the CASINO code that is used for QMC calculations in this work, a two-level sampling algorithm is used for superior efficiency.

VMC recovers 70-85% of the correlation energy but better accuracy can be achieved with the use of more sophisticated starting wavefunctions [112]. Generally, VMC lacks a systematic way to approach the ground state wavefunction beyond importance sampling. Projector based Monte Carlo methods have been developed that project out the ground state wavefunction. Diffusion Monte Carlo (DMC) is the main benchmark projector method used in this work and is introduced in Section 2.4.3. Before doing so, note that VMC is routinely used to optimise a wavefunction for use in DMC. As such, let us comment briefly on the form the wavefunction used in QMC calculations.

Since the accuracy of a VMC calculation is strongly dependent on the input wavefunction, it is essential to provide a good quality starting point. Generally one produces a trial wavefunction from DFT or HF calculations, and augments it with a Jastrow factor J [113] for a Slater-Jastrow type wavefunction,

$$\Psi(\mathbf{r}) = exp[J] \sum_n c_n D_n^{\uparrow} D_n^{\downarrow}, \tag{2.34}$$

where c_n are the determinant coefficients and $D_n^{\uparrow}$ and $D_n^{\downarrow}$ are the Slater determinants of up and down single particle spin orbitals, respectively. The role of the Jastrow factor is to improve the description of the correlation energy in the trial wavefunction by introducing electron-electron interactions explicitly. Given that there is no correlation energy in HF and that xc functionals are approximations often without long-range correlation, the Jastrow factor makes a significant improvement to the accuracy of VMC. In the QMC calculations performed in this thesis, the Jastrow factor takes the form proposed by Drummond *et al.* [114],

$$J(\mathbf{r_i}, \mathbf{R_I}) = \sum_{i=1}^{N_e-1} \sum_{j=i+1}^{N_e} u(r_{ij}) + \sum_{I=1}^{N_n} \sum_{i=1}^{N_e} \chi_I(r_{iI}) + \sum_{I=1}^{N_n} \sum_{i=1}^{N_e-1} \sum_{j=i+1}^{N_e} f_I(r_{iI}, r_{jI}, r_{ij}). \tag{2.35}$$

In this equation, $u(r_{ij})$ is the isotropic electron-electron term; $\chi_I(r_{iI})$ is the isotropic electron-nucleus term centred on nuclei; and $f_I(r_{iI}, r_{jI}, r_{ij})$ is the isotropic electron-electron-nucleus term centred on nuclei also. Each of these terms are expanded in terms of polynomials with variable parameters that are optimized in a VMC calculation. An important feature of the terms in the Jastrow factor above, is that they satisfy Kato cusp conditions [115, 116]. In other words, when two electrons or an electron and a nucleus are coincident, the correct

behaviour is produced for the many-body wavefunction[5].

The VMC energy can be lowered variationally by varying the Jastrow parameters in what is referred to as energy minimization. As mentioned earlier, the variance is also a measure of accuracy and can also be minimized with respect to the Jasrtow parameters. The number of variational parameters can be increased but it also makes subsequent DMC calculations more expensive. As such, one typically only increases the number of parameters if it justified by a marked improvement in the VMC energy or variance.

2.4.3 Diffusion Monte Carlo

In principle DMC provides an exact stochastic solution to Schrödinger's time-dependent equation. DMC is only very weakly dependent on the initial trial wavefunction compared to VMC and provides a more accurate estimation of the energy. As such, VMC is generally used to optimise the wavefunction for use in DMC.

Recalling the imaginary time-dependent Schrödinger equation (Eq. 2.2), the Hamiltonian can be expressed in terms of the kinetic and potential energy of the system,

$$\Big[-\frac{1}{2}\nabla^2_{\mathbf{r}} + V(\mathbf{r})\Big]\Psi(\mathbf{r},\tau) = -\frac{\partial}{\partial\tau}\Psi(\mathbf{r},\tau), \tag{2.36}$$

where the first term is the kinetic energy operator for the electrons, the second term is the potential energy operator encompassing electron-electron and electron-nucleus interactions, and $\tau = it$. An ensemble of random walkers is used to represent the electron configurations and therefore the wavefunction. Note that Eq. 2.36 resembles a diffusion equation with a diffusion constant $D = 1/2$ with an additional, exponential growth/decay (or *branching*) term, $V(\mathbf{r})$ for the random walkers. Reformulating this potential term as a weight (w) corresponding to each random walker,

$$-\frac{dw}{d\tau} = \big(V(\mathbf{r}(\tau)) - E_T\big)w, \tag{2.37}$$

it can be incorporated into a complete diffusion equation that can be propagated in imaginary time. The term E_T that has been introduced in Eq. 2.37 is used to adjust the weight of walkers during a simulation. E_T is updated with the best estimate of the ground state energy such

[5]The Kato cusp conditions arise from the requirement that the divergences in the local kinetic energy and local potential energy cancel each other at the point of coincidence.

that population of walkers remains stable. In doing so, the wavefunction is evolved from a starting trial wavefunction towards the exact ground state wavefunction,

$$\Psi(\mathbf{r}, \tau \to \infty) = c_0 e^{(-E_0 - E_T)\tau} \Psi_0(\mathbf{r}). \tag{2.38}$$

Here, c_0 must be a non-zero coefficient, E_0 is the ground state energy, and the energy shift E_T acts only as a normalisation constant.

In DMC, the propagation of the random walkers in Eq. 2.36 with time, is done via Green's function,

$$\Psi(\mathbf{r}, \tau_0 + \tau) = \int G(\mathbf{r} \leftarrow \mathbf{r}' : \tau) \Psi(\mathbf{r}', \tau_0) d\mathbf{r}', \tag{2.39}$$

where τ_0 is the initial imaginary time and the Green's function equates to,

$$G(\mathbf{r} \leftarrow \mathbf{r}' : \tau) = \langle \mathbf{r} | \, e^{-\tau(\hat{H} - E_T)} \, | \mathbf{r}' \rangle \, . \tag{2.40}$$

However, $G(\mathbf{r} \leftarrow \mathbf{r}' : \tau)$ is not known exactly for realistic systems. Instead, by invoking the Suzuki-Trotter formula, the Green's function can be approximated in terms of the known diffusion and branching processes,

$$G(\mathbf{r} \leftarrow \mathbf{r}' : \Delta\tau) \approx G_b(\mathbf{r} \leftarrow \mathbf{r}' : \Delta\tau) G_d(\mathbf{r} \leftarrow \mathbf{r}' : \Delta\tau), \tag{2.41}$$

where $G_d(\mathbf{r} \leftarrow \mathbf{r}' : \Delta\tau)$ is the diffusion term, $G_b(\mathbf{r} \leftarrow \mathbf{r}' : \Delta\tau)$ is the branching term, and $\Delta\tau$ is the time-step. In the diffusion term, the kinetic energy allows for walkers to diffuse randomly simulating new electron configurations. Meanwhile, in the branching term, the potential energy governs the growth and decay of the walkers. When the potential energy of an electron configuration is low, the weight of the walkers is large, leading to growth. Decay occurs when the energy is high, and therefore any excitated states decay until only the ground state wavefunction remains. Note that the Suzuki-Trotter formula is only accurate for short time-steps and this approximation therefore introduces a time-step bias.

Two important problems arise for a physical system. First, the potential energy contains the Coulomb operator which diverges for electrons that are very close to each other or very close to nuclei. These singularities can lead to significant population explosions and thus

numerical instabilities. Second, Ψ is not a probability distribution with the same sign everywhere as assumed. As a fermionic system, the wavefunction is anti-symmetric but no such symmetry has been imposed in DMC. Since bosonic states are almost always lower in energy than fermionic states; the non-orthogonal bosonic wavefunction is projected out despite a fermionic trial wavefunction. The most common method of alleviating both of these two problems is by introducing importance sampling again. Replacing $V(\mathbf{r})$ with E_L, any regions where the electrons are close to singularities are avoided in the limit of zero time-step. That includes the nodes of the trial wavefunction, which are fixed in place. Once the nodes are fixed, all regions between nodes can be treated as probability distributions. This is known as the fixed node approximation and has been employed in all the DMC calculations in this work. Of course, this approximation means that DMC is no longer exact unless the nodes of the trial wavefunction are exactly in the ground state postion (which is unlikely). As an uncontrolled error, this can be catastrophic in energy differences for which the nodal surface is considerably different amongst the intitial and final states [117]. However it has been shown that for weak interactions we can expect a favourable error cancellation [118].

2.5 Calculations in practice

The first principles methods (quantum chemistry, DFT, QMC) that have been introduced require a mathematical representation of the variables such as the single-particle states, to be computationally solvable. In addition, if simulating a solid state material, periodic boundary conditions are needed to model the properties of an extended material without using simulation cells with an intractable number of atoms. In this section, basis sets that have been used for first principles methods in this work are addressed. A more general guide to performing atomistic computer simulations can also be found in Ref. 119.

The wavefunction in quantum chemical methods and DFT is expressed as a sum of single-particle orbitals, and we seek a real-space representation of these.

$$\psi_i(\mathbf{r}) = \sum_{1}^{P} c_{i,p}\varphi_p(\mathbf{r}), \tag{2.42}$$

In Eq. 2.42 a single-particle orbital is expressed by a basis set of functions ($\varphi_p(\mathbf{r})$) with

expansion coefficients ($c_{i,p}$). The expression is exact for $P \to \infty$ but in practice the size of the basis set is chosen according to the convergence of a property of the system. The two most common types of basis set functions are atom-centred functions and plane-waves.

2.5.1 Localised basis sets

Atom-centred functions are typically chosen to resemble the hydrogenic orbitals (*s, p, d ...*). A sum of Gaussian functions are commonly used because various single-particle operators can be solved analytically for Gaussian functions. On the other hand, several Gaussian functions are needed per single-particle orbital to better approximate the cusp of the electron density at the nuclei as well as bonding regions in molecules. Polarisation functions with higher angular momenta than the occupied states are particularly useful for a more flexible representation of molecular orbitals. For anions and other diffuse electron densities, additional diffuse functions can be used to provide a more accurate description. Standard localised basis sets have been developed by Pople and Dunning, and the latter has been used for quantum chemical calculations in some chapters. Two important errors need to be addressed when localised basis sets are used. The first is the impact from using a finite set of functions to describe the wavefunction. This is normally accounted for by making a complete basis set (CBS) extrapolation using two or three different sizes of basis sets. Several schemes exist [120–124] to make CBS extrapolations and Dunning's correlation consistent basis sets have been specifically designed to allow for extrapolation [125–127]. The second error stems from the overestimation of interactions in the region where basis functions of separate fragments overlap and is referred to as basis set superposition error (BSSE). BSSE can be alleviated by using a more complete basis set that describes the wavefunction more accurately. Another widely used scheme for correcting BSSE is Boys and Bernardi's counterpoise correction [128].

2.5.2 Plane-waves and Bloch's theorem

Another mathematical representation of the wavefunction is plane-waves. These are periodic functions and are therefore suitable for representing orbitals - especially in solid state systems where localised basis sets may not be as efficient. Plane-waves are Fourier representations of orbitals expressed as $e^{iG \cdot r}$, where G is a vector of the reciprocal lattice. As such, plane-waves are computationally favourable because integrals can be evaluated efficiently using fast Fourier

transforms. Plane-waves also lend themselves to the use of periodic boundary conditions which is realised using Bloch's theorem. According to this theorem, the eigenfunctions of a Hamiltonian can be expressed as the product of a plane-wave function and a function with the same periodicity as the potential felt by the single-particle states:

$$\psi_{n,\mathbf{k}}(\mathbf{r}) = u_{n,\mathbf{k}}(\mathbf{r})e^{i(\mathbf{k}\cdot\mathbf{r})}. \tag{2.43}$$

In Bloch's theorem, $\mathbf{k}$ is a reciprocal vector in the first Brillouin zone and n enumerates the number of eigenfunctions for each $\mathbf{k}$-point. The function $u_{n,\mathbf{k}}(\mathbf{r})$ has the same periodicity as the unit cell, such that $u_{n,\mathbf{k}}(\mathbf{r}) = u_{n,\mathbf{k}}(\mathbf{r}+\mathbf{R})$, where $\mathbf{R}$ is translation vector in the Bravais lattice. By Bloch's theorem, it is possible to use a primitive unit cell to model a periodic extended system, and integrating over the whole Brillouin zone to get the exact energy. In principle, this requires an infinite number of $\mathbf{k}$-points but in practice, it is approximated through a finite set of $\mathbf{k}$-points that are sampled to converge some properties of interest. Generally, molecules and solid state insulators do not require a large number of $\mathbf{k}$-points and are often converged at the Γ-point. In contrast, metals and systems with small band gaps require more $\mathbf{k}$-points for convergence.

A drawback of plane-wave basis sets is that many plane-waves are required to describe the highly oscillatory nature of valence electron states in the core region near the nuclei. These oscillations arise because of the strong ionic potential exerted in the core region, and to maintain orthogonality with the core electron states. One method of increasing the computational efficiency then, is to treat the core electrons differently to the valence electrons. Pseudopotentials are commonly used to mimic the potential felt by valence electrons from the core region (*i.e.* core electrons and nucleus) of an atom. Since most chemical interactions involve only the valence electrons, this is often a good approximation. The separation between core and valence region is defined by a radial cut-off from the nucleus. In norm conserving pseudopotentials, the rapid oscillations near the nucleus are smoothed out whilst maintaining the real (all-electron) norm of the orbitals. In ultrasoft pseudopotentials, the norm is not conserved and an extra charge is added in the core region as a correction. As such, the pseudo-orbitals in the core region are even smoother and therefore require a lower plane-wave energy cut-off than norm conserving pseudopotentials.

Alternatively, the projector-augmented wave (PAW) method can be used, and indeed has been used for many DFT calculations in this thesis. PAW pseudopotentials are calculated by computing the pseudo-wavefunction first and using it to calculate the real wavefunction with an all-electron treatment. The difference between the two wavefunctions is used to correct the pseudo representation. The PAW pseudopotentials have smaller radial cut-offs than ultrasoft pseudopotentials, and therefore usually require higher plane-wave cut-off energies for convergence. On the other hand, PAW pseudopotentials allow for all-electron calculations (with frozen core electrons). Let us finally note that with any plane-wave basis set, the quality can be systematically improved by increasing the energy cut-off and hence, the number of plane-waves.

The majority of DFT codes scale cubicly with the number of atoms but it should be noted that better scaling can be achieved with real-space methods. Indeed, linear scaling DFT codes that have been developed allow for thousands and even millions of atoms to be simulated [129, 130]. It should be noted that there are important challenges in achieving the same accuracy with linear scaling DFT as with conventional DFT codes. Two particular challenges are the convergence of localised basis sets and second, metals and systems with near-zero band gaps are still beyond the scope of such codes. See reference [131] for a review of linear scaling DFT.

The real-space representation of orbitals can be used in linear scaling DFT codes, but it also aides the efficiency of QMC calculations. More specifically, B-spline representation (or blips) [132] have been used in the QMC calculations performed as part of this thesis. This is done by converting the plane-wave representation of a wavefunction from DFT into a localised form using cubic spline functions.

Chapter 3

Water and 1,2-azaborine: role of exact exchange

3.1 Abstract

DFT studies of weakly interacting complexes have recently focused on the importance of van der Waals dispersion forces whereas, the role of exchange has received far less attention. Here, by exploiting the subtle binding between water and a boron and nitrogen doped benzene derivative (1,2-azaborine) we show how exact exchange can alter the binding conformation within a complex. Benchmark values have been calculated for three orientations of the water monomer on 1,2-azaborine from explicitly correlated quantum chemical methods, and also diffusion quantum Monte Carlo. For a host of popular DFT exchange-correlation functionals we show that the lack of exact exchange leads to the wrong lowest energy orientation of water on 1,2-azaborine. As such, a high proportion of exact exchange and the associated improvement in the electronic structure could be needed for the accurate prediction of physisorption sites on doped surfaces and in complex organic molecules. Meanwhile to predict correct absolute interaction energies an accurate description of exchange needs to be augmented by dispersion inclusive functionals, and certain non-local van der Waals functionals (optB88- and optB86b-vdW) perform very well for absolute interaction energies. Through a comparison with water on benzene and borazine ($B_3N_3H_6$) we show that these results could have implications for the interaction of water with doped graphene surfaces, and suggest a possible way of tuning the interaction energy.

3.2 Introduction

An accurate description of the structures and energies of weakly interacting systems is important in materials science and biology, but it is often difficult to obtain reference data either theoretically or experimentally. Specifically, it is difficult to capture small energy differences on the order of a few meV. Although, such small energy differences may seem insignificant, they can have a drastic impact on the final structure. Complex organic molecules, for instance, may form several metastable crystal structures with lattice energies within tens of meV of each other [56, 57, 133]. Knowing the lowest energy structures are of critical importance in pharmacy, since different polymorphs will have different physical properties, see for example, Ref. 134 and references therein.

Thanks to remarkable advances in combining boron, nitrogen and carbon atoms in a cyclic aromatic arrangement it is now possible to create 2-dimensional sheets with carefully structured regions of carbon and boron nitride [135–137]. Despite the growing number of studies for water on h-BN [138–140] and graphene [63, 141–146] there are no direct measurements of adsorption energies for the water monomer, and the theoretical adsorption energies for these systems vary significantly across different high accuracy methods [63, 64, 145, 147].

One can use smaller model systems for graphene [145, 147–150] and h-BN, such as benzene and the inorganic counterpart borazine ($B_3N_3H_6$), to help understand the interaction with water. With these small molecules, it is possible to use high accuracy methods to calculate benchmark interaction energies and binding conformations, [151–155] that would otherwise be infeasible for the extended surfaces. Given the shortage of reference data across these systems, there is a strong incentive to deliver accurate benchmark calculations, and for our purposes, we require a model system that is a hybrid of benzene and borazine. With that in mind, the weak binding between water and an aromatic molecule known as 1,2-dihydro-1,2-azaborine (or 1,2-azaborine for short) as a reference system is studied. The 1,2-azaborine molecule shares many similarities to benzene, with the clear distinction being the asymmetry of the molecule due to boron and nitrogen substitution (see Fig. 3.1). The mixture of boron, nitrogen and carbon atoms in this molecule makes it a suitable model for benchmarking in relation to extended surfaces that are hybrids of graphene and h-BN [156]. Moreover, the asymmetry makes 1,2-azaborine an ideal system for testing the performance of computational

methods because each atom in the ring has a distinct chemical environment that serves as a tag, in contrast to benzene in which carbon atoms are obviously indistinguishable.

Previous work on the water-benzene interaction and other weak interaction systems has demonstrated that methods without long-range correlation fail to account for dispersion interactions that are important for the interaction energy [63, 64, 154, 157–161]. However, most studies of such systems have focused on the description of long-range correlation, and fewer have shown that the underlying exchange approximation can also have an impact on the binding interaction [162–164]. Here, the water/1,2-azaborine system has been examined with coupled cluster with single, double and perturbative triple excitations (CCSD(T)), and a range of DFT exchange-correlation (xc) functionals. Many exchange-correlation functionals are found to predict the wrong conformation of water on 1,2-azaborine, and this problem is solved by including a high proportion of exact exchange, highlighting the need for improvements in existing models of exchange [43, 100, 165, 166]. As part of this chapter DMC has also been tested. It is shown that DMC does well with respect to the CCSD(T) benchmarks, again achieving subchemical accuracy.

This chapter will start with a brief summary of the employed methods, followed by results from a set of calculations that allow us to directly compare the performance of different xc functionals with other explicitly correlated methods. After analysis and discussion of the various DFT results on the intermediate 1,2-azaborine system, the effect of the boron nitride doping is investigated, by also studying the interaction of water with the pure systems of benzene and borazine. We close with a discussion and some general conclusions.

3.3 Methods

3.3.1 Computational Methods

A series of quantum chemical calculations using Dunning's augmented correlation consistent basis sets (aug-cc-pVXZ) [125–127] have been undertaken. Second order Møller-Plesset perturbation theory (MP2) with up to aug-cc-pV5Z basis sets along with CCSD(T) calculations at the aug-cc-pVTZ level have been conducted. Due to the unfavorable scaling of CCSD(T), it is more feasible to conduct MP2 calculations with larger basis sets, deducing the complete basis set (CBS) limit, and subsequently calculating the ΔCCSD(T) value of absolute inter-

action energy at the CBS limit. For a description of this procedure along with analysis of errors, the reader is referred to the recent work of Sherrill and coworkers [167]. Regarding the CBS limit, various extrapolation schemes have been discussed [120–124] and we have chosen to use the one proposed by Halkier *et al.* [121–123] Gaussian03 [168] was used for the HF and post-HF calculations.

The initial single particle wavefunctions for use in DMC were obtained from DFT plane-wave (PW) calculations using the PWSCF package [169] and Trail and Needs pseudopotentials (PPs) were used for all atoms in the system [170, 171], warranting a standard 300 Ry energy cut-off. Previous work by Ma *et al.* [154] indicates that weak binding energies are not overly sensitive to the trial wavefunctions (TWs), having tested a few xc functionals (including hybrids) and also HF. TWs have been generated using the LDA [172] and also the PBE [173] xc functional. The resulting wavefunctions were expanded in terms of B-splines [174] for efficiency. DMC calculations have been performed using the CASINO code [175], and Slater-Jastrow type TWs have been used, in which the Jastrow factor contains electron-nucleus, electron-electron, and electron-electron-nucleus terms. We used a combination of DMC calculations using 16,000 walkers across 160 cores and 64,000 walkers across 640 cores. Final DMC results have been derived by the weighted averaging of the results and errors. Time steps of 0.0025, 0.005 and 0.01 a.u. have been tested and the locality approximation was utilized [176]. We obtained statistical error bars for our interaction energies of ± 3 meV, which corresponds to 1σ.

VASP 5.3.2 [177–180] was used for all the DFT calculations. VASP employs plane-wave basis sets and uses projector augmented wave (PAW) potentials [181, 182] to model the core region of atoms. After a series of convergence tests for the plane-wave cut-off energy and unit cell, we chose to use a 500 eV cut-off energy and a 15 Å length cubic unit cell, along with Γ-point sampling of reciprocal space.

There is, of course, an almost endless list of xc functionals that could be considered, and here we benchmark a selection of fairly widely used functionals. The functionals tested include PBE [173] which is a GGA functional that does not contain long-range correlation. We have also considered the hybrid xc functionals which contain a proportion of exact exchange: PBE0 [183, 184] and B3LYP [185–188]. There have been many developments to include van der Waals (vdW) dispersion in xc functionals, as discussed in the perspective of Klimeš

and Michaelides [43] and reviewed by Grimme [44], and here we have tested several of these vdW-inclusive DFT approaches. Specifically, PBE-D2 [189], a semi-empirical functional that contains Grimme's D2 correction, and also two correction schemes from Tkatchenko and Scheffler, namely vdW-TS [38] and vdW-TS+SCS [38, 39], referred to here as TS and TSscs, respectively. Using the TS and TSscs schemes, C_6 coefficients and vdW radii are determined from ground state electron densities [38], whilst TSscs also includes long-range screening effects [39]. The TS and TSscs corrections will be applied to PBE, PBE0 and B3LYP.The vdW-DFs considered include the original vdW-DF which we refer to as revPBE-vdW [32], several optimized vdW functionals (optPBE-vdW [37], optB88-vdW [37], and optB86b-vdW [36]), and also vdW-DF2 [33].

3.3.2 Water and 1,2-azaborine Setup

The absolute interaction energy, E_{int}, that we refer to throughout this chapter is defined as,

$$E_{int} = E^{tot}_{com} - E^{tot}_{sub} - E^{tot}_{wat} \tag{3.1}$$

where E^{tot}_{com} is the total energy of the bound complex between water and the substrate (1,2-azaborine benzene or borazine), and E^{tot}_{sub} and E^{tot}_{wat} are the total energies of relaxed substrate molecule and water, respectively.

In 1,2-azaborine the electronic environment of individual carbon atoms differs due to the asymmetry introduced through the boron and nitrogen atoms. We use the numbering scheme shown in Fig. 3.1(a) to make the distinction between the atoms.

We obtained three distinct orientations of water over 1,2-azaborine using PBE-D2[1] in order to carry out the benchmarking study, namely C3, C5 and C5C3, also depicted in Fig. 3.1. The nomenclature of the complexes refers to the specific carbon atoms involved in hydrogen bonding, keeping in line with the numbering scheme in Fig. 3.1(a). The hydrogen atoms of water point toward carbon-3 and carbon-5 in all three complexes; most likely as a result of the higher electron charge around these carbon atoms due to the conjugation of the localized lone pair of electrons from the nitrogen atom. Indeed, Bader analysis shows that carbon-3 and carbon-5 have a larger atomic volume compared to carbon-2 and carbon-4, as

[1] A 10 Å long cubic cell was used with standard PBE PAW potentials and a 500 eV cut-off energy. Convergence criteria of 10E-6 eV for the wavefunction optimization and 0.01 eV/Å for the forces were used.

a result of increased electron charge around them. Some characteristic structural parameters are listed in Table 3.1 for the three different configurations. Although the PBE-D2 geometries are not benchmark accuracy, there have been various studies on polymer crystals and layered materials [190–192], and even for water on graphene [64], indicating that PBE-D2 can provide reasonable structures for weakly interacting systems.

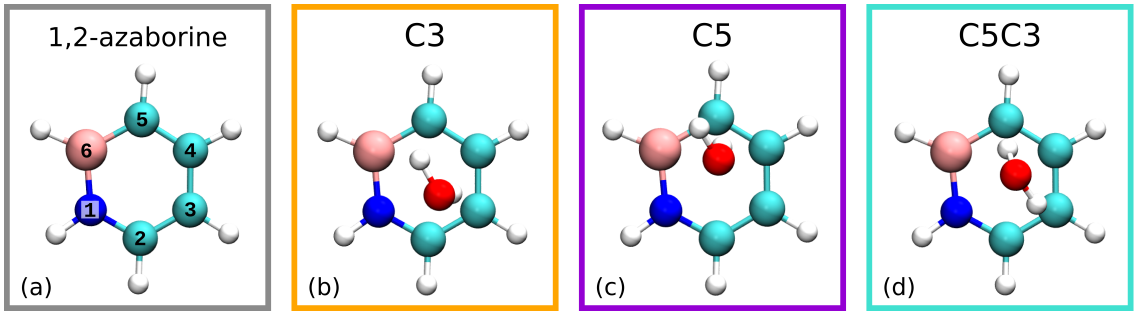

Figure 3.1: (a) 1,2-azaborine molecule: the carbon atoms are numbered according to their positions, nitrogen being 1 and boron being 6. The three distinct binding configurations of water (oxygen in red and hydrogen in white) on 1,2-azaborine are: C3 (b), C5 (c), and C5C3 (d).

Table 3.1: Perpendicular separation distances (in Ångstrom) of the oxygen atom to the plane of the 1,2-azaborine ring ($R_{O\text{-plane}}$), and hydrogen atoms of water to C3 and C5 ($R_{HW\text{-}C3}$ and $R_{HW\text{-}C5}$). The shortest C-H distance is reported in each case.

	C3	C5	C5C3
$R_{O\text{-plane}}$	3.24	3.22	3.15
$R_{HW\text{-}C3}$	2.44	4.42	2.75
$R_{HW\text{-}C5}$	3.50	2.39	2.51

3.4 Results and Discussion

3.4.1 Stability Trends for water on 1,2-azaborine

We computed benchmark absolute interaction energies for the three water adsorption complexes (C3, C5, and C5C3) using ΔCCSD(T). The results for ΔCCSD(T) have been extrapolated to the CBS limit and the computed interaction energies reveal that C3 is the most stable binding configuration with an interaction energy of −155 meV, followed by C5 (−146 meV) and C5C3 (−143 meV), as listed in Table 3.2.

The interaction energies we computed with DMC are in good agreement with ΔCCSD(T); within 14 meV depending on the adsorption structure considered and the TW used. This level

of agreement is in line with several recent studies in which DMC has been compared to coupled cluster [63, 118, 154, 193]. The small difference between DMC and ΔCCSD(T) interaction energies could be due to issues such as the use of PPs and the grid multiplicity for B-splines in DMC, the fixed node approximation in DMC, or the approximations used to obtain the ΔCCSD(T) values (including CBS extrapolation) [167]. Previously, Nolan *et al.* [194] did a careful study of using additive corrections to the basis set from MP2 for CCSD(T) for LiH clusters. It was found to be ~ 2 meV per formula unit, indicating that only a small error is introduced by this method.

With regard to the relative stabilities of the complexes, the DMC results suggest the same trend as ΔCCSD(T): C3 is more stable than C5 and C5 is more stable than C5C3. Considering the statistical error bars for each DMC interaction energy however, C3 and C5 could be degenerate according to DMC with LDA TWs. Whilst with PBE TWs, C3 is 9 meV more stable than C5, indicating a better trend prediction with the latter. Note the total energies using LDA TWs are slightly lower than those obtained with PBE TWs [2] and since DMC is a variational method, we consider the interaction energies with LDA TWs to be slightly more reliable in this particular system. Therefore, once again, it appears that DMC is useful for obtaining reliable interaction energies, but there is also an inherent difficulty in using a stochastic method like DMC, to clearly distinguish between complexes with very small energy differences.

If we now consider the results obtained from the various DFT xc functionals, we find that the trend obtained is in stark contrast to the benchmark ΔCCSD(T) results; with GGA and dispersion inclusive xc functionals showing preference for C5 instead of C3. However, before discussing this in detail, we analyze the performance of the xc functionals in terms of absolute interaction energies, and compare to ΔCCSD(T) as illustrated in Fig. 3.2. For the most stable C3 complex the best agreement with ΔCCSD(T) is given by optB88-vdW, optB86b-vdW, and optPBE-vdW: remarkably less than 3% errors. The other vdW functionals do not perform as well, with vdW-DF2 underbinding by 15% and revPBE-vdW underbinding by 25%. As anticipated, PBE is strongly underbinding by almost 35% due to the lack of long-range correlation, whilst dispersion corrected PBE-D2 overestimates the binding by 20%. The

[2] The LDA TWs give rise to total energies that are $\sim$ 20–30 meV lower than total energies obtained from PBE TWs, whereby the total energies are in the region of $\sim$ 1500 eV.

Table 3.2: Absolute interaction energies in (meV) of water on 1,2-azaborine, using the structures shown in Fig. 3.1. The benchmark values from ΔCCSD(T) are presented in addition to DFT, HF, MP2 and DMC results. Lowest energies for each method are highlighted in bold.

Methods	C3	C5	C5C3
PBE	−98	**−110**	−87
PBE-D2	−188	**−196**	−195
PBE+TS	−168	**−174**	−169
PBE+TSscs	−162	**−169**	−161
revPBE-vdW	−115	**−127**	−96
optPBE-vdW	−159	**−170**	−148
optB88-vdW	−154	**−164**	−148
optB86b-vdW	−157	**−167**	−150
vdW-DF2	−134	**−143**	−122
$PBE0^{0.25}$	−105	**−110**	−92
$PBE0^{0.50}$	**−114**	−112	−100
$PBE0^{0.75}$	**−124**	−116	−109
$PBE0^{0.25}$+TS	**−174**	−173	**−174**
$PBE0^{0.25}$+TSscs	**−168**	**−168**	−165
$PBE0^{0.75}$+TS	**−191**	−177	−190
$PBE0^{0.75}$+TSscs	**−181**	−168	−178
$B3LYP^{0.20}$	−65	**−73**	−46
$B3LYP^{0.40}$	−95	**−97**	−78
$B3LYP^{0.60}$	**−125**	−121	−110
$B3LYP^{0.20}$+TSscs	−128	**−131**	−120
$B3LYP^{0.60}$+TSscs	**−187**	−178	−183
HF	**−22**	−8	+15
MP2/CBS	**−164**	−157	−152
DMC (Ψ_{LDA})	$\mathbf{-158 \pm 5}$	-141 ± 2	-132 ± 3
DMC (Ψ_{PBE})	$\mathbf{-143 \pm 3}$	-134 ± 3	-129 ± 3
ΔCCSD(T)/CBS	**−155**	−146	−143

TS and TSscs corrections perform significantly better than the D2 correction, with only 10% and 5% errors, respectively.

One can see from Fig. 3.2 that the percentage error lines across C3, C5, and C5C3 have a very similar form, but they shift with regard to the reference ΔCCSD(T) binding energy. This means that for the C5 complex vdW-DF2 is providing the best agreement with ΔCCSD(T) (2% error) and the optimized vdW functionals are overbinding by 10–15%. Whereas for C5C3, the xc functionals perform in a similar manner as for C3, with the optimized vdW functionals performing the best once again (< 5% error). Of PBE and its dispersion corrected forms, PBE+TSscs performs the best for all three complexes (underbinding by 5-15%). Note that MP2 consistently overbinds all three structures by $\sim 9\%$.

Regardless of the absolute interaction energies of PBE, dispersion corrected PBE and the

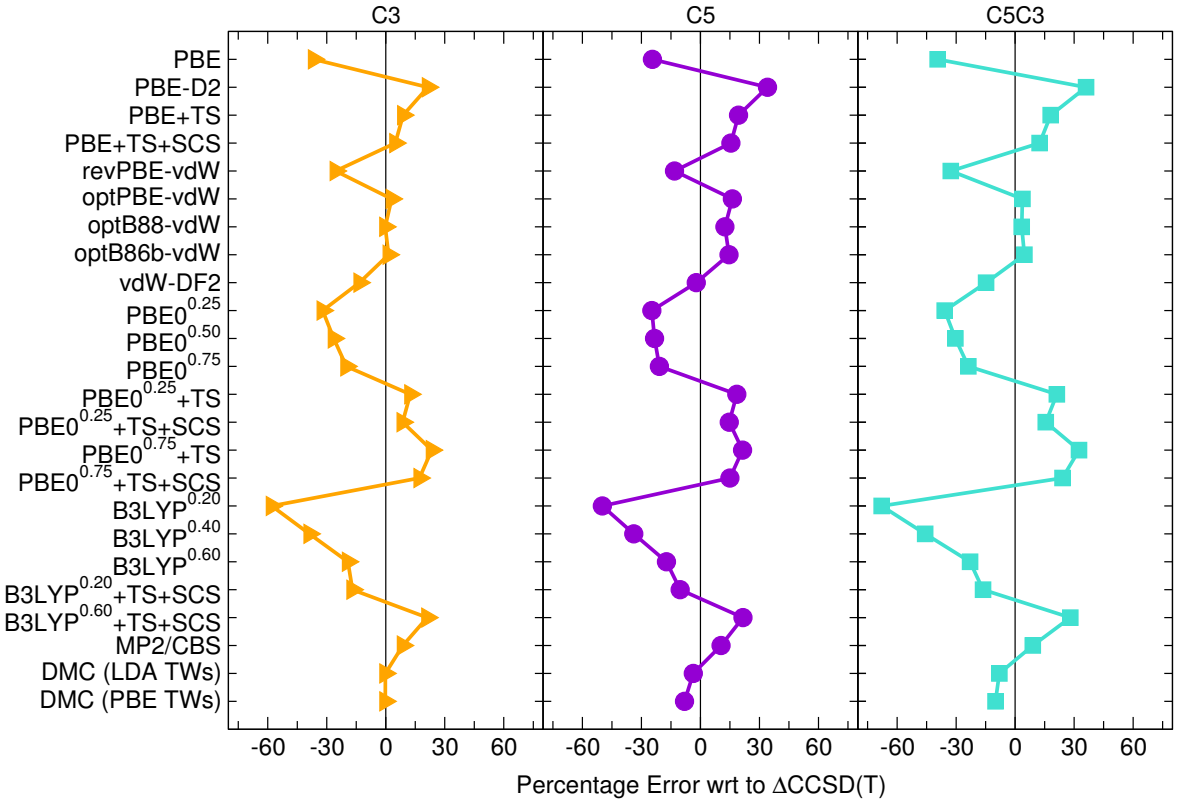

Figure 3.2: The percentage difference between ΔCCSD(T) interaction energy and that from DMC, MP2 and the various DFT xc functionals, of water to 1,2-azaborine. The solid black lines at zero represent the ΔCCSD(T) reference. Note that DMC results with both LDA (Ψ_{LDA}) and PBE (Ψ_{PBE}) TWs are reported and that the HF results are off the chart. The superscripts for the hybrid PBE0 and B3LYP functionals indicate different proportions of exact exchange.

non-local vdW functionals, they all fail to predict C3 as the most stable complex. In addition, the TS and TSscs corrections are not satisfactory as they stabilize the C5C3 complex such that it becomes degenerate with either C3 or C5. Clearly with a fairly flat potential energy surface, the difference between C3 and C5 is a considerable challenge for the xc functionals. According to the benchmark ΔCCSD(T) values, C5 is only 9 meV less stable than C3, making it difficult to assign the source of error that leads to so many different xc functionals predicting the wrong trend.

One possible source of error is an inadequate description of exchange and to address this we initially performed HF calculations. We find that with HF the trend is correctly predicted with C3 as the most stable configuration, despite the lack of correlation and highly underestimated interaction energies. The HF results suggest that the lack of exact exchange is perhaps the main reason for many of the xc functionals predicting C5 instead of C3. For

further insight, HF symmetry adapted perturbation theory (HF-SAPT) calculations revealed that it is the exchange-repulsion energy (mostly electrostatic) that puts the binding energy in favor of C3 and not C5.

Guided by this insight, we computed binding energies using the hybrid PBE0 and B3LYP functionals with varying amounts of exact exchange. The results are listed in Table 3.2 with the proportion of exact exchange indicated by the superscripts, along with hybrid functional results corrected with the TS and TSscs vdW schemes. In addition, Fig. 3.3 shows how the interaction energies of the C3 and C5 complexes vary with the proportion of exact exchange with PBE0-like functionals. Using standard PBE0$^{0.25}$ the lowest energy complex is C5, but

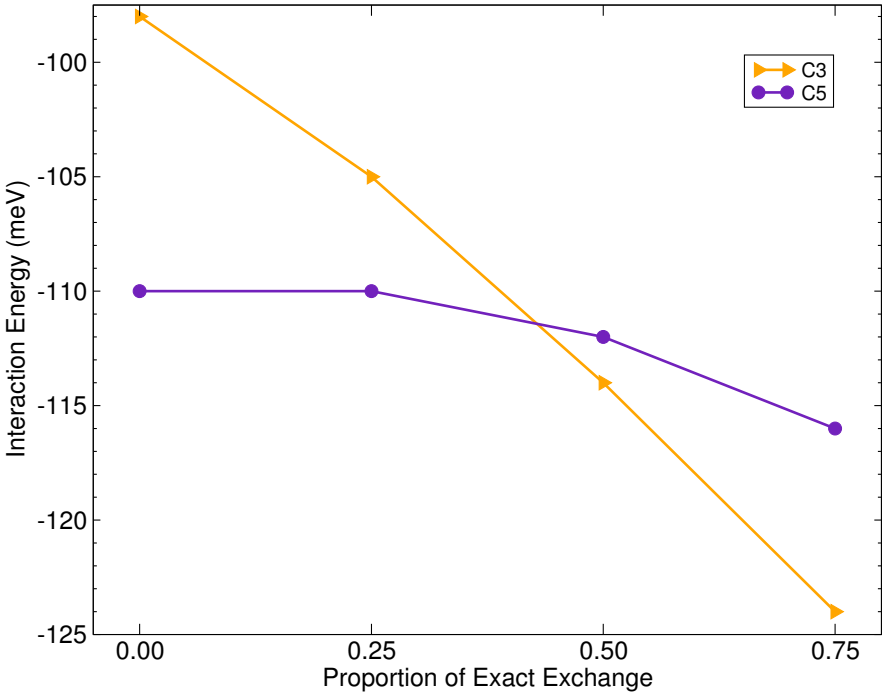

Figure 3.3: The interaction energy of the C3 and C5 complexes are plotted against the proportion of exact exchange in PBE0-style calculations, with zero exact exchange corresponding to PBE.

as the percentage of exact exchange is increased to 50% and above, C3 becomes the most stable complex. Similarly with B3LYP, 60% exact exchange is needed in order to switch the site preference to C3. However PBE0$^{0.75}$ and B3LYP$^{0.60}$ still underbind by 20% with respect to ΔCCSD(T), and including the TSscs corrections leads to overbinding by the same amount. The combination of the hybrid functionals with TS and TSscs corrections tends to decrease the energy differences between the different configurations. Depending on the particular combination of exact exchange and TS-like dispersion, both C3 and C5 can be degenerate or

almost degenerate or even all three structures can be almost degenerate. Overall we learn from these various calculations that a high proportion of exact exchange improves the relative energies of the various structures. However, still, in the future a more refined description of long-range correlation and exchange is needed in order to predict the correct trend and absolute interaction energies.

A change in the stability trend of weakly interacting complexes due to the amount of exact exchange is not limited to the systems studied here; Thonhauser *et al.* [162] observed a similar distortion in the ordering of conformers in their study of monosubstituted benzene dimers, which they corrected by using HF exchange. The need for a very high fraction of exact exchange in xc functionals to give correct predictions warrants further discussion. We have very carefully looked at the electronic structures obtained from the various functionals for the different complexes and a thorough inspection of the individual energy contributions to the absolute interaction energies was particularly informative. By decomposing the interaction energies into the kinetic, potential, Hartree, exchange and correlation energies, we have analyzed the effect of increased exact exchange on the individual energy contributions for C3 and C5. We find that the main distinguishing feature between C3 and C5, is that the kinetic energy and the repulsive terms (Hartree and exchange energies) change to different extents as the fraction of exact exchange is increased. Kinetic energy favors C5 but with a high fraction of exact exchange, the C3 complex is stabilized by less repulsion (Hartree and exchange) than in C5. This observation is in accord with the HF-SAPT results mentioned earlier.

It is known that exact exchange localizes the electrons and alleviates the surplus delocalization which is otherwise present in standard GGA calculations. The localization of electrons determines the electron density distribution over a system and therefore determines the interaction sites within complexes. In addition to orbital overlap, hydrogen bonding and dispersion interactions are also both affected by a change in the electron density distribution. The interactions in our water/1,2-azaborine complexes have contributions from hydrogen bonding, dispersion interactions and weak orbital mixing. We have seen that the delicate balance between such interactions is sensitive to the relative contributions from individual energy terms, prompting the need for both exact exchange and a good description of the correlation energy for the reliable prediction of configurations in weakly interacting systems, such as ours.

3.4.2 From benzene to borazine

Thus far we have studied the interaction of a water monomer with the intermediate 1,2-azaborine molecule as a model for boron nitride doped graphene. We have found that an inadequate description of exchange in xc functionals can alter the binding orientation, despite reasonable interaction energies being predicted by some of the vdW xc functionals. Here we establish whether xc functionals without exact exchange can correctly describe the interaction between the water monomer and the pure counterparts of 1,2-azaborine: benzene and borazine ($B_3N_3H_6$). It is also useful, from a materials design perspective, to understand how the boron nitride doping affects the interaction with water, compared to graphene and h-BN; which can be mimicked to some extent by benzene and borazine, respectively. Adhering to the use of model systems allows us to compare interaction energies from DFT and benchmark CCSD(T) calculations. To this end, we have examined water on benzene and borazine and we find that in contrast to 1,2-azaborine, these pure systems are much less challenging, with different functionals able to predict the same orientation as obtained in previous benchmark calculations [151, 152, 155]. Previous work has shown that water tilts towards a carbon atom in benzene, and the complex has an absolute interaction energy of −145 meV calculated with CCSD(T) [151, 152]. Similarly, in the water-borazine complex, water tilts towards a nitrogen atom and the CCSD(T) interaction energy reported by Wu *et al.* [155] is −92 meV. In Chapter 5 the ΔCCSD(T) energy with CBS extrapolation is computed for water-borazine to be −119 meV. We have relaxed several starting geometries of the water-benzene and water-borazine complexes with PBE and optB86b-vdW and the absolute interaction energies are shown in

Table 3.3: Absolute interaction energies of water to benzene, 1,2-azaborine, and borazine using PBE, optB86b-vdW, vdW-DF2 and CCSD(T). The absolute interaction energies with DFT correspond to optimized structures, and the values for water-1,2-azaborine correspond to the C3 complex.

Methods	H_2O/Benzene	H_2O/1,2-azaborine	H_2O/Borazine
PBE	−108	−109	−85
optB86b-vdW	−142	−160	−122
vdW-DF2	−137	−155	−129
CCSD(T)	−145[a]	−155[b]	−119[c]

[a] CCSD(T) interaction energy by Min *et al.* with CBS extrapolation [152].
[b] ΔCCSD(T) interaction energy calculated in Section 3.4.1 for the C3 complex.
[c] ΔCCSD(T) interaction energy computed in Chapter 5 with CBS extrapolation. Wu *et al.* [155] computed CCSD(T) interaction energy without CBS extrapolation to be −92 meV.

Table 3.3. For the water-benzene complex, PBE underbinds as previously shown [153], whilst optB86b-vdW performs very well: only 2% error compared to the benchmark. Moreover with PBE, there is almost no distinction between water binding to benzene or 1,2-azaborine, but using the dispersion inclusive optB86b-vdW, the binding on 1,2-azaborine is almost 20 meV stronger. Similarly using CCSD(T), our benchmark absolute interaction energy of the C3 complex (−155 meV) is 10 meV stronger than the absolute interaction energy of water to benzene (−145 meV calculated by Min *et al.* [152]). On borazine the absolute interaction energy is weaker according to all methods: PBE (−85 meV), optB86b-vdW (−122 meV) and also with CCSD(T) (−119 meV). In all cases, the water tilts towards nitrogen in the borazine ring [155] and this tilting, that also occurs on 1,2-azaborine and benzene, is indicative of a weak hydrogen bond forming in all three complexes. Not only do PBE and optB86b-vdW obtain the correct binding orientations for water on benzene and borazine, but also optB86b-vdW yields only a 2–3% error for the water-benzene and C3 complexes. For completeness, we also include the results obtained with vdW-DF2 in Table 3.3, which are similar to those obtained with optB86b-vdW. Using vdW-DF2 the error for water-benzene is 5% and for the C3 complex the binding energy agrees with the benchmark. Even so, the wrong orientation is predicted by PBE, optB86b-vdW and vdW-DF2 for water binding to 1,2-azaborine as discussed in Section 3.4.1. Therefore, the prediction of binding sites with weak interactions on doped surfaces and between complex organic molecules could be compromised by an inadequate description of exchange, whilst being correct in pure systems.

Finally, it is interesting to note that water interacts more strongly with the intermediate 1,2-azaborine molecule than either benzene or borazine. If upon doping graphene with boron and nitrogen a similar increase in the interaction with water was found then this could provide a means of tuning the strength of the water substrate interaction to have specific, targeted wetting properties.

3.5 Discussion and Conclusions

We have calculated three benchmark values of the absolute interaction energy between a water monomer and 1,2-azaborine using ΔCCSD(T) extrapolated to the CBS limit. The lowest energy complex according to the explicitly correlated, exact exchange methods (ΔCCSD(T),

DMC and MP2) is C3 with an absolute interaction energy of −155 meV from ΔCCSD(T). The DMC energies are, on average, within 6–8% of ΔCCSD(T). Meanwhile, xc functionals including PBE, dispersion corrected PBE and an array of vdW-DFs, fail to predict the same binding configuration as ΔCCSD(T), MP2 or DMC. Instead, these xc functionals indicate that C5 is the lowest energy complex. Although interatomic many-body dispersion (MBD) forces have previously been shown to be neglected or wrongly described in DFT xc functionals [195], HF and HF-SAPT calculations demonstrate that in this case, exact exchange corrects the trend without including MBD forces; thus we can deduce that MBD is not a source of error for the stability trend. Previous work has shown that for strongly interacting systems, like CO on Pt(111), exact exchange improves the alignment of electronic states between the substrate and the adsorbate and to recover the experimental chemisorption site [196]. Also, for defects in semiconductors, exact exchange is a crucial factor in finding the correct defect states (see e.g. ref 197). Here, it is demonstrated that exact exchange and the associated changes to the electronic structure plays a decisive role in the prediction of the lowest energy configuration for weakly interacting (asymmetric) complexes. As such, it is imperative that more emphasis is placed on the accurate treatment of exchange when using DFT to examine weakly bound complexes and adsorption. The wrong prediction of the configuration for our relatively small system of water on 1,2-azaborine suggests that the delocalization error is likely to be even more pervasive for larger systems with more shallow energy minima, such as for physisorption on doped surfaces and in crystal polymorph prediction.

In terms of the absolute interaction energies, however, the inclusion of dispersion interactions is essential for weakly bound systems, and in the systems studied here this is more accurately achieved by non-local vdW functionals than dispersion corrected PBE, PBE0 and B3LYP. By comparing absolute interaction energies, we determined that optB88-vdW and optB86b-vdW are generally the best performing xc functionals from those tested. Our findings imply that in order to predict the correct binding configuration as well as the energy, DFT xc functionals must simultaneously contain exact exchange (so as to avoid delocalization error) and account for dispersion interactions. However, even with dispersion corrected hybrid functionals we were not able to obtain a perfect trend or accurate interaction energies; echoing the need to develop xc functionals that contain a better description as well as balance, of both exchange and non-local correlation [100].

Finally, we have found that water binds more strongly to the intermediate system, 1,2-azaborine than to either benzene or borazine. Should equivalent behavior be observed on doped graphene surfaces, then this could represent a means of tuning the binding and wetting of interfacial water to graphene and h-BN. In future work we will focus on exploiting this possibility.

Chapter 4

Establishing the adsorption energy of water on h-BN from DMC

4.1 Abstract

Despite a recent flurry of experimental and simulation studies, an accurate estimate of the interaction strength of water molecules with hexagonal boron nitride (h-BN) is lacking. Here, quantum Monte Carlo results are reported for the adsorption of a water monomer on a periodic h-BN sheet. This yields a water monomer interaction energy of -84 ± 5 meV in a (4×4) unit cell of h-BN. The results are used to evaluate the performance of several widely used density functional theory (DFT) exchange correlation functionals, and it is found that they all deviate substantially. Differences in interaction energies between different adsorption sites are however better reproduced by DFT.

4.2 Introduction

Hexagonal boron nitride (h-BN) has become popular for anyone with an interest in 2-dimensional materials, due to a number of notable properties such as high thermal conductivity, mechanical robustness and exceptional resistance to oxidation [198], and not least because it is isostructural with graphene. Our interest has been piqued by experimental reports of fascinating behavior of water at h-BN such as superhydrophobicity [199], water cleaning ability [3] or generation of electric current [10]. These experiments have already prompted a number of

simulation studies of water on h-BN sheets and nanostructures using both density functional theory (DFT) and classical molecular dynamics [138, 200–205]. They have been incredibly informative and have helped to e.g. understand the electrical currents generated in BN nanotubes [10].

However, there is one major unknown at the very heart of any water/BN simulation study: we simply do not know what the interaction strength of a water molecule with h-BN is. DFT calculations yield a range of values for the water monomer adsorption energy depending on the exchange-correlation (xc) functional used [138, 200, 201] and force fields rely on interaction parameters fitted to particular xc functionals or to experimental data such as contact angles for macroscopic water droplets [202–205]. If fitting to experiment, one needs to be certain that the experimental conditions are exactly known; recent lessons learned for water droplets on graphene reveal that contact angle measurements are incredibly sensitive to surface preparation conditions and levels of cleanliness [141, 143, 144, 206].

The lack of well-defined reference data for water on h-BN is representative of a much broader problem: there are very few systems for which accurate water monomer adsorption energies have been established. Mainly this is because even at low temperatures water molecules cluster into larger aggregates making the determination of monomer adsorption energies with established surface science techniques such as temperature programmed desorption or single crystal adsorption calorimetry highly challenging [207–209]. In the absence of experimental data, simulations play an important role, either via explicitly correlated quantum chemistry approaches or quantum Monte Carlo (QMC) (see *e.g.* references 63, 64, 69, 145, 210–212). Indeed given recent increases in computational capacity and the fact that it can be applied to periodic systems, QMC has emerged as a powerful technique for obtaining interaction energies of molecules with surfaces [63, 69] or biomolecules [118, 193, 213].

In this chapter, results for interaction energy curves for water on a periodic h-BN sheet using fixed node diffusion Monte Carlo (DMC) are reported. From this an estimate of the water/h-BN interaction strength of about -84 ± 5 meV at an equilibrium water-surface distance of *ca.* 3.4 Å has been obtained. Also, interaction energy curves with a variety of DFT xc functionals have been computed and these are found to differ significantly from DMC. Except for LDA, of the functionals considered those that do not account for van der Waals underbind and those that do, overbind. DFT based predictions of the equilibrium adsorption

height are much better with several functionals coming within 0.2 Å of DMC. In addition, based on DMC and DFT calculations of water on h-BN in a second metastable adsorption structure, we find that many of the xc functionals do reasonably well in predicting the relative energy difference between the stable and metastable adsorption structures.

4.3 Methods

Two different levels of theory have been used in this chapter, fixed node DMC and DFT. A standard computational setup has been used for each and so only the key features are discussed here. QMC calculations were undertaken using the CASINO code [175], with Slater-Jastrow type trial wavefunctions in which the Jastrow factor contains electron-nucleus, electron-electron, and electron-electron-nucleus terms. Trail and Needs pseudopotentials [170, 171] were used for all atoms, in which the 1s electrons of B, N, and O were treated as core. This set-up for the DMC calculations is similar to the one used in Chapter 3 (and Ref. 213) where water adsorption was examined on 1,2-azaborine and agreement between DMC and coupled cluster with single, double and perturbative triple excitations (CCSD(T)) to within 9 meV was obtained. The initial single particle wavefunctions for use in DMC were obtained from DFT plane-wave calculations using the PWSCF package [169]. A standard 300 Ry energy cut-off was applied and for efficiency the resulting wavefunctions were expanded in terms of B-splines [174] using a grid multiplicity of 2.0. Trial wavefunctions were generated using the local density approximation (LDA) [172] which has been validated for weak interactions in previous work [154, 213]. After optimization of the trial wavefunctions in variational Monte Carlo, 6,553,840 walkers were used across 16,384 cores for each point along the DMC interaction energy curves. The locality approximation was utilized [176] with a time step of 0.015 a.u. which was tested against a time step of 0.005 a.u.

VASP 5.3.5 [177–180] was used for the DFT calculations, making use of projector augmented wave (PAW) potentials [181, 182] to model the core regions of atoms (again the 1s electrons of B, N, and O were treated as core). Following careful tests, a 500 eV plane-wave cut-off was chosen and a (4×4) unit cell of h-BN with 16 Å between sheets, along with Γ-point sampling of reciprocal space.[1] The proliferation of DFT xc functionals over the last decade

[1]For example, tests with a higher plane-wave cut-off (600 eV) and denser **k**-point mesh $(5\times5\times1)$ performed for the PBE functional yielded an interaction energy that differed from the reported one by < 3 meV. Similarly

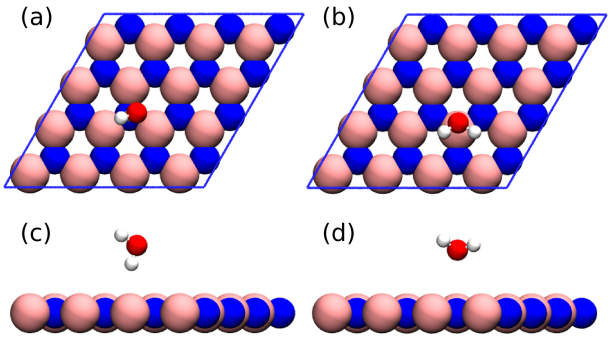

Figure 4.1: Structures of the two adsorption modes of water on h-BN considered in this study. (a,c) Top and side view of water above an N site of h-BN. (b,d) Top and side view of water above a B site of h-BN. Boron is pink, nitrogen is blue, oxygen is red and hydrogen is white. All calculations have been performed on periodic unit cells, with the periodic unit cell in the x,y plane indicated by the blue frames in (a) and (b).

[99] means that it is not feasible to consider all xc functionals or even all modern xc functionals designed to capture weak interactions. Rather we consider a small selection that have been widely used in adsorption studies. This includes the LDA, the PBE [173] generalised gradient approximation (GGA), two hybrid functionals (PBE0 [183, 184] and B3LYP [185–188]), and several van der Waals (vdW) inclusive functionals (PBE+D2 [189], PBE+D3 [34, 35], DFT+TSscs [38, 39], optB86b-vdW [32, 36, 214] and vdW-DF2 [32, 33]). The DFT+TSscs correction (from Tkatchenko and Scheffler) was applied to three xc functionals (PBE, PBE0 and B3LYP).

Results for interaction energy curves of a water monomer on h-BN in two different adsorption modes (Figure 4.1), obtained from DMC and a range of DFT xc functionals, are shown in Figure 4.2. The interaction energy between the adsorbate and substrate is plotted as a function of the perpendicular distance between the oxygen atom of the water molecule and the h-BN sheet. The absolute interaction energy between water and the substrate were calculated as follows,

$$E_{int} = E_d^{tot} - E_{\text{far}}^{tot} \tag{4.1}$$

where E_d^{tot} is the total energy of water and h-BN at a given oxygen-surface separation distance, d, and E_{far}^{tot} is the total energy of water and h-BN at 8 Å oxygen-surface distance. This definition allows the same Jastrow factor to be used for all configurations, including the

when the current set-up was tested for water adsorption on the 1,2-azaborine system considered in Ref. 213 against all-electron PBE calculations with an aug-cc-pV5Z basis set we found that the results with the two approaches differed by only 1 meV; the PBE adsorption energy for that system being 109-110 meV.

reference structure in DMC. Adsorption structures were obtained from optB86b-vdW optimizations of water on a fixed h-BN sheet. The same structures were chosen for DMC and all xc functionals because this makes for a cleaner comparison. For many of the xc functionals interaction energy curves with fully relaxed structures have been computed and the differences between the relaxed and the fixed structures are < 5 meV, except in the repulsive wall at short oxygen-surface separations. The first adsorption structure considered has the oxygen of the water molecule above an N site with one of the OH bonds directed at that N atom (Figure 4.1(a,c)). This is the most stable adsorption structure according to previous DFT studies [200]. The second structure has the oxygen atom of the water molecule above a B site with the plane of the molecule tilted away from the substrate by 128° (Figure 4.1(b,d)). According to DFT calculations this is the most stable structure for water at the B site but ~ 20 meV less stable than the N site adsorption structure. Water adsorption at the B site is considered to establish if the DFT site preference for this system is correct [109].

4.4 Results

Let us now focus on the DMC interaction energy curves for water on h-BN. Because of the enormous computational cost of DMC only a small number of points can be computed for each energy curve, which limits the resolution of the curves. Nonetheless they are sufficiently well defined to yield an adsorption energy of -84 ± 5 meV at a height of ~ 3.4 Å at the N site and an adsorption energy of -63 ± 5 at a height of ~ 3.2 Å at the B site. The O atom sits slightly further away from the substrate at the N site because of the orientation of the molecule at this site, wherein the H atoms points to the N, forming a weak hydrogen bond like interaction. The relative energies of the two sites confirms the DFT site preference but more importantly provides an estimate of the water monomer interaction energy that is free of any arbitrary choices of DFT xc functional.

Obtaining an accurate estimate of the interaction strength between water and h-BN is important in its own right, however, it also provides a valuable benchmark which we now exploit. Here, the DMC derived interaction energy curves are used to evaluate how various DFT xc functionals perform for this system. Interaction energy curves from several functionals are included in Figure 4.2 and in some respects these reveal a familiar story. Looking at

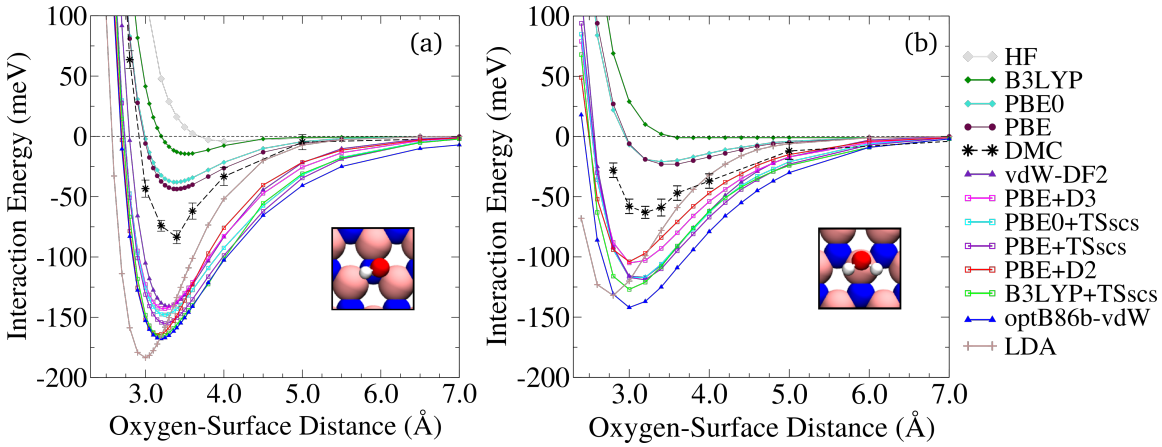

Figure 4.2: (a) Interaction energy curves for water situated above the N site in h-BN as shown in the inset. (b) Interaction energy curves for water situated above the B site in h-BN as shown in the inset. The lines connecting the data points are merely there to guide the eye.

the most stable site first, LDA overbinds by predicting an adsorption energy of −183 meV with the molecule 0.4 Å closer to the surface than DMC. In contrast the GGA and the hybrid functionals underbind: PBE is ~ -45 meV, PBE0 is ~ -40 meV and B3LYP is ~ -15 meV. The PBE and PBE0 adsorption heights are fairly reliable at 3.40 Å whereas the shallow B3LYP minimum is located at 3.55 Å. More interesting are the results from the vdW inclusive functionals since these are in principle designed to accurately describe weak interaction systems. Surprisingly, all vdW inclusive functionals considered significantly overbind this adsorption system. Specifically the adsorption energies are in the −140 to −170 meV range, with vdW-DF2 predicting the smallest adsorption energy and optB86b-vdW the largest. This overbinding also persists at large adsorbate-substrate distances; compare for example the DMC and vdW-inclusive DFT results at $4-5$ Å from the surface. The predicted height above the surface is in reasonably good agreement with DMC, only around 0.1 Å closer to the surface for all vdW-inclusive functionals.

Moving to the B site adsorption structure it is found that systematically, with the exception of PBE+D2, the interaction strength is reduced by $\sim 20-30$ meV. This is in very good agreement with the DMC energy difference between these two sites (PBE-D2 predicts that the B site is ~ 60 meV less stable than the N site). Thus although none of the xc functionals considered come within 40% of the DMC interaction energy, the change in interaction energies between adsorption sites are in most cases described fairly accurately. Note that only two adsorption structures have been considered and considerably more work is needed to

fully substantiate this conclusion. Moreover, at this stage the poor performance of the vdW functionals is not entirely understood, and further investigation follows in Chapter 5 using BN molecules as well as h-BN.

4.5 Conclusion

In summary, DMC interaction energy curves have been obtained for water on a periodic hexagonal sheet of BN and used these to evaluate the performance of a number of xc functionals. The interaction energy obtained is -84 ± 5 meV. This is clearly a small number; corresponding to the physisorption regime.[2] It is, however, about 15 meV larger than the value predicted by DMC for water on graphene. Interestingly many of the van der Waals inclusive functionals also predict a similar 15–20 meV increase upon going from graphene to h-BN [69, 200]. This suggests that although interaction energies are overestimated with these functionals, the relative interaction energies between the two materials are fairly well described. Finally let us note that the reference interaction energy calculated here is for a (4×4) unit cell of h-BN. The impact of any long-range correlation that may not be captured by this unit cell size is studied in the following chapter.

[2] Zero point energy contributions (computed within the harmonic approximation) weaken the optB86b-vdW interaction strength by ~ 30 meV. Since this is the most strongly binding xc functional, others are likely to show a smaller reduction than this.

Chapter 5

Further insights from water adsorption on BN substrates

5.1 Abstract

In the past, agreement between high accuracy *ab initio* methods has mostly been demonstrated for small, molecular systems. Much less is known about how methods such as the RPA, DMC and MP2 compare for extended systems. Here, reference DMC adsorption energies for water on BN substrates are used as a case study to understand and quantify important approximations in quantum chemistry and to the RPA. Molecular BN substrates are used to gauge the performance of the RPA, MP2, CCSD(T), DMC and a selection of widely used xc functionals. In addition, calculations with a series of h-BN unit cells of up to 98 atoms, are used to establish the contribution from long-range correlation interactions on the 2-dimensional BN surface. These are found to scale as $1/N^{3/2}$ with N being the number of atoms, and result in a 25% increase in the water-surface adsorption energy, giving a corrected DMC adsorption energy of -104 ± 5 meV. In addition, the many-body dispersion method emerges as a particularly useful estimation of finite size effects for other expensive, explicitly correlated methods.

5.2 Introduction

Great progress in developing algorithms has enabled surface adsorption problems to become increasingly accessible computationally [59, 62–71]. Water adsorption on graphene is an exemplary case that has been computed with RPA, DMC [63] and CCSD(T) [64]. However the reported adsorption energies range by up to 40%; likely because the calculations still involved a number of limitations and approximations which have not been quantified.

Gauging the impact from different approximations is evidently desirable and would allow for greater understanding of the necessary corrections to the methods. To this end, we focus on water interaction with BN substrates which are geometrically analogous to carbon substrates but have more insulating electronic structures. Like graphene, the 2-dimensional BN surface gives rise to long range Coulomb interactions that are relevant to adsorption on low-dimensional systems [104]. In addition, it is especially important to understand how water interacts with the surface since water is ubiquitous. Even the gecko which is known for climbing walls by adhesion from vdW interactions, has been found to lose its grip when its toepads become wet [215–217].

Here, periodic RPA, DMC and MP2 calculations are used to ascertain the best possible adsorption energy for water on the h-BN sheet. Importantly, these systems are used to establish: (i) the size of the single excitations (SE) correction in RPA interaction energies for both molecular and extended BN substrates; and (ii) the contribution from long-range correlation for water/h-BN and its convergence with different methods, including the many body dispersion (MBD) correction [40, 218] in DFT. In what follows, the MBD correction is found to agree with RPA, indicating that it can be used as an efficient approach for estimating the contribution from long-range correlation interactions. In addition, a number of DFT exchange-correlation functionals are benchmarked for this set of water/BN substrates and shown to vary in performance across the length-scales; with worsening performance as the substrate size increases.

Details of the calculations and set-up are given first in Section 5.3 followed by results in Section 5.4. In Section 5.4.1 the interaction energy curves for a water monomer with borazine (BN analogue of benzene, $B_3N_3H_6$) and boronene (BN analogue of coronene, $B_{12}N_{12}H_{12}$) are reported. In Section 5.4.2 water/h-BN interaction energy curves from RPA and MP2 are given

(along with previous results from DMC). PBE+MBD is discussed in more detail in Section 5.5 and we close with conclusions in Section 5.6.

5.3 Methods

For this study, DFT, MP2, CCSD(T), the RPA and DMC have been employed. As such, many electronic structure codes have been employed with various settings that are detailed here.

First, for consistency, all of the DMC calculations in this chapter use the same settings as in the previous Chapter 4. As before, the locality approximation was utilized [176] with a time step of 0.015 a.u. which was tested against a time step of 0.005 a.u for the water/borazine interaction. In Table 5.1 the interaction energy can be seen to agree within the error bars for the 0.015 and 0.005 a.u. time steps.

The DFT calculations on the molecular BN systems have been conducted with the same settings as in Chapter 4: standard PAW potentials with a 500 eV plane-wave cut-off energy and Γ-point sampling of reciprocal space. A range of xc functionals are assessed in this chapter, namely: the LDA [172], PBE [173], PBE0 [183, 184], dispersion corrected PBE and PBE0 (D2 [189], D3 [34, 35], TSscs [38, 39], and MBD [40, 218]) and vdW-inclusive functionals (optB86b-vdW [36, 214], vdW-DF2 [33], and rev-vdW-DF2 [219]). We have also tested the more recently developed strongly constrained and appropriately normalised (SCAN) functional of Sun *et al.* [220]. In addition, M. Rossi calculated interaction energy curves for water/BN substrates with PBE+MBD and PBE0+MBD using the all-electron FHI-AIMS code [221].

The molecular systems were also calculated with quantum chemical codes (Gaussian [168], Molpro [222], and NWChem [223]) to obtain the MP2 interaction energy at 3.4 Å water/substrate distance, with complete basis set extrapolation using Dunning's aug-cc-pV(T,Q)Z basis sets. The CCSD(T) interaction energy of water/borazine at 3.4 Å was calculated using aug-cc-pV(T)Z basis set and by taking the difference with MP2 at this basis set, the ΔCCSD(T)/CBS interaction energy was estimated. For water/boronene, the MP2/CBS interaction energy was evaluated in the same way as for borazine. Due to a memory bottle-neck however only cc-pVDZ basis set was used in the CCSD(T) calculation of water/boronene at 3.4 Å. As such, an *ad hoc* ΔCCSD(T)/CBS interaction energy was

estimated for water/boronene. This was done by taking the difference between MP2 and CCSD(T) with a cc-pVDZ basis set as the correction to CBS extrapolated MP2 interaction energy.

For periodic calculations of the molecular water/borazine system, a $15\times15\times15$ Å^3 unit cell was used. With this unit cell, the effect of a dipole correction is negligible (<1 meV) in a PBE calculation with VASP. For the larger boronene molecule, a $20\times20\times16$ Å^3 unit cell was used. Periodic LMP2 calculations were undertaken by Theodoros Tsatsoulis and Andreas Grüneis for water on h-BN. After checking convergence, a 500 eV energy cutoff was employed for the one-particle HF states along with Γ-point sampling of the Brillouin zone. The cutoff energy for the auxiliary plane-wave basis set required for the evaluation of the two-electron four-orbital integrals [224] was set to 250 eV. Occupied HF states were converged within the full plane-wave basis, whereas the virtual orbitals were constructed using Dunning's contracted aug-cc-pVDZ and aug-cc-pVTZ [125, 225] pseudized Gaussians in a plane-wave representation, projected to the HF occupied states [226].

In addition, the RPA calculations reported in this chapter have been provided by Benjamin Ramberger and Georg Kresse. A developer version of VASP 5.4.2 was used following methods precribed in Refs. 227–229. PBE orbitals were used for the RPA calculations[1], using GW-optimised PAW potentials and 430 eV plane-wave energy cut-off.

The absolute interaction energy between water and the substrate were calculated as follows,

$$E_{int} = E_d^{tot} - E_{\text{far}}^{tot} \tag{5.1}$$

where E_d^{tot} is the total energy of water and substrate at a given oxygen-substrate separation distance, d, and E_{far}^{tot} is the total energy of water and substrate at 8 Å oxygen-substrate distance. This definition allows the same Jastrow factor to be used for all configurations, including the reference structure in DMC[2]. The one-leg configuration of water with H atom above a N atom in the substrate is used for each system because this makes for a cleaner comparison (see Fig. 5.1). The interaction energy between water and substrate is plotted as a function of the perpendicular distance between the oxygen atom of the water molecule and

[1]Differently to current default settings in VASP, NOMEGA = 8 was set and PRECFOCK = Normal for the RPA calculations.

[2]In the MP2 and RPA calculations for water/h-BN, there is a residual 6 meV interaction at 3.25 Å compared to taking the interaction energy with respect to a gas-phase water molecule and isolated surface.

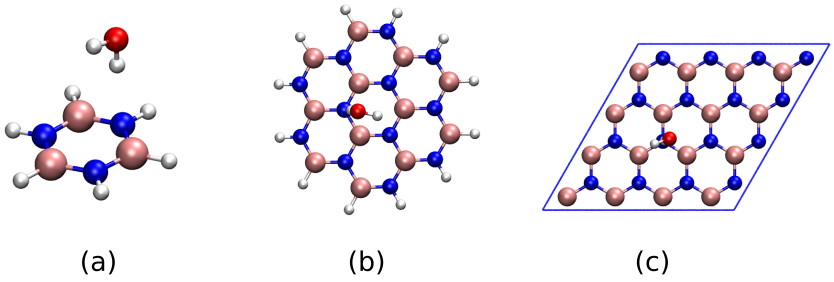

Figure 5.1: (a) Water adsorbed on borazine. (b) Water adsorbed on boronene. (c) Water adsorbed on 4×4 unit cell of h-BN sheet. White spheres are hydrogen, red spheres are oxygen, pink spheres are boron, and blue spheres are nitrogen.

the flat substrate.

5.4 Results

In Section 5.4.1, reference interaction energy curves for water on borazine and boronene at the most favourable adsorption site have been computed, contributing to the body of knowledge that has been reported previously. It will be shown that excellent agreement is achieved amongst the benchmark methods when certain corrections are introduced. The importance of incremental corrections has previously been demonstrated in high accuracy methods for lithium hydride crystals [62, 92]. We also compare a selection of widely used xc functionals and demonstrate the non-transferability of their performance for these very similar systems. After reporting on the molecular systems, in Section 5.4.2 the impact of long-range correlation interaction in the water/h-BN system is determined from RPA, MP2, and MBD at the most favourable adsorption site.

5.4.1 Water adsorption on borazine and boronene

Wu *et al.* have previously computed the interaction energy of water in a two-leg configuration on borazine with DMC and CCSD(T) [70]. In the two-leg configruation both hydrogen atoms of the water molecule point towards the substrate, with one hydrogen atom nearer to a boron atom and the other nearer to a nitrogen atom. Although the configuration that was used is unlikely to be the lowest in energy, they showed that CCSD(T) and DMC predicted the same interaction energy curves, with a maximum interaction of $\sim$ 75 meV at 3.36 Å separation.

Table 5.1: Reference interaction energies using different methods for water with borazine (at 3.32 Å oxygen height above ring) and boronene (at 3.40 Å oxygen height from the molecule).

Method	Water/Borazine	Water/Boronene
DMC (0.015 a.u.)	-111 ± 5	-91 ± 8
DMC(0.005 a.u.)	-117 ± 3	
RPA[a]	-92	
RPA + GW singles[a]	-110	
MP2/CBS	-120	-113
ΔCCSD(T)/CBS	-119	-101[b]
ΔCCSD/CBS	-99	-80[b]

[a] This data was kindly computed by collaborators Benjamin Ramberger and Georg Kresse.
[b] For the water/boronene ΔCCSD(T) result, the difference between MP2 and CCSD(T) using cc-pvdz basis set (without any diffuse functions) was added as a correction to MP2/CBS result. The latter is computed from from aug-cc-pvqz and aug-cc-pvtz basis sets.

Using the one-leg configuration of water, shown in Fig. 5.1, the interaction energy minimum appears at 3.32 Å with DMC. In Table 5.1, reference interaction energies from RPA and MP2 are also reported for the water/borazine system at this 3.32 Å distance oxygen-ring. The ΔCCSD(T) and MP2 with CBS extrapolations agree with the DMC interaction energy within the stochastic error bars that are < 5 meV. It should be noted that without CBS extrapolation, there is a 20 meV overestimation for the MP2 energy with Dunning's aug-cc-pvtz basis set, and it is therefore essential to employ basis set extrapolations. Direct RPA is instead underestimating the water/borazine interaction by $\sim$ 20 meV. Direct RPA has been found to underbind weakly interacting systems in general [110]. This underestimation can be alleviated by including SE and indeed, for water/borazine this leads to an 18 meV improvement, bringing the RPA+SE into agreement with DMC, MP2 and ΔCCSD(T).

Boronene is the BN analogue of coronene, and has been used by Wu *et al.* in an extrapolation scheme to predict the interaction energy of water on h-BN [70]. Similarly in carbonaceous systems, the interaction of water on graphene has been extrapolated from water-acene interactions [145]. Such schemes require a stringent understanding of the various of components of the interaction energy and their scaling. We see here that MP2 is slightly overestimating the DMC interaction energy by $\sim$ 14 meV. Including higher order excitations through ΔCCSD(T) brings the water/boronene interaction energy into agreement with DMC. This has important implications for extrapolation schemes, suggesting that the accuracy of MP2 on a small system may be fortuitous and cannot be guaranteed to extend to larger systems.

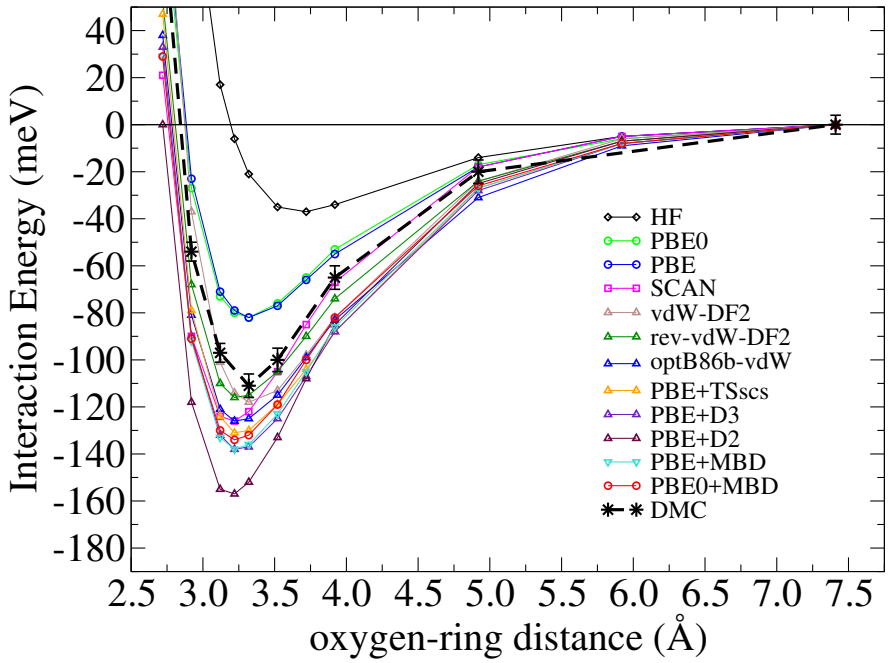

Figure 5.2: Interaction energy curves for water situated above the N site in a borazine molecule. MBD data contributed by Mariana Rossi.

This is also indicated by the ΔCCSD results showing that the contribution from perturbative triple excitations is a considerable 20 meV for both water/borazine and water/boronene. Yet unlike MP2, ΔCCSD underestimates the interaction energy by ~ 10 meV.

Fig. 5.2 shows the interaction energy curve of water with borazine from DMC and with a range of widely used xc functionals in DFT for comparison. The same can be seen in Fig. 5.3 for water on boronene. Amongst the xc functionals that have been considered here, rev-vdW-DF2 and vdW-DF2 provide the best agreement with reference interaction energies near the minimum, predicting interaction energies of -116 meV and -118 meV at 3.32 Å, respectively. Other dispersion inclusive functionals tend to overbind by 10-20 meV. PBE+D2 overestimates the interaction considerably more, by 40 meV. Interestingly, the next best performance is given by the recently developed SCAN functional. SCAN predicts the water/borazine interaction energy to be -126 meV at a distance of 3.22 Å and it agrees perfectly with DMC at water-borazine separations above 3.5 Å. This is somewhat surprising in the absence of any dispersion correction and reflects that accounting for the Ar dimer interaction in the development of this functional has worked well to approximate the long-range behaviour between small molecules.

From Fig. 5.3 it can be immediately seen that the performance of the all xc functionals worsens for water/boronene. DMC and other reference methods predict that the interaction

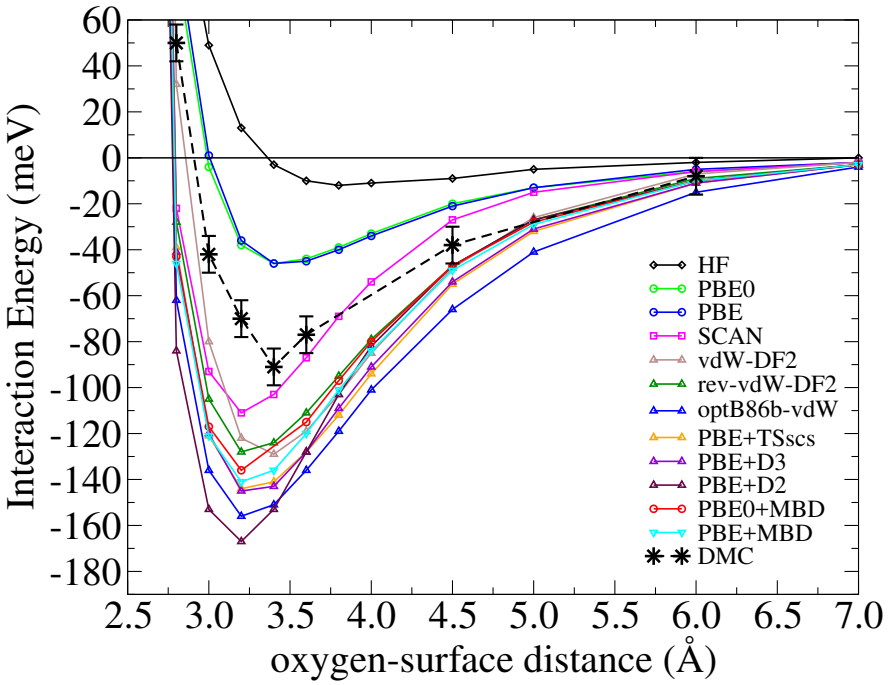

Figure 5.3: Interaction energy curves for water situated above the N site in boronene molecule. MBD data contributed by M. Rossi.

of water weakens with boronene compared to borazine by about 10 meV, to -91 ± 8 meV with DMC. Whereas, the dispersion inclusive functionals estimate a $\sim$ 10 meV stronger interaction for this system and thus overestimate the over interaction energy at the minimum by 30-60%. On the other hand, PBE and PBE0 predict the water/boronene interaction to be approximately half of the water/borazine interaction energy. This is evidently a severe underestimation but it is expected since these xc functionals cannot account for the increase in long-range correlation interaction that arises from the higher numbers of electrons in boronene. Once again, SCAN stands out from other functionals as it predicts a 15 meV weaker interaction for water/boronene compared to water/borazine - in line with the trends given by DMC, MP2 and ΔCCSD(T). However, SCAN appears to overestimate the interaction energy of water/boronene by more than 20 meV despite the absence of any vdW correction. This behaviour of the SCAN functional suggests that it overbinds weakly interacting systems that contain a mixture of hydrogen bonding and dispersion. Thus, the implementation of any vdW-correction to SCAN has to be done cautiously in order to avoid considerable errors.

To briefly summarise the results of this section, DMC, RPA, MP2 and ΔCCSD(T) predict the same interaction energies for water with borazine, when single excitations are included in

the RPA. In addition, reference water adsorption energies on borazine and the larger boronene molecule have shown that xc functionals do not maintain their accuracy across these relatively similar systems. The challenge arises in the larger system for which the inclusion of vdW interactions leads to an overestimation of the interaction energy.

5.4.2 Water on h-BN surface and the impact from long-range correlation

In this section, interaction energy curves are shown for water/h-BN from DMC, RPA, RPA+SOSEX (second-order screened exchange), MP2, and DFT+MBD (see Fig. 5.4). Note that MP2 calculations are performed for the periodic system, with the same unit cell as for the other methods. RPA, RPA+SOSEX, and MP2 energies have been extrapolated to the complete basis set limit using pseudized aug-cc-pV(D,T)Z basis sets. For comparison, PBE, PBE0, vdW-DF2 and SCAN interaction energy curves are also shown. Before addressing the new insights, let us briefly recall previous work for water adsorption on h-BN from reference methods. Al-Hamdani *et al.* computed the interaction energy curve for water at a boron and nitrogen site in h-BN from DMC and benchmarked a selection of xc functionals [65]. Wu *et al.* used non-periodic MP2 to extrapolate from water/molecule interactions to the water/h-BN interaction for the two-leg orientation of water, and obtained the same energy as their extrapolated DMC result within ~ 10 meV error [70]. Later, Wu *et al.* performed direct RPA calculations and estimated a 16 ± 8 meV finite size correction using the two-leg configuration of water [71]. The finite size correction arises because of the long-range correlation that is exhibited by this system. Here, we quantify the impact from long-range correlation with MP2, RPA and the MBD method in DFT but first, we show the effect of SE and SOSEX on RPA interaction energies.

It can be seen from Fig. 5.4 that RPA interaction energies agree within the stochastic error of DMC interaction energies - in line with the findings of Wu *et al.*[71] The interaction energy of water according to RPA is -68 meV at 3.25 Å. Earlier however, SE were found to contribute 18 meV towards the interaction energy of water/borazine and similarly here, SE contribute 20 meV to the interaction energy of water on h-BN when it is 3.25 Å above the surface. From Fig. 5.4 the SOSEX correction to direct RPA increases the interaction energy on the order of ~ 5 meV, especially when water is close to the h-BN surface at $<$3.5 Å height. Therefore, the RPA+SE+SOSEX interaction energy of water on h-BN at 3.25 Å is -94 meV.

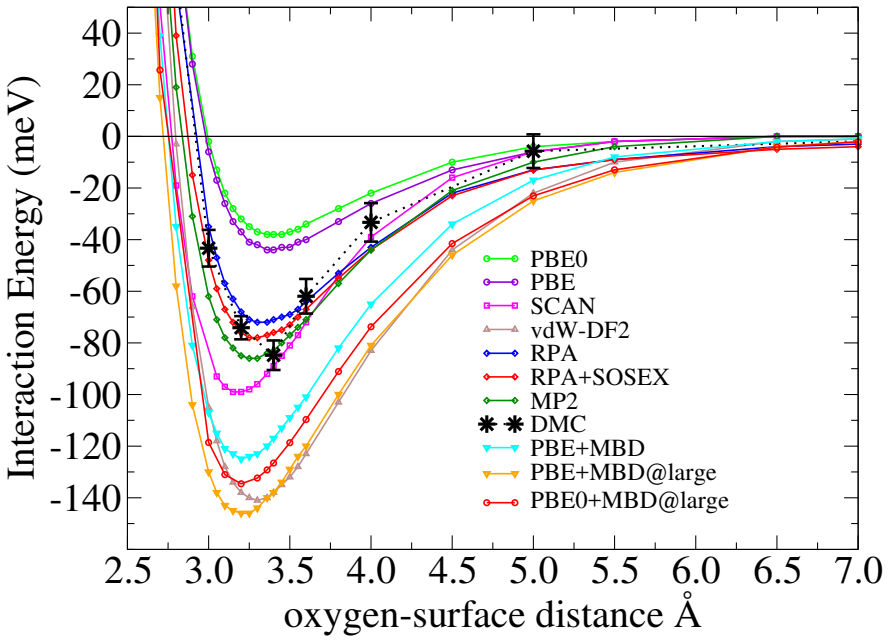

Figure 5.4: Interaction energy curves for water situated above the N site in h-BN. RPA and MP2 data contributed by Theodoros Tsatsoulis and Andreas Grüneis. MBD data from Mariana Rossi.

This seems to be slightly more than the DMC interaction energy curve indicates but there is no DMC data at this distance for water on h-BN to properly verify it. Meanwhile, the interaction energy minimum is −88 meV, also at 3.25 Å, from MP2. It should be noted that MP2 theory does not contain SE by definition.

Interestingly, MP2, RPA and RPA+SOSEX predict the same asymptotic behaviour when the water molecule is more than 4.0 Å above the surface and therefore the same long range behaviour for the (4×4) unit cell of h-BN. Long-range Coulomb type interactions, or otherwise referred to as long-range correlation energy, can extend to the nanometre scale. Capturing these interactions requires very large unit cells and to this end, the MP2, RPA, RPA+SE and PBE+MBD interaction energies for water/h-BN have been computed in increasing supercell sizes. The results are reported in Table 5.2 and shown in Fig. 5.5. An important trait emerges: MP2 adsorption energies converge as $\sim 1/N^2$ whereas adsorption energies from RPA, RPA+SE and the MBD correction converge as $\sim 1/N^{3/2}$, with N being the number of atoms in the h-BN unit cell. $1/N^2$ is the analytically expected behaviour for pairwise vdW dominated contributions but given that the RPA accounts for more correlation than MP2, its deviation from the $1/N^2$ behaviour indicates that adsorption on this 2-dimensional surface is greatly influenced by higher-order correlation interactions. Indeed, MP2 predicts 10 meV

Table 5.2: Interaction energies in meV for water on h-BN at 3.25 Å with increasing supercell sizes. N is the number of atoms in the h-BN substrate unit cell. ΔE_{int}^{lrc} is the difference in the interaction energy due to long-range correlation (lrc) for water with 32 and 98 atoms in the h-BN unit cell. Contributions are indicated in the headers.

N	MP2[a]	RPA[b]	RPA+SE[b]	MBD[c]
18 (3×3)	-70	-34	-58	-88
32 (4×4)	-103	-64	-84	-125
50 (5×5)	-109	-76	-95	-139
72 (6×6)	-113	-78	-97	-145
98 (7×7)	-113	-84	-103	-148
ΔE_{int}^{lrc}	-10	-20	-19	-23

[a] Data from Theodoros Tsatsoulis and Andreas Grüneis
[b] Data from Benjamin Ramberger and Georg Kresse
[c] Data from Mariana Rossi

for the contribution from long-range correlation in contrast to the RPA and MBD correction that estimate ~ 20 meV (see Table 5.2). The absence of higher order excitations in MP2 thus limit its ability to predict long-range behaviour in low dimensional systems.

The ~ 20 meV contribution to the water/h-BN adsorption energy from long-range correlation interactions can be used to improve the DMC adsorption energies that have been reported until now for a (4×4) unit cell of h-BN. Thus, the best estimate of the water/h-BN adsorption energy is -105 ± 6 meV. Importantly, the results signify that the MBD method can be used to estimate the finite size effect arising from long-range correlation interactions that are not captured by a given unit cell size in DMC calculations.

Lastly, let us consider the xc functionals for water/h-BN briefly. The MBD correction has been evaluated for different supercells in Table 5.2 and in combination with PBE0 in Fig. 5.4. In this way the periodic dipole potential is summed over a long distance and all possible collective charge density fluctuations are converged. Indeed, PBE+MBD captures the same long-range behaviour as the RPA. To make a direct comparison with the reference interaction energy curves in the (4×4) unit cell of h-BN, the MBD correction was evaluated at the Γ-point also. This leads to a $\sim$25 meV weakening in the interaction energy at 3.2 Å (see light blue line in Fig. 5.4). Nevertheless, the MBD correction with PBE and PBE0 leads to significant overestimation of the interaction energy (by 50%) compared to explicitly correlated methods. In addition, the interaction energy curve predicted by SCAN is included in Fig. 5.4. Our results suggest that the same level of inaccuracy is exhibited by xc functionals for water/h-BN as for water/boronene. For a detailed analysis of the performance of a range of other widely

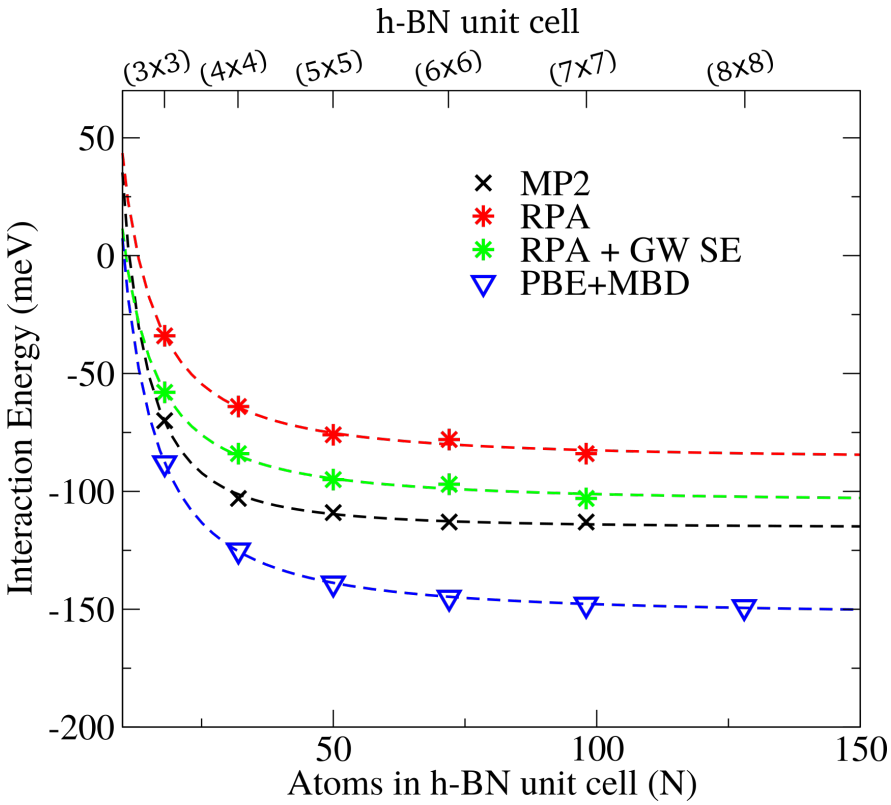

Figure 5.5: Interaction energy of water/h-BN at 3.25 Å height for different supercells with N being the number of atoms in the h-BN unit cell. Dotted lines indicate $1/N^{3/2}$ fits to RPA, RPA+SE, and PBE+MBD interaction energies, and $1/N^2$ for MP2.

used xc functionals on this system, we refer the interested reader to Ref. 65.

5.5 Discussion

Good agreement between RPA based methods, MP2, and DMC has been demonstrated for water adsorption on molecular and extended BN substrates; and some corresponding approximations have been quantified. Interestingly, PBE+MBD has been found to overestimate the interaction energies despite reproducing the correct long-range behaviour for water adsorption on h-BN. To gain further insight into the performance of PBE+MBD, two aspects of this xc functional are considered here: (i) the delocalisation error that is inherent in such functionals, and (ii) the correlation energy of MBD compared with RPA.

First, PBE and PBE+MBD interaction energies have been evaluated using the HF charge densities for the water/boronene system. In HF theory there is no delocalisation (or self-interaction) error, and as a result the HF charge density tends to be more confined. A $16-19$

meV weakening in the PBE and PBE+MBD interaction energies is found by using HF charge densities non self-consistently. This brings the PBE+MBD interaction energy closer to the reference interaction energy, but still overestimating it by $\sim$ 20 meV. In relation to this, we note that the difference between PBE and PBE0 (with or without the MBD correction) for the molecular systems is negligible, as can be seen from Figs. 5.2 and 5.3; and renders the use of PBE0 (containing 25% exact exchange) somewhat ineffective. However, for water/h-BN the improvement from using PBE0 over PBE reaches about 10 meV in Fig. 5.4.

Second, the total correlation energy might be overestimated by PBE+MBD which uses PBE correlation in the short-range and MBD in the long range. As the MBD correction is derived from RPA correlation for quantum harmonic oscillators, it should produce the same amount of correlation energy as RPA when there is no contamination from the short-range correlation energy given by PBE. As a test, we compare the amount of correlation energy from RPA and PBE+MBD contributing to the interaction energy for water at 5.0 Å separation from the h-BN surface. At this height, there should be negligible short-range correlation energy from PBE; and indeed we find that energies agree within 3 meV. The RPA interaction energy is -14 meV and similarly, PBE+MBD interaction energy is -11 meV. Thus, the MBD correction appears to be excellent in the long-range and but at short-range, the interface with PBE appears to be problematic.

5.6 Conclusion

The adsorption energy of water on BN substrates has been determined from DMC, and MP2 and the RPA methods by our collaborators, along with coupled cluster theory for the molecular substrates. Various corrections have been quantified and the most significant include: single excitations to the RPA, perturbative triple excitations in CCSD(T), and the contribution from long range correlation energy on h-BN surface. Each was found to contribute $\sim$20 meV to the adsorption energy of water. Moreover, the RPA type methods and the MBD correction from DFT have shown that water adsorption energy on h-BN scales as $\sim 1/N^{3/2}$ but MP2 predicts $1/N^2$ scaling instead. The findings show that the MBD correction is a promising method for estimating the long-range correlation contribution even for unusual, low-dimensional structures. This is particularly useful for more expensive periodic DMC

calculations, in which some of the inherent finite size effects can be estimated by the MBD method in future.

Chapter 6

Physisorption inside/outside a carbon nanotube

6.1 Abstract

The interaction of H_2 and water with carbon nanomaterials is relevant to H_2 storage, water treatment, and water flow. However, reference interaction energies for H_2 and water on carbon nanotubes remain scarce despite the importance of having reliable benchmark data to accurately inform experimentalists, and to validate and develop computational models. Benchmark fixed-node diffusion Monte Carlo (DMC) interaction energies are provided in this chapter for both H_2 and water monomers, inside and outside a typical zigzag carbon nanotube. A selection of exchange-correlation (xc) functionals and force field potentials are compared. Contrasting predictions are made by two different types of van der Waals functionals. One class slightly overestimates interaction energies by $\sim 20\%$, whilst the other severely overestimates the interaction of molecules inside the CNT by $\sim 200\%$. The discrepancy between these two types of functionals is rationalised using the confinement of water from different nanotube diameters. We make suggestions for the most appropriate xc functionals and classical potential for these systems.

6.2 Introduction

Carbon nanotubes (CNTs) have been found to facilitate ultra-fast diffusion [230–236], desalination [237, 238], and water treatment [239], and were also considered as viable materials for storing H_2 [240, 241]. Spurred on by such promising applications and open questions, experiments and computer simulations of relevant properties such as water flow, adsorption, and contact angles, on graphene and across CNTs have proliferated, see *e.g.* Refs. 238, 242–245.

Yet many obstacles exist in studying these carbon nanomaterials which in some part has lead to counter intuitive conclusions. For instance, Hummer *et al.* showed that small changes in water-carbon interaction energies can lead to a significant change in the water occupancy inside the hydrophobic carbon channels of nanotubes [246]. Another example is the debate that surrounded the transparency of graphene for the contact angle of water [141, 143, 144, 206, 247–250]. This is partly because of the inherent challenges of studying a clean graphene surface experimentally and having reliable and accurate models in simulations.

Indeed, the majority of studies focusing on either H_2 or water on these carbon nanomaterials use classical force fields with Lennard-Jones (LJ) type potentials to model the intermolecular interactions. However, different methods, either classical or ab initio, predict different adsoprtion energies and it is not clear which methods give more accurate results. In addition, only tentative comparisons can be made from the literature since different types of CNTs and adsorbate configurations have been reported on.

Accurate reference data is therefore paramount for the verification of predicted adsorption energies and for the appropriate parametrization of force field potentials. Due to the scarcity of reference information a number of force field studies have relied on experimental adsorption energies of H_2 [251] and the contact angle of water on graphite [252] - a material which is physically different to either graphene or CNTs. Moreover, Leroy *et al.* show that the work of solid-liquid adhesion is a better reference than water contact angles [253], and thus the ability to reproduce the correct adsorption energy between water and the substrate is more desirable in a force field. As noted earlier, the most promising and commonly used methods for computing benchmark adsorption energies include but are not limited to: coupled cluster with single, double, and perturbative triple excitations (CCSD(T)), the random phase approximation (RPA), and diffusion Monte Carlo (DMC). These methods are explicitly

correlated and account for exact exchange, thus they are able to capture weak interactions that contain significant proportion of van der Waals (vdW) forces.

Recent progress has been made by Lei *et al.* using density fitted local CCSD(T) (DF-LCCSD(T)) to compute interaction energy curves for a water monomer with non-periodic, H-capped, segments of CNTs of varying curvature [68]. Force field parameters have also been proposed based on the results. Meanwhile, it has been noted that long-range charge density fluctuations on the nanometre scale play a key role in the interactions of low-dimensional systems like graphene and CNTs [46, 104] and it is therefore important to go beyond localised segments of such systems.

The goal here is to take another step towards adsorption on the real physical CNT by providing benchmark information from fixed-node DMC which takes into account the extended nature of the CNT. We have computed the physisorption energy of both H_2 and water, inside and outside a CNT using DMC. Direct comparison is made with some new and some widely used exchange-correlation (*xc*) functionals and force field potentials. We also compare the interaction energies with a graphene substrate and draw similarities with adsorption on the exterior of the CNT. We find that a particular class of van der Waals *xc* functionals overestimates the interaction energy inside the CNT by up to a factor of 2.

This chapter is organised as follows: the methods are outlined first, followed by results for interaction energies of water and H_2 on graphene and CNT from DMC, *xc* functionals, and force field potentials. Implications of the results are discussed in Section 5.5 and we close in Section 5.6 with some conclusions.

6.3 Methods

VASP 5.4.1 [177–180] was used for the density functional theory (DFT) calculations with projector augmented wave (PAW) potentials [181, 182]. There are countless *xc* functionals available in DFT and it would not be feasible to test all of them, hence only a few widely used or relatively new *xc* functionals have been chosen as part of this study. The various *xc* functionals tested include LDA [172], PBE [173], dispersion corrected PBE (D2 [189], D3 [34, 35], TSscs [38, 39], and MBD [40, 218]) and vdW-inclusive functionals (original vdW-DF [32, 254], optPBE-vdW [37], optB88-vdW [37, 255], optB86b-vdW [36, 214], vdW-DF2 [33],

rev-vdW-DF2). We have also tested the more recently developed strongly constrained and appropriately normalised (SCAN) functional of Sun *et al.* [220]. This functional is expected to outperform PBE for weakly interacting systems because it contains some non-local correlation from constraints based on the non-bonded interaction of an Ar dimer. Furthermore, the revised version of the Vydrov and Van Voorhis non-local correlation functional, rVV10 [41, 42], was included using Quantum Espresso. Hybrid functionals that contain a fraction of exact exchange have not been employed here: these are much more computationally expensive and it is expected that the description of correlation energy has a much larger impact on the physisorption in these systems than exchange energy.

From an electronic perspective, there are two types of CNTs: armchair which is metallic and zigzag which is semiconducting. The modelled CNT is (10,0) in configuration and belongs to the class of non-metallic zigzag CNTs. A CNT unit cell containing 80 carbon atoms was relaxed using an increased 600 eV energy cut-off as prescribed in VASP and PBE, PBE+TSscs, and vdW-DF2 functionals; the resulting cell parameters differ by 0.7% at most. PBE+TSscs predicted the nearest C-C bond length to the experimental C-C bond length in graphite (1.421 Å) and hence, the 8.58 Å unit cell length predicted by this functional along the CNT axis was chosen for all further calculations. 25 Å was used along the other axes which allows for at least $\sim$ 17 Å separation between periodic images of the CNT. The interaction energy of water/CNT was tested against a larger CNT unit cell of 12.8 Å length at the DFT level. The difference in interaction energies was less than 3 meV indicating that the water is well separated from its image. Water interaction energies were tested up to $10 \times 1 \times 1$ **k**-points and convergence was reached already with just the Γ-point (within 2 meV) and subsequently used.

Graphene is a semi-metal for which a (5×5) unit cell was used with a 15 Å long vacuum between graphene sheets. Following a convergence test on the number of **k**-points, a $4 \times 4 \times 1$ **k**-point mesh was chosen. After careful convergence tests for water/CNT and water/graphene interaction energies, a plane-wave energy cut-off of 500 eV was applied for both systems. Hard PAWs with 700 eV cut-off energy were also used to check convergence and standard PAWs were converged to less than 0.2 meV for the interaction energy of water on graphene.

The lowest energy geometries of water interacting with CNTs are not entirely consistent in previous studies which have mainly employed LDA and PBE [256–258]. Here, vdW-DF2

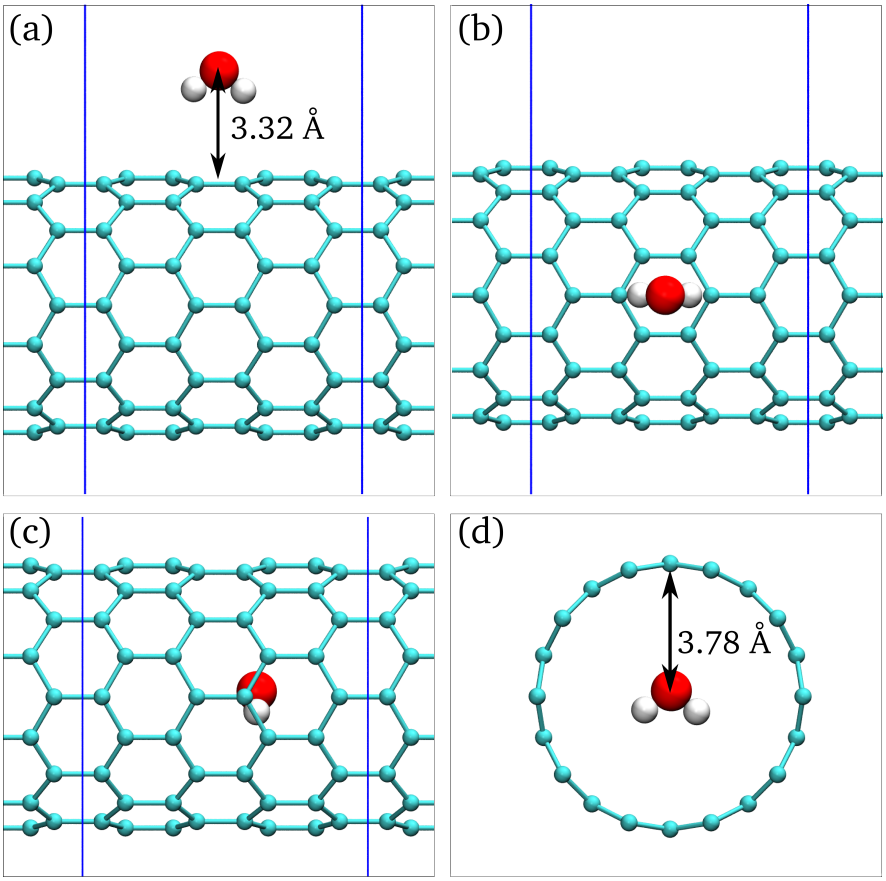

Figure 6.1: Unit cell of water outside (top panel) and inside (bottom panel) a CNT(10,0). The unit cell is bounded by blue lines and contains 80 carbon atoms with a CNT diameter of 7.9 Å. Configurations have been obtained from DFT geometry relaxations with the vdW-DF2 functional.

and PBE+TSscs were used to relax several starting configurations of water and H_2, inside and outside the CNT, and on different sites above graphene. The lowest energy orientations were found to be consistent between PBE+TSscs and vdW-DF2 indicating that the choice of *xc* functional does not have a great impact on the adsorbate geometry and vdW-DF2 relaxed structures were chosen for subsequent DFT, force field and DMC calculations (see Fig. 6.1 and Fig. 6.2). In general, the potential energy surface is fairly smooth for graphene and even more so for the CNT, and as such, we expect small variations in the interaction energies for different configurations with other methods.

Force field calculations were performed using LAMMPS [259] with the TIP5P [260] and SPC/E [261] models of water and LCBOP [262] for the carbon substrates. The often used Werder potential [252] for carbon-water interaction was tested along with recent carbon-water LJ type potentials that were fit to coupled cluster data for water on graphene [263] and water

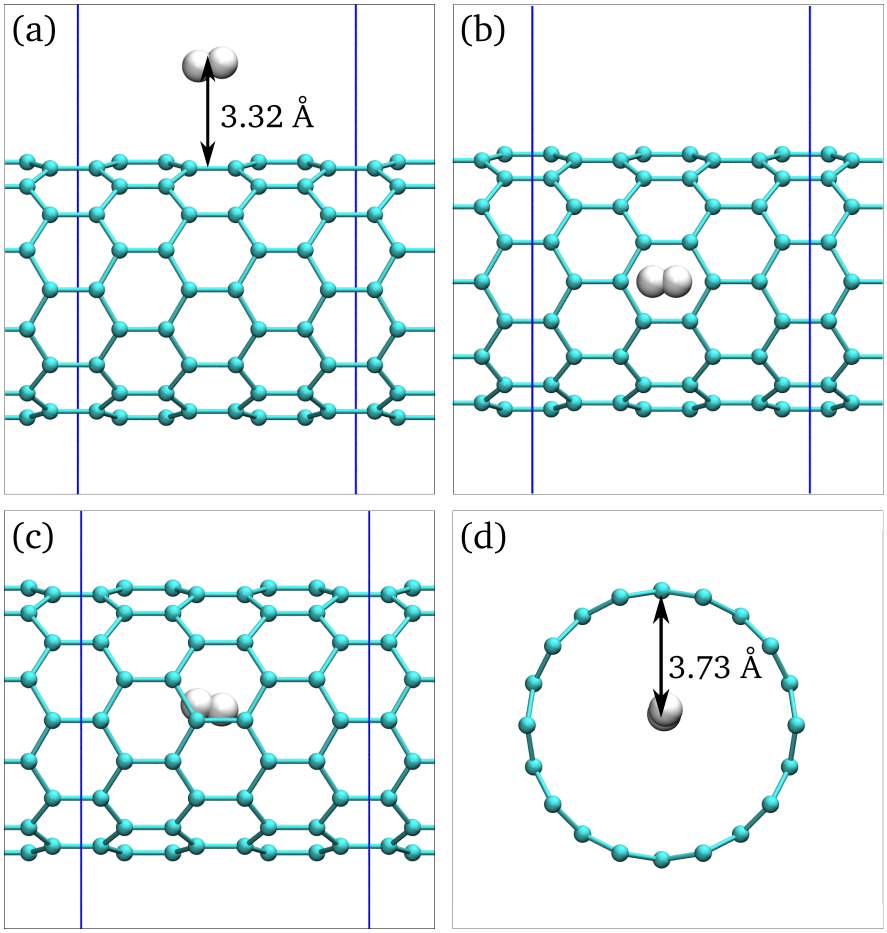

Figure 6.2: Unit cell of H_2 outside (top panel) and inside (bottom panel) a CNT(10,0). The unit cell is bounded by blue lines and contains 80 carbon atoms with a CNT diameter of 7.9 Å. Configurations have been obtained from DFT geometry relaxations with the vdW-DF2 functional.

on a H-capped segment of CNT [68].

DMC calculations for CNT systems were performed using the CASINO code [175], with the same cells and configurations as for the DFT calculations. A plane-wave energy cut-off of 500 Ry was applied to the LDA calculation of the trial wavefunctions in Quantum Espresso [169] using the Trail and Needs pseudopotentials [170, 171] for all atoms. The resulting wavefunctions were expanded in terms of B-splines [174] using a grid multiplicity of 1.0. A Jastrow factor with up to three-body contributions was used to account for correlation and optimised using variational Monte Carlo. 1-D periodicity was applied along the CNT axis. A time-step of 0.015 a.u. was used in DMC whilst employing the locality approximation [176] and 80,000 walkers for each configuration. The DMC calculations were run until a stochastic error of 10-15 meV was reached, producing a combined error of less than 20 meV in each interaction energy. A new implementation of CASINO has been used for H_2 on graphene, which allows a larger time-step (0.05 a.u.) to be used. Since H_2 is small, a 3×3 unit cell of graphene was found to be large enough to avoid any interaction between the periodic images of H_2 molecules. In addition, **k**-point convergence was reached with 2 **k**-points at the DFT level. Trial wavefunctions were produced at each **k**-point using Quantum Espresso, as prescribed for the CNT systems. The resulting DMC energies at each **k**-point were averaged to give a final interaction energy for H_2 on graphene.

The interaction energy of either water or H_2 on the carbon substrates is defined as,

$$E_{int} = E_{ads}^{tot} - E_{far}^{tot} \tag{6.1}$$

where E_{ads}^{tot} is the total energy of the molecule/substrate system in the interacting configurations shown in Fig. 6.1 and Fig. 6.2 for water and H_2, respectively. E_{far}^{tot} is the total energy of the molecule/substrate system with the components separated by 12 Å.

6.4 Results

The interaction energy of water and H_2 has been computed with DMC, a selection of *xc* functionals, and a few different classical water-substrate potential models. Table 6.1 reports the interaction energies for water on graphene and the CNT from DMC and DFT (see Table 6.2 for H_2 adsorption). The reference DMC results are discussed first, followed by the performance

of the *xc* functionals for which some striking results lead to further questions and analysis. Finally some comments on the force field results are presented.

Water physisorbs on the exterior of the CNT with an interaction energy of $-80(\pm19)$ meV and on the interior with an interaction energy of $-244(\pm17)$ meV. The DF-LCCSD(T) water adsorption energies computed by Lei *et al.* for a H-capped CNT segment with similar diameter [68] are within ∼20 meV of the DMC reference energies reported here. The DMC interaction energy of water with graphene has previously been calculated to be $-70(\pm10)$ meV [63]. H_2 physisorbs more weakly: $-13(\pm19)$ meV on the exterior of CNT, which means it could be repulsive within stochastic error, and $-99(\pm19)$ meV on the interior. The interaction energy of H_2 on graphene from DMC is $-24(\pm11)$ meV. The H_2/CNT interaction is ∼50% weaker than water on each substrate; likely because of the stronger electrostatic interaction between the substrate and the permanent dipole of water.

Note that the interaction energies of water on graphene and the exterior of the CNT are very close in energy (within stochastic error). Similarly, the DMC interaction energy for H_2 on the exterior of the CNT and on graphene is small. The similar interaction energies on graphene and outside the CNT suggest that the curvature of this relatively small (10,0) nanotube has at most a modest impact on adsorption on the exterior of the CNT. Experimentally produced CNTs can have much larger diameters than CNT(10,0) [230], so it is likely that interaction energies on those surfaces will be close to graphene.

In contrast, the DMC interaction energies inside the nanotube are three times larger than those obtained outside the nanotube. This relative difference between the interaction outside and inside of the nanotube will have a large impact on molecules entering a nanotube [246]. As such, it will be another important aspect to consider when assessing the accuracy of various methods in the following sections, starting with *xc* functionals.

6.4.1 Performance of *xc* functionals: Challenge of internal interaction

With the reference DMC information we can assess the performance of a selection of *xc* functionals listed in Tables 6.1 and 6.2, beginning with the most commonly used functionals, LDA and PBE. LDA only accounts for short-range correlation and yet it provides the most accurate prediction for water and H_2 adsorption inside the CNT, -237 and -96 meV, respectively. This fortuitous performance of LDA is not consistent, and even when considering similar 2-

Table 6.1: Interaction energies (in meV/H_2O) of water on graphene, outside the CNT, and inside the CNT.

Method	graphene	external-CNT	internal-CNT
LDA	−124	−122	**-237**
PBE	−21	−26	−84
SCAN	**-84**	**-78**	−203
PBE+D2	−136	−120	−305
PBE+D3	−126	−113	−293
PBE+TSscs	−158	−137	−327
PBE+MBD	−130	**-99**	−293
SCAN+D3	−123	−117	−292
vdW-DF	−130	−109	−458
optB88-vdW	−152	−123	−457
optPBE-vdW	−169	−137	−506
optB86b-vdW	−154	−122	−459
vdW-DF2	−129	−108	−397
rev-vdW-DF2	−119	**-97**	−365
rVV10	−144	−124	−382
Werder *et al.*		−59	−180
Lei *et al.*		−122	−362
PHS		**-70**	**-251**
DMC	**-70±10**[*]	**-80±19**	**-244±17**

[*] DMC interaction energy of water/graphene calculated in a previous study by Ma *et al.* [63]

Table 6.2: Interaction energies of H_2 on graphene, outside of CNT, and inside of CNT in meV.

	graphene	external-CNT	internal-CNT
LDA	−67	−60	**-96**
PBE	−5	**-6**	−22
SCAN	**-22**	**-17**	−50
PBE+D2	−59	−48	**-117**
PBE+D3	−53	−52	−128
PBE+TSscs	−72	−60	−138
PBE+MBD	−53	−39	**-107**
SCAN+D3	−43	−38	**-100**
vdW-DF	−77	−59	−230
optB88b-vdW	−75	−59	−216
optPBE-vdW	−94	−74	−253
optB86b-vdW	−79	−58	−221
vdW-DF2	−69	−55	−181
rev-vdW-DF2	−58	−44	−165
rVV10	−65	−52	−151
DMC	-24 ± 11	-13 ± 19	-99 ± 19

dimensional systems like water on hexagonal boron nitride [65], LDA strongly overestimates the interaction energy and the minimum distance to the surface. We can see from Fig. 6.3 that PBE severely underestimates the interaction energy of water on these low dimensional carbon substrates wherein dispersion is a significant part of the interaction. For H_2 adsorption PBE still underestimates the interaction energy of the interior configuration but appears to provide a reasonable interaction energy for H_2 outside of the CNT (see Fig. 6.4). The majority of previous DFT studies on graphene and CNTs have used PBE and LDA to study water and H_2 [256, 258, 264–268]. The reported water-substrate and H_2-substrate distances vary by up to 0.2 Å in the literature and involve CNTs with different diameters and lengths. Even with these differences in mind, the interaction energies in previous studies are within 30 meV of those reported here for LDA and PBE.

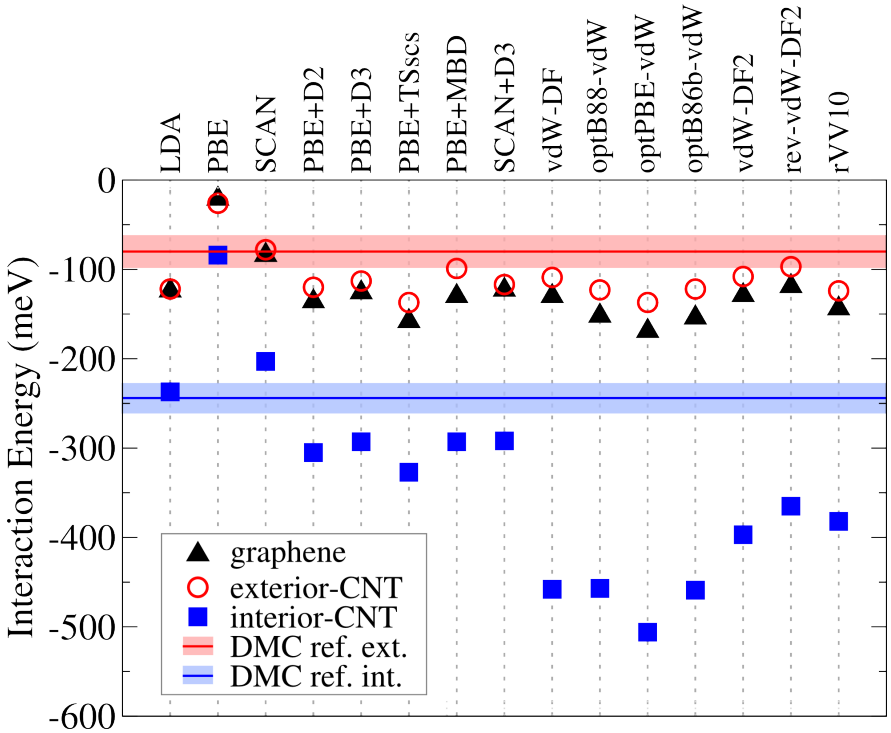

Figure 6.3: Interaction energies of water inside (blue squares) and outside (red circles) the CNT with different *xc* functionals and DMC. The DMC reference interaction energies are indicated by horizontal solid lines with the shaded area corresponding to the stochastic error. The interaction energy of water on graphene with different *xc* functionals is also shown using black triangles. All energies are in meV.

More promising performance is seen for the recently developed SCAN functional which predicts excellent physisorption energies for water (−84 meV) and H_2 (−17 meV) outside of the CNT. SCAN also predicts a similar physisorption energy of water on graphene to

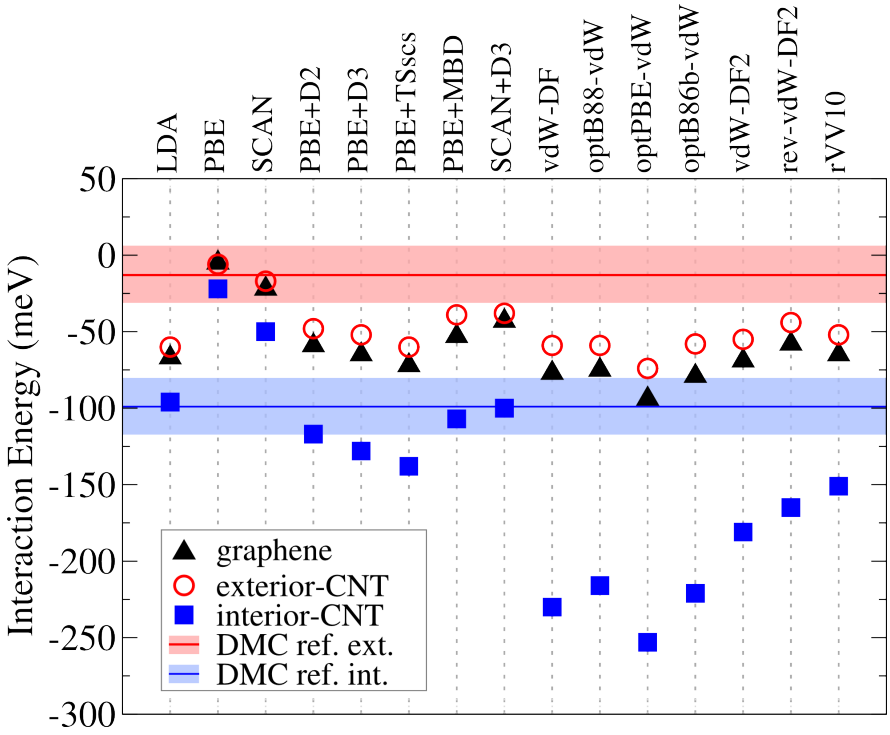

Figure 6.4: Interaction energies of H_2 inside (blue squares) and outside (red circles) the CNT with different *xc* functionals and DMC. The DMC reference interaction energies are indicated by horizontal solid lines with the shaded area corresponding to the stochastic error. The interaction energy of H_2 on graphene with different *xc* functionals is also shown using black triangles. All energies are in meV.

DMC (and RPA) from Ma *et al.* [63]. However SCAN slightly underestimates the interaction energies for both molecules inside the CNT due to the absence of longer-range correlation in the functional that is needed to capture all of the dispersion interaction.

As noted in Chapter 2.3.1, there are two particularly common ways to account for dispersion interactions in DFT *xc* functionals. The first is by adding a dispersion correction calculated from atomic polarizabilities and includes the D2, D3, TSscs and MBD methods. The second is based on the original vdW-DF from Dion *et al.* [32] in which two-body dispersion is calculated based on charge densities and is seamlessly incorporated in an *xc* functional. Some have been shown to perform very well for weakly bound molecular systems (we refer the reader to the reviews in Refs. 43, 45–47); though not as well for water adsorption on graphene [63] and hexagonal boron nitride [65]. For water/CNT and H_2/CNT, PBE+MBD and SCAN+D3 predict the best interaction energies amongst the vdW functionals tested here for both exterior and interior adsorption. MBD takes into account beyond two-body correlation interactions and is therefore able to capture more effectively the dispersion that is present

in the DMC reference interaction energies. The D3 correction includes up to three-body correlation interactions and as we can see from Fig. 6.3 and Fig. 6.4 it also performs well. Their performance is followed closely by the other dispersion corrected PBE functionals.

For exterior adsorption of water and H_2 on the CNT, the vdW-DFs perform similarly to dispersion corrections, over-binding by 20 to 40 meV compared to DMC. The exceptions are vdW-DF2 and rev-vdW-DF2 which predict water interaction energies of -108 and -97 meV, respectively. Rather strikingly, vdW-DFs predict significantly more pronounced interaction energies inside the CNT, with up to 250 meV overestimation by optPBE-vdW. That is twice the DMC physisorption energy for water inside CNT. In fact we see two regimes emerge for vdW functionals based on internal interaction energies from Fig. 6.3 and Fig. 6.4. Such a stark difference in the behaviour of dispersion corrected DFT *xc* functionals and vdW-DFs is not often seen in other systems and raises several questions which we address in Section 5.5.

The comparison of external to internal interaction energy is another important aspect, especially to H_2 storage studies and in general for understanding how these molecules adsorb on CNTs. We provide reference information for water and H_2 inside and outside CNT(10,0), showing that interaction is a factor of three times stronger inside. Some of the *xc* functionals predict a similar ratio namely, PBE (3.2), PBE+D2 (2.6), PBE+D3 (2.6), PBE+MBD (3.0) and SCAN (2.6). The remaining *xc* functionals not only overestimate interaction energies but also get this ratio wrong. LDA predicts a factor of two, whilst some vdW-inclusive functionals predict up to four times larger interaction in the interior of CNT. Thus, this relative proportion of exterior to interior interaction energy remains a challenge for many of the *xc* functionals tested here.

6.4.2 Reliable water-carbon potentials for water/CNT?

Three classical potentials for water-carbon substrate interaction have been tested here, referred to as: Werder *et al.* [252], Lei *et al.* [68], and PHS (Pérez-Hernández and Schmidt) [263]. The potential by Werder *et al.* is one of the most commonly used for water/carbon systems and was designed to reproduce experimental water contact angles on graphite [252]. In this potential only the C-O interaction is defined ($\epsilon_{CO} = 5.848$ meV and $\sigma_{CO} = 3.19$ Å) and was obtained by tuning ϵ_{CO} until the experimental water/graphite contact angle was reproduced with the SPC/E model of water. It can be seen from Table 6.1, that this interaction

potential leads to an underestimation in the interaction energy of water especially inside the CNT by at least 40 meV (20%).

Meanwhile, Lei *et al.* have suggested a few different water-carbon potentials by manually fitting interaction parameters to DF-LCCSD(T) interaction energy curves for water with H-capped segments of CNTs. It is recognised therein that water adsorption inside and outside the nanotube is not accurately predicted by any single set of parameters. We have chosen one that includes C-H interaction parameters ($\epsilon_{\mathrm{CH}} = 3.835$ meV and $\sigma_{\mathrm{CH}} = 2.85$ Å) as well [68] and is therefore more sensitive to the water force field employed. Using TIP5P for the water force field as prescribed, there is a three-fold increase of the water interaction energy from exterior to the interior of CNT, in agreement with DMC reference results. However, the interaction energy is overestimated especially inside the CNT by ∼40%. It is worth noting that the orientation of water in the DF-LCCSD(T) calculations is different to the configuration studied here; with the H atoms of water parallel to the length of the CNT instead of perpendicular as shown in Fig. 6.1.

Another water-carbon potential is based on CCSD(T) water-graphene adsorption energy proposed by Pérez-Hernández and Schmidt [263] and the TIP5P model of water. This model was obtained by reproducing the CCSD(T) interaction energy of water in the up and down configurations on a 58 carbon atom segment of graphene [64]. Orientation dependence is therefore built in by defining C-H as well as C-O interactions for water. From Table 6.1 it can be seen that this potential predicts interaction energies in line with the DMC references for water on CNT.

The sensitivity of the classical potentials to the form of parametrization is clear from the varying performance of three potentials considered here. We hope the DMC reference interaction energies of water and H_2 on CNT will be useful for future force field simulations of these systems.

6.5 Discussion

The benchmark DMC energies reported in this chapter are the first accurate interaction energies for water and H_2 on an extended CNT and are also intended to serve as references for other methods. Additional insight is given on the DMC results in this section and the

significant overestimation by vdW-DFs for adsorption inside the CNT is addressed. We first comment on the appropriateness of the DMC method for these systems in the context of other benchmark methods, and we make an estimate of finite size effects in the DMC energies. Later, the conflicting predictions from vdW-DFs and dispersion corrected functionals are discussed and rationalised using additional information from DFT for larger CNTs.

First, for the CNT(10,0) that is considered here, multi-reference character is unlikely due to the curvature of the nanotube and the finite band gap which is ∼1 eV from GGAs. Therefore, a single-determinant approach as used here is sufficient. An important and challenging feature of CNTs that needs to be accounted for is their extended and delocalised nature. To this end, DMC and RPA can be efficiently used with periodic boundary conditions and as a result, they are free of localisation approximations in the charge density and polarizability. On the contrary, such approximations are inherent in non-periodic calculations using CCSD(T). Using unit cells with periodic boundary conditions however leads to finite size effects in DMC and RPA.

The main source of finite size effects relevant to the CNT studied here with DMC is the long-range nature of Coulomb interactions. Such long-range Coulomb interactions can extend to the nanometre scale [104] and are prevalent in low-dimensional extended materials with small band gaps [104, 269]. As such, considerably large unit cells are required to capture these interactions. Whilst DMC provides a many-body solution, it remains an expensive method for which large unit cells become increasingly prohibitive. Whereas, the MBD correction is more computationally feasible and can be used with more **k**-points to predict the contribution from long-range Coulomb interactions. We find that the MBD correction to PBE is converged with a **k**-point mesh of $2 \times 2 \times 2$. The water interaction energy is found to increase by 12 meV to −111 meV outside the CNT and by 16 meV to −309 meV inside the CNT. For the H_2 interaction the MBD correction is 5-8 meV only. Although these corrections are still smaller than the stochastic errors in the DMC reference values, they should be taken as the finite size error and therefore, the reference energies are shifted towards stronger interaction.

Second, the DFT results in this chapter indicate that molecular adsorption on CNTs is more accurately described by dispersion corrected *xc* functionals as opposed to including vdW interactions in a seamless, though still approximate, manner. This is a somewhat unexpected finding because such a clear-cut difference in interaction energies between these two types of

vdW functionals has not been observed previously. The reader is referred to some notable reviews, for example Refs. 43, 45, 47, wherein various vdW-DFs and dispersion corrected functionals have been benchmarked on a number of weakly interacting systems, including the S22 data set and H_2 adsorption on metal surfaces. In addition, many of the assumptions made in developing these vdW functionals are common to both types, and here we attempt to tease out the source of the disagreement.

For vdW-inclusive functionals the charge density is immediately brought into question since the dispersion contribution is calculated using the densities. To address this possibility, the vdW-DF interaction energy was calculated using the more localised Hartree-Fock density of the water/CNT configurations. The reduction in the interaction energy for the interior configuration of water is a mere 11 meV, going from −458 meV to −447 meV. Hence, any delocalisation error that is present in the vdW-inclusive functionals is not enough to explain the overestimation seen here that is 100-200 meV.

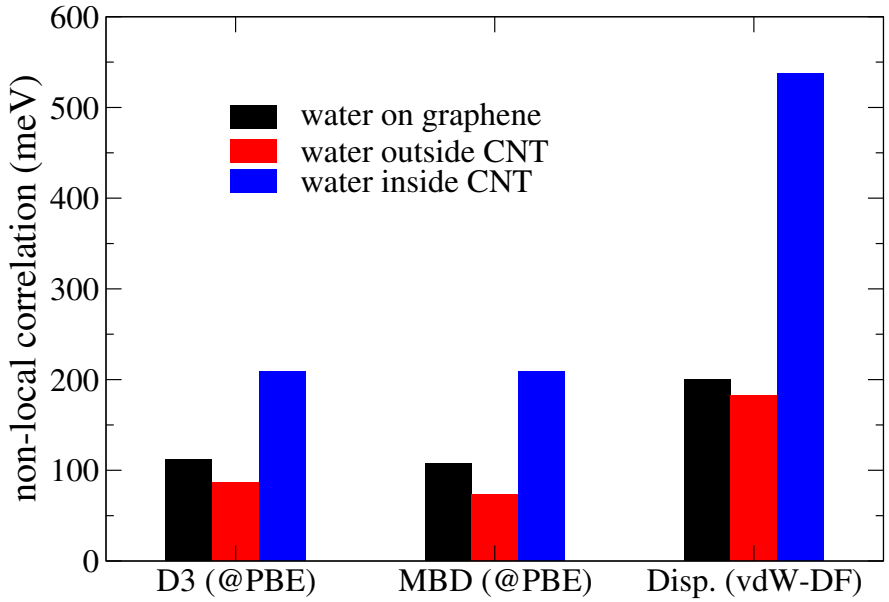

Figure 6.5: Non-local correlation contribution to the interaction energy of water outside (red) and inside (blue) the CNT(10,0) from PBE+D3, PBE+MBD and vdW-DF. Water on graphene is also shown in black and all energies are in meV.

In Fig. 6.5 the dispersion contribution to the interaction energies of water on graphene and the CNT are shown for PBE+D3, PBE+MBD and vdW-DF. Evidently, the non-local correlation in vdW-DF is at least twice as large as the contribution from the dispersion corrections for all the systems. Normally in vdW-DFs the high non-local correlation is deliberately

offset by a more repulsive exchange interaction at short distances. However for water inside the CNT, the repulsive exchange interaction is not high enough to *alleviate* the ∼500 meV of non-local correlation. So why is this non-local correlation interaction so high? To answer this, previous work by Dobson *et al.* [46, 269] and Misquitta *et al.* [270] identify key assumptions in vdW approximations based on $1/r^6$ behaviour including the implicit assumption of locality in polarizability. Methods based on these approximations are unable to account for non-additivity in polarizabilities, which are particularly relevant for extended low-dimensional systems. Furthermore, this effect is expected to be important for medium-range correlation interaction in small band gap systems. This medium-range correlation regime refers to atomic separations larger than bonding distances (a few Ångstroms) and closer than the long-range limit where the interaction reaches the $1/r^6$ limit (∼10 Å). As a result there is no guarantee that either dispersion corrections or vdW-inclusive functionals should predict accurate dispersion interactions for molecules adsorbing in these highly anisotropic systems studied here.

However, we find that dispersion corrected PBE and SCAN both provide much better predictions than vdW-inclusive functionals. One possibility for this is the use of damping functions in these dispersion corrections. The damping function is used to adjust the short-range behaviour of the dispersion correction with respect to the underlying *xc* functional empirically. In doing so, the medium range correlation is affected and by way of fitting, it is possible that some non-additivity has been absorbed into this function. The importance of medium-range correlation can be seen by comparing the relaxed interaction energies for water inside and outside of CNTs with different diameters in Fig. 6.6, and the corresponding radial distribution functions between oxygen and carbon, $g_{OC}(r)$, in Fig. 6.7. From Fig. 6.6, water interaction energies outside the CNT show less than 7% deviation between PBE+D3 and vdW-DF. Whereas for water inside the CNT, the interaction energy difference PBE+D3 and vdW-DF increases rapidly from 9% to 30% as the CNT diameter decreases. For the same systems, Fig. 6.7(a) shows a distinct increase in medium-range oxygen to carbon distances, as the diameter of the CNT is reduced. Note that the same increase is not seen for water outside the CNTs in Fig 6.7(b). This suggests that vdW-DF begins to overestimate the dispersion interactions more than PBE+D3 in the medium-range correlation regime. We expect this to be the case for all the other vdW-DFs tested in this chapter as well as the rVV10 functional.

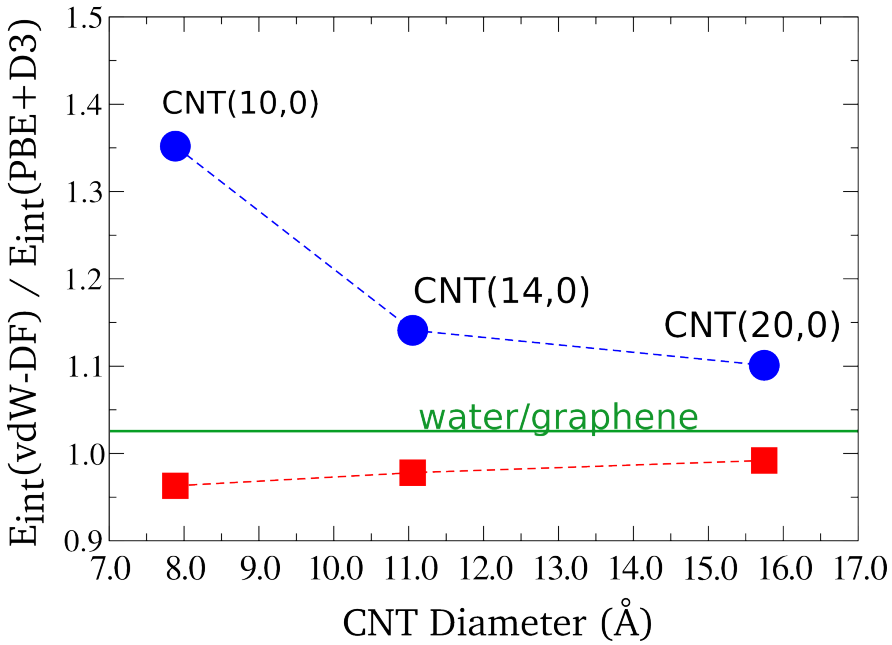

Figure 6.6: Ratio of vdW-DF to PBE+D3 interaction energies for water inside (blue circles) and outside (red squares) of CNTs with increasing diameters: CNT(10,0), CNT(14,0) and CNT(20,0). The water/graphene ratio is indicated by the solid green line.

6.6 Conclusions

DMC reference interaction energies have been computed for water and H_2 on the outside and inside of the zigzag CNT(10,0), and also for H_2 on graphene. Adsorption of either water or H_2 inside this nanotube is about three times larger than outside. Three water-carbon classical potentials were benchmarked against DMC, including the widely used Werder *et al.* potential. Naturally, the results are very sensitive to the parameters and underlying model, but we find that for water on CNT(10,0) the potential given by Pérez-Hernández and Schmidt predicts interaction energies in excellent agreement with DMC.

In contrast, a selection of widely used or new *xc* functionals considered here are unable to accurately predict the interaction energies for these systems, nor the relative strength of adsorption of water or H_2 outside and inside the CNT. Strikingly, there is a clear distinction between dispersion corrected *xc* functionals - which only slightly overestimate the interaction energies - and vdW-inclusive functionals. The latter strongly over-bind molecules inside the CNT: up to twice as much. After eliminating delocalisation error and relaxation effects, it seems that the extended and highly anisotropic nature of these systems causes non-additive dispersion interactions that cannot be accounted for by assuming any form of locality in the

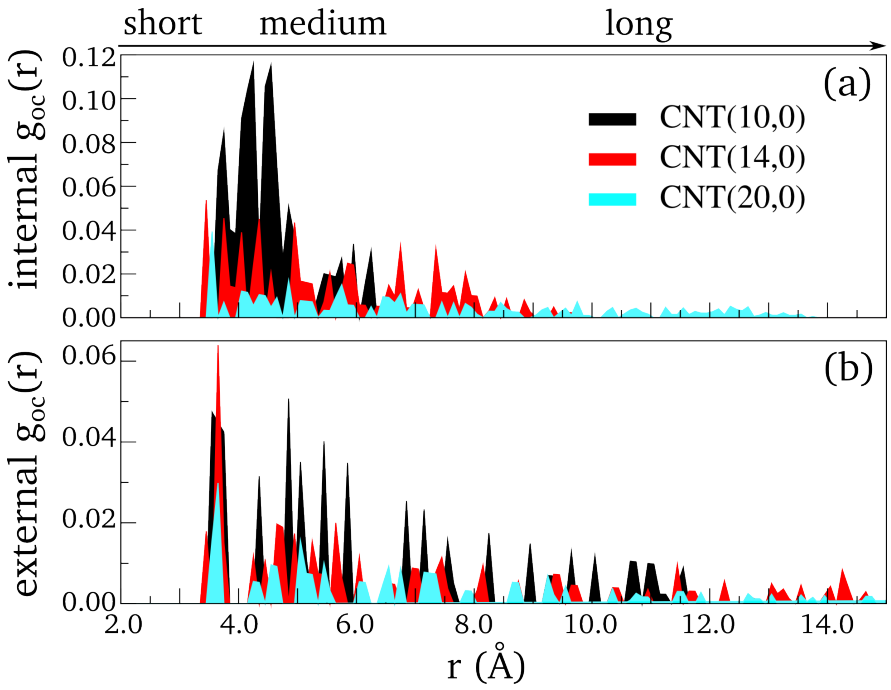

Figure 6.7: Radial distribution function of oxygen and carbon within the unit cells of CNT(10,0), CNT(14,0) and CNT(20,0) in black, red, and blue, respectively: (a) water inside the CNTs and (b) water outside the CNTs.

polarizability. This has been suggested by others previously but clearly demonstrated here for an important physical system. Indeed it is not clear why dispersion corrected functionals perform better but the damping function is likely involved. Benchmark studies of water on other low-dimensional materials suggest they too lack consistent accuracy. As such, further development in vdW-DFs by incorporating anisotropic and non-localised polarizabilities could go a long way in establishing reliable *xc* functionals for so-called vdW materials.

Chapter 7

Tuning dissociation at 2D surfaces

7.1 Abstract

Novel uses for 2-dimensional materials like graphene and hexagonal boron nitride (h-BN) are being frequently discovered especially for membrane and catalysis applications. Still however, a great deal remains to be understood about the interaction of environmentally and industrially relevant molecules such as water with these materials. Taking inspiration from advances in hybridising graphene and h-BN, we explore using density functional theory, the dissociation of water, hydrogen, methane, and methanol on graphene, h-BN, and their isoelectronic doped counterparts: BN doped graphene and C doped h-BN. We find that doped surfaces are considerably more reactive than their pristine counterparts and by comparing the reactivity of several small molecules we develop a general framework for dissociative adsorption. From this a particularly attractive consequence of isoelectronic doping emerges: substrates can be doped to enhance their reactivity specifically towards either polar or non-polar adsorbates. As such, these substrates are potentially viable candidates for selective catalysts and membranes, with the implication that a range of tuneable materials can be designed.

7.2 Introduction

Much of the work on graphene and h-BN is motivated by the sustainability and the availability of the component elements – an aspect which can be difficult to meet using materials that

contain transition or noble metals [271]. Already, hydrogenated h-BN is thought to be a potential photocatalyst as a material that is active under visible light and has a band gap roughly in line with the reduction and oxidation potentials of water [11]. Similar efforts are being made to develop graphene into a photocatalyst by modification of its band gap, and also as a support to other photocatalytic materials [12, 13]; as in the case of CdS particles dispersed on graphene that have a ~ 5 times higher quantum efficiency for H_2 formation from water splitting, than unsupported CdS nanoparticles [13].

An important aspect to consider, if using graphene and h-BN based materials as catalysts, is their degree of selectivity. A high degree of selectivity is an extremely desirable property for any catalyst and indeed, the rational design of metal-based heterogeneous catalysts is the focus of intense research (see *e.g.* Refs. 272–278). However, even in these cases the metal-based catalysts do not necessarily have very different selectivities, and although they can be doped or alloyed to vary their reactivity, the effect on reaction energies and barriers is often a constant shift with respect to different molecules [278–281]. For instance, in the reaction pathways towards H_2 formation discussed by Cortright *et al.*, a metal catalyst is used throughout, which also catalyses H_2 consuming reactions instead [282]. Meanwhile, Guo *et al.* have shown that a more complex selective catalyst gives rise to a higher conversion rate of methane to H_2 in their non-oxidative scheme [283].

Here we investigate water and some other environmentally and industrially relevant small molecules with density functional theory (DFT). The particular focus of this chapter is to establish the thermodynamics of dissociative adsorption and how this is affected by doping. From this work we draw a number of conclusions. First, doping strongly affects the dissociation process, in some situations making dissociation more favourable by several electronvolts. Second, different surfaces have varying reactivity for the set of molecules considered, with some substrates significantly enhancing the reactivity of polar molecules and others enhancing the reactivity of non-polar adsorbates.

Below, we begin by describing our computational setup in Section 7.3 and present our DFT results for water adsorption in Section 7.4.1, followed by an overview regarding the relative adsorption of other molecules in Section 7.4.2. In Section 7.5 we discuss the trends observed in adsorption sites and structures, and propose a general framework for dissociative adsorption before finally concluding, in Section 7.6.

7.3 Methods

The dissociative adsorption of a water monomer and other molecules on graphene, h-BN, and their doped counterparts was calculated using DFT and the VASP 5.3.2 [177–180] with standard PAW potentials [181, 182] to model the core region of atoms.

7.3.1 System setup

The graphene and h-BN substrates are modelled using (5×5) hexagonal unit cells containing 50 atoms, for which adsorption energies are converged to less than 10 meV with respect to (7×7) unit cells. After a series of convergence tests for the plane-wave cut-off energy we chose to use a 400 eV energy cut-off, which gives dissociative adsorption energies converged to within 16 meV of a 600 eV energy cut-off. Γ-point sampling of reciprocal space for the (5×5) cell was used but **k**-point densities up to $(9 \times 9 \times 1)$ were tested. Adsorption energies using Γ-point sampling are within 50 meV (3%) of the converged adsorption energies for all substrates. Spin polarisation was applied since hydrogen atom pre-adsorption on the substrates gives rise to spin polarised states. A 10 Å separation in the z-direction between substrates without a dipole correction proved to be converged for dissociative adsorption energies of water compared to using a dipole correction or a 20 Å separation (< 15 meV difference).[1]

For the dissociative adsorption energies evaluated here (spanning a few eV) we have mostly used the Perdew-Burke-Ernzerhof (PBE) [173] generalised gradient approximation exchange-correlation functional. However we have also verified that the key results obtained here are not particularly sensitive to the choice of exchange-correlation functional, as discussed in Section 7.5.

There are many different ways of isoelectronically doping graphene with BN and *vice versa* and as a first step we focus on low concentrations of doping: one pair of BN substituting two C atoms in a (5×5) unit cell of graphene which we refer to as boron nitride doped graphene (BNDG) and likewise, two C atoms substituting a BN pair in a (5×5) unit cell of h-BN, henceforth referred to as 2CBN. Doped substrates are modelled by isoelectronically doping the pristine sheets and relaxing the unit cells using a plane-wave energy cut-off of 600 eV to remove any strain introduced by the mixture of B, N and C atoms. Relaxation effects are

[1] For methanol the separation distance in the z-direction was increased to 20 Å to allow space for the larger adsorbed fragments.

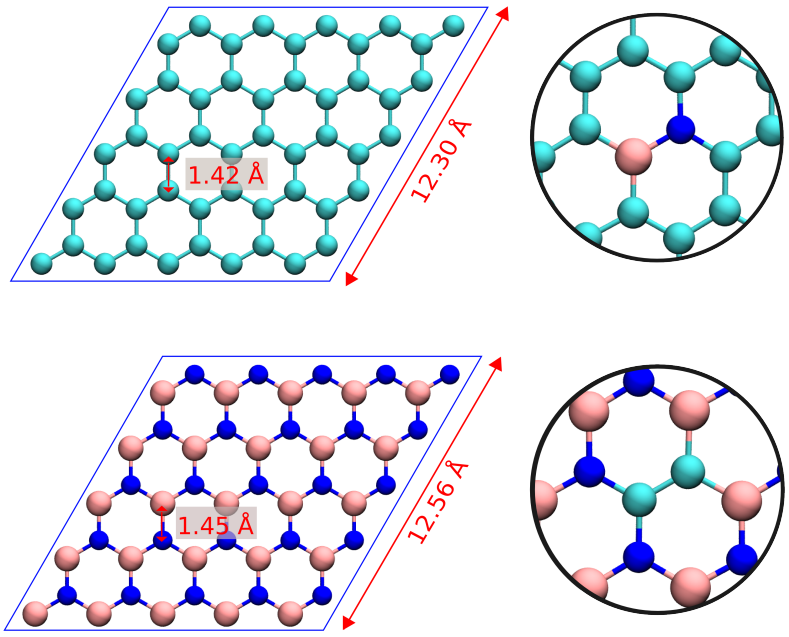

Figure 7.1: The clean and doped graphene and h-BN surfaces considered in this chapter. (a) (5×5) unit cell of graphene. (b) BN doping in (5×5) unit cell of graphene which we refer to as BNDG. (c) (5×5) unit cell of h-BN. (d) C doping in (5×5) unit cell of h-BN, referred to as 2CBN. For clarity only a small portion of the (5×5) unit cell is shown in (b) and (d). C is coloured cyan, B is pink, and N is blue.

small: less than 1% of the relaxed lattice constant of the undoped system.[2]

When water dissociates on a 2D substrate there are a number of possible adsorption scenarios. Here, we have focused on four possible outcomes. Schematic illustrations are given in Fig. 7.2 and in brief they involve: (i) An OH group on the surface and the release of (half) an H_2 molecule, referred to as "OH (½H_2 gas)"; (ii) The adsorption of both OH and H components of water on the surface, with them both being on one side of the substrate, namely "cis(OH–H)". We consider this configuration to be particularly important because 2D materials tend to be examined by supporting them on other materials, leaving only one side of the surface exposed; (iii) The adsorption of both OH and H on the surface but this time on opposite sides of the substrate, referred to here as "trans(OH–H)". This could arise from having the substrate suspended in a wet environment or from the H atoms diffusing through the sheet and there are indications that graphene and h-BN are permeable to protons [285]. However, as it is not clear how likely it is for molecules to dissociate on different sides of the substrates, we consider this configuration to be less relevant than cis(OH–H); (iv) Lastly, "OH–H–H" which is again the adsorption of both OH and H, this time on a surface that has an H atom pre-adsorbed. We tested this particular set-up in light of previous experimental and simulation work, where this is thought to cause water dissociation [10]. Many adsorption sites are available for each category and we have calculated only a number of possibilities: ortho, meta, and para positioning of the adsorbed components with respect to each other, as well as adsorption of the components far away from each other and the doping site in the substrate.

The absolute adsorption energy for dissociative adsorption, E_{ads} is defined as,

$$E_{ads} = E^{tot}_{ads/sub} - E^{tot}_{sub} - E^{tot}_{ads} \tag{7.1}$$

where $E^{tot}_{ads/sub}$ is the total energy of the adsorption system, E^{tot}_{sub} is the total energy of the relaxed substrate, and E^{tot}_{ads} is the energy of the intact molecule in the gas phase. Equation

[2]We verified the stability of the doped substrates by calculating their cohesive energies and we find good agreement with other work for similar arrangements of doping atoms [284]. Cohesive energies for the different substrates have been calculated as $E_{coh} = E^{tot}_{sheet} - N_C E^{tot}_C - N_B E^{tot}_B - N_N E^{tot}_N$ where E^{tot}_{sheet}, E^{tot}_C, E^{tot}_B and E^{tot}_N are the total energies of the sheet and gaseous C, B and N atoms in the unit cell, respectively, and N_C, N_B and N_N are the numbers of C, B and N atoms in the unit cell. The doped sheets in this chapter have cohesive energies between that of graphene and h-BN, and the four substrates range between −7.06 and −7.84 eV/atom.

7.1 is used for all but one adsorption state, that is OH (½H_2 gas). Here we also take into account the energy ($E^{tot}_{H_2}$) of the ½H_2 gas molecule that is formed:

$$E_{ads} = E^{tot}_{ads/sub} + {}^1\!/_2 E^{tot}_{H_2} - E^{tot}_{sub} - E^{tot}_{ads} \tag{7.2}$$

Within these definitions negative adsorption energies correspond to favourable (exothermic) adsorption processes. Bond strengths of hydrogen and hydroxyl to the surfaces are calculated with respect to a gas phase hydrogen atom or hydroxyl group instead of the whole molecule:

$$E_{bond} = E^{tot}_{sub} + E^{tot}_{ads} - E^{tot}_{ads/sub} \tag{7.3}$$

7.4 Results

We begin with the results for the dissociative adsorption of water on the pure substrates, graphene and h-BN, and on the doped substrates, BNDG and 2CBN. In general, we find that the dissociation of water is more facile on the doped substrates and is also strongly affected by the presence of a pre-adsorbed H atom, local electronic induction, and steric effects arising from rehybridisation of orbitals in the substrate atoms. We use these insights to look at the adsorption of H_2, methane, and methanol on the same surfaces in Section 7.4.2. From our analysis we see that different substrates favour the dissociation of different molecules, depending on their polarity, enabling us to make comparisons between the adsorption behaviour of polar and non-polar molecules and fragments.

7.4.1 Dissociative adsorption of water on graphene, h-BN, BNDG and 2CBN

Fig. 7.2 reports results for the dissociative adsorption of water on the clean and doped substrates. It can be seen that the energetics of the dissociation process varies significantly for the various adsorption structures and substrates.

On pristine graphene we find that dissociation is strongly endothermic in agreement with previous work [149, 286]. In addition the energy of the dissociation process varies by as much as 2 eV depending on the final adsorption configuration. The lowest adsorption configuration on pristine graphene is trans(OH–H) (2.19 eV) with OH and H in ortho positions, in agreement

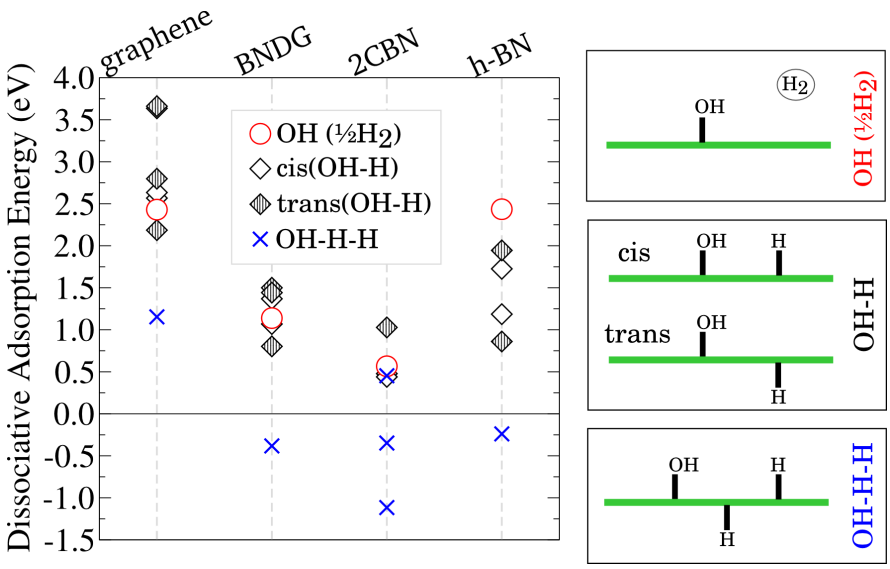

Figure 7.2: The dissociative adsorption energy of water on graphene, BNDG, 2CBN and h-BN is shown for different adsorption structures. Red circles indicate the adsorption of OH from water onto the substrate and the release of hydrogen gas. The black diamonds indicate the dissociative adsorption of a water molecule into OH and H on the substrate. The blue crosses correspond to the adsorption energies on a hydrogenated substrate. The categories of water dissociation on the substrate are illustrated on the right.

with Xu *et al.*[149] The cis(OH–H) configuration shown in Fig. 7.3 (a) on graphene has a dissociative adsorption energy of 2.57 eV and is thus $\sim$ 0.4 eV less stable than trans(OH–H). Dissociative water adsorption is in general, more thermodynamically favourable on h-BN than on graphene. For example the cis(OH–H) state on pristine h-BN shown in Fig. 7.3 (d), has E_{ads} of 1.19 eV and is 1.38 eV more favourable than the equivalent structure on graphene. Nonetheless, given just how thermodynamically unfavourable water dissociation is, it is unlikely that water monomers will dissociate on pristine graphene and h-BN.

Upon moving to the doped substrates, for which numerous configurations were considered, we find a significant lowering in the energy to adsorb water. From graphene to BNDG, and from h-BN to 2CBN, we gain $\sim$ 1 eV in the adsorption of a water molecule. The cis(OH–H) state and lowest energy dissociation state for each doped surface is shown in Fig. 7.3. On both BNDG and 2CBN, B–OH and C–H bonds are formed. Note from Table 7.1 that the B–OH bond is $\sim$ 1.3 eV stronger on BNDG than on h-BN (or C–OH on graphene). Hence, a marked activation of the B atom towards binding OH results from the mixture of N and C atoms surrounding it and in this way doping leads to a considerable lowering of the dissociative adsorption energy.

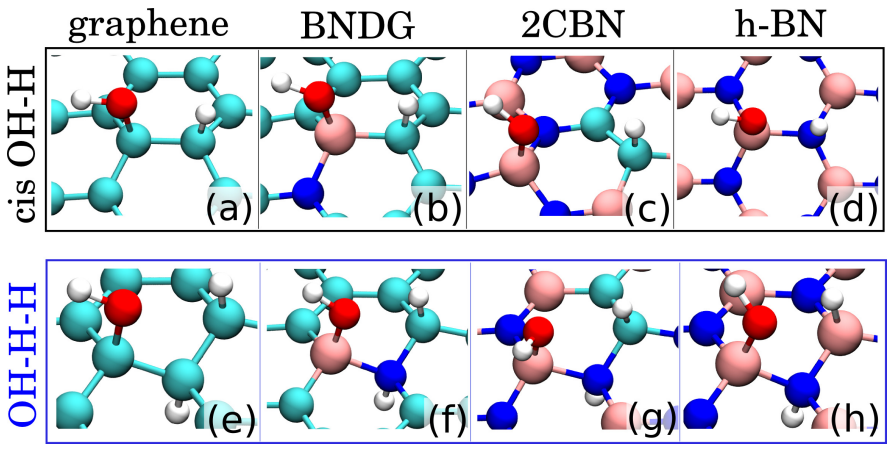

Figure 7.3: The most stable cis(OH–H) (top panel) and most stable overall dissociative adsorption structures (lower panel) of water on graphene, h-BN, BNDG and 2CBN are shown. (a) and (e) are water on pristine and hydrogenated graphene, respectively. (b) and (c) show water adsorbed on BNDG and 2CBN, whilst (f) and (g) show water adsorption on the hydrogenated counterparts. (d) and (h) are on pristine and hydrogenated h-BN, respectively.

The presence of the pre-adsorbed H atom also significantly improves the thermodynamics of water adsorption by $\sim$ 1 eV for each substrate. Favourable OH–H–H configurations are shown in Fig. 7.3 and from Fig. 7.2 it can be seen that water splitting is thermodynamically favourable on the hydrogenated h-BN (-0.24 eV), BNDG (-0.38 eV) and 2CBN (-1.12 eV) surfaces. Thus doping and hydrogenating both graphene and h-BN makes the thermodynamics of water dissociation considerably more favourable. The general conclusion that pre-adsorbed hydrogen facilitates water dissociation is in agreement with Siria *et al.*[10] Interestingly, the overall most favourable states for water dissociation on the doped surfaces contain a B–N–C construction in the surface where B–OH, N–H, and C–H bonds are formed. We considered if the increased reactivity at these sites is due to the pre-adsorbed H atom on a N site destabilising the surface and thus activating it towards water adsorption, but this is unlikely because the N–H bond is very weak (only 0.07 eV). The B–N–C construction in the surface of doped substrates is therefore central to making the dissociation energy more exothermic, and exemplifies the use of isoelectronic doping to tune the dissociative adsorption energy of water. In all OH–H–H states, the OH and H components of the dissociated water are arranged in a hydrogen bonded fashion. The hydrogen bond on h-BN at 1.95 Å is shorter than the hydrogen bond on graphene (2.23 Å) despite the slightly smaller lattice constant of graphene. The hydrogen bonding distances are indicative of the more polarised binding of OH and H on h-BN, which culminates in a more negative oxygen atom in the OH group and

hence a shorter hydrogen bond.

Additional DFT calculations of water dissociation on the protonated (as opposed to hydrogenated) substrates were also performed. These reveal that protonation is slightly less effective than hydrogenation but still increases the tendency of water to dissociate by ~ 0.8 eV with respect to the non-protonated clean surfaces. Thus either hydrogen pre-adsorption or acidic conditions (pre-adsorbed protons) could be key elements in the activation of these sheets towards dissociative water adsorption.

Before moving on to discuss the other adsorbates, two additional features of these adsorption systems deserve comment. First, adsorption of the dissociated fragments on separate sides of the sheet (so-called trans adsorption) is favoured in general. Specifically, trans-ortho(OH–H) adsorption is ~ 0.4 eV more stable than cis-ortho(OH–H) on graphene. This is consistent with previous work on graphene [287–291] and demonstrates the stabilisation gained by adhering to a more tetrahedral structure around the sp^3 hybridised C atom. Likewise on h-BN and BNDG, the tetrahedral arrangements of trans(OH–H) and OH–H–H lead to lower dissociative adsorption energies (by about 0.3 eV). Note the 2CBN system is an exception and the most stable (OH–H) configuration on 2CBN has cis-para positioning, shown in Fig. 7.3(c). The trans-ortho (OH–H) state on 2CBN is still close in energy and only 0.04 eV less stable than cis-para[3]. This can be explained by the difference in partial charges on the B atoms bonding to OH in each case. Electronegative N atom neighbours make B atoms more positive and subsequently form a stronger polar bond with OH. In the trans-ortho state, the B atom is surrounded by only two N atoms and hence, is not as electrophilic as the B atom in the cis-para state which is bonded to three other N atoms. This example in 2CBN demonstrates that inductive effects from neighbouring atoms dominate over steric effects. Despite the advantage of satisfying the sp^3 hybridisation in trans adsorption states, it is important to remember that in practice 2D materials are often suspended or grown over substrates [138, 292–299] (metals or silicon carbide) where cis configurations are more likely.

Second, inductive effects are also introduced by the adsorbed water fragments. This can be seen by comparing the co-adsorbed to the separately adsorbed OH and H fragments. Specifically, OH ($\frac{1}{2}H_2$ gas) adsorption on graphene and h-BN only differ by 5 meV and

[3]The 0.04 eV difference between cis-para and trans-ortho adsorption configurations remained the same using a denser $6 \times 6 \times 1$ **k**-point mesh.

Table 7.1: Bond strengths (in eV) for H and OH on graphene, h-BN and BNDG sheets with respect to a gas phase hydrogen atom or OH molecule. Parentheses indicate neighbouring atoms in the substrate. Negative bond energies correspond to endothermic but metastable adsorption minima. No minimum was found for OH adsorbed on the N atom.

Bond	Bond strength (eV)
Graphene	
C–H	0.81
C–OH	0.67
h-BN	
N–H	−0.77
B–H	−0.01
B–OH	0.67
BNDG	
B–H	0.98
N–H	0.07
(B)C–H	1.15
(N)C–H	1.04
B–OH	1.96
(B)C–OH	0.84
(N)C–OH	1.03

indeed the C–OH and B–OH bond (as listed in Table 7.1) in graphene and h-BN are almost identical. In contrast C–H bonds in graphene are significantly stronger than N–H bonds in h-BN, implying that OH–H on graphene might be more stable, and yet water adsorption is more exothermic on h-BN. It follows that the binding of hydrogen atoms on the surface perturbs the local electronic structure and therefore, the bond strength of OH to the surface, such that the OH–H configuration is considerably more stable on h-BN than on graphene.

It is useful to explain these trends in terms of the physical properties of the surfaces and we have done this by looking at Bader charges [300, 301], average electrostatic potentials at each atom, and Kohn-Sham orbitals of the dissociated states.[4] Comparison of the adsorption structures and Bader charges suggests the most stable adsorption states arise from: (i) C–H in which the C site has the most negative partial charge across the surface; (ii) B–OH in which the B atom is positive and susceptible to nucleophilic attack; and (iii) N–H in which the N atom is the most negative and therefore the strongest nucleophile. A careful analysis reveals that the adsorption of water is affected by a combination of factors involving orbital overlap and electrostatic interactions. Graphene has weaker electrostatic interactions with

[4]Of course there are many ways to project charges onto atoms and Bader charges discussed here are simply used for pinpointing the relevant trends in the materials.

water than h-BN, but better orbital overlap (evidenced by bond strengths in Table 7.1). In contrast, hybrids of h-BN and graphene have stronger electrostatic interactions with water than graphene, and also stronger orbital overlap with water than h-BN. Due to these combined effects doped graphene and h-BN are more suited for the adsorption of water. Evidently for a given substrate, electrostatic interactions with a molecule are determining the site of adsorption (*e.g.* in 2CBN the cis-para state of water is more stable than the trans-ortho).

To recap, isoelectronic doping has a significant impact on the thermodynamics of water dissociation of graphene and h-BN. The most thermodynamically favourable adsorption identified is the OH–H–H configuration on 2CBN with an adsorption energy of -1.12 eV. The strong adsorption energy on 2CBN can be attributed to: (i) the B–OH bond in which the B atom is more positive compared to B atoms in the other substrates; and (ii) a stronger C–H bond at 2CBN as opposed to a B–H bond at h-BN.

7.4.2 Dissociative adsorption of hydrogen, methane, and methanol

With the insight gained from water adsorption, we also calculated the dissociative adsorption of H_2, methane, and methanol. As before, various configurations were calculated for each system and in Fig. 7.4(a) we report the most favourable dissociation energies found for the molecules on the same side (cis configurations) of the pure and doped substrates. The change in zero point energy (ZPE) upon dissociative adsorption for each system is also included in the energies in Fig. 7.4. ZPEs were calculated using the harmonic approximation and we find that the change in ZPE increases the dissociative adsorption energies by up to 0.3 eV, which is certainly not insignificant. In some cases the adsorption energies of the trans states are more favourable than cis but since it is more feasible for adsorbates to dissociate on the same side of the substrate, we show results only for cis configurations.

From these calculations with the other adsorbates we learn two key things. First, doping of the pristine substrates helps the thermodynamics of dissociation for these molecules too. Second, the details are quite different, with methanol behaving in a similar manner to water by benefiting most from BN doping in graphene, whereas H_2 and methane benefit most from C doping in h-BN. Figs. 7.4 (b) and (c) illustrate this latter point by showing the gain in dissociative adsorption energy for each molecule as a result of doping in the pristine substrates.

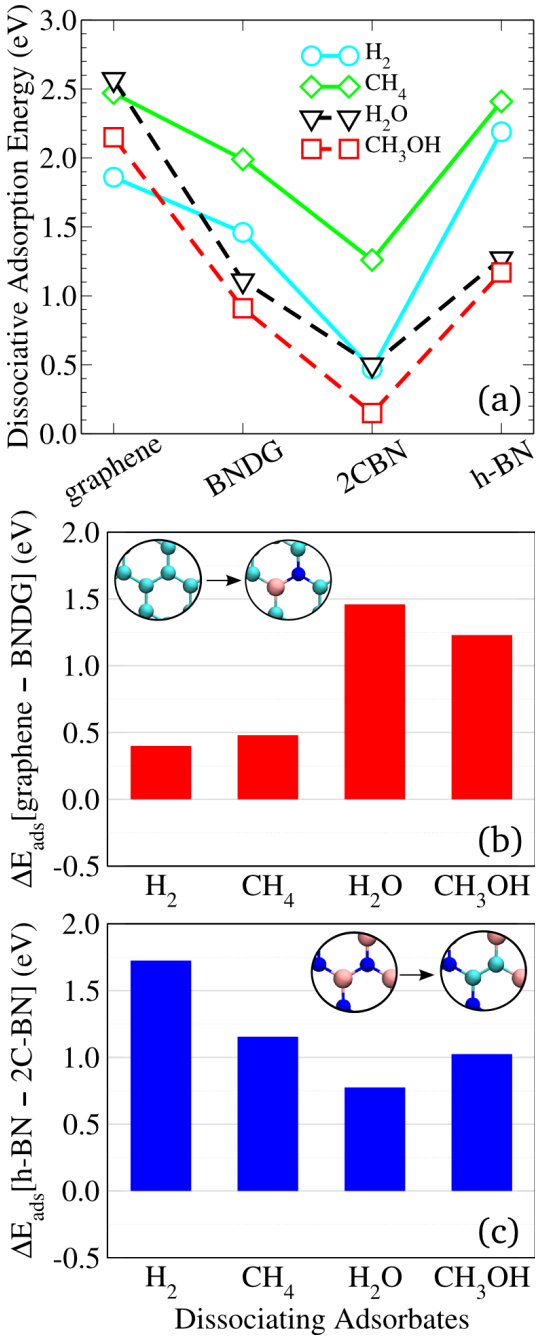

Figure 7.4: (a) Dissociative adsorption energies including ZPE contributions of H_2, methane, water, and methanol on graphene, BNDG, 2CBN and h-BN. H_2 in blue circles, methane in green diamonds, water in black triangles, and methanol in red squares. Results are given only for the most stable adsorption structure for each molecule and substrate with the fragments adsorbed on the same side of the substrate and without pre-adsorbed hydrogen. (b) Gain in adsorption energies from doping pristine graphene with BN (in eV) for different molecules, illustrating a marked increase in the reactivity with polar adsorbates. (c) Gain in adsorption energies from doping pristine h-BN with 2C (in eV) for different molecules and here the reactivity with non-polar adsorbates increases more significantly. The insets in (b) and (c) illustrate the doping.

The adsorption of methanol varies in a similar way to water across the different substrates and favours the same adsorption sites (ortho on graphene, BNDG, and h-BN, and para on 2CBN). From Fig. 7.4 we see that water and methanol adsorption energies both become more favourable by ~ 1.4 eV as the substrate is changed from graphene to BNDG. Having established that the C–OH to B–OH change in bond energy is the main contributor to the difference in adsorption energies for water on graphene and BNDG, we can deduce that the same is true for methanol. Note that the adsorption of methanol is stronger than that of water on all substrates by $0.2 - 0.4$ eV. On graphene, BNDG, and 2CBN the C–O bond of methanol is broken preferentially with the CH_3 fragment bonding to the substrate at the same sites as the H from water does. However on h-BN, the O–H bond is broken instead, resulting in N–H and B–OCH_3 bonds with the h-BN substrate.

Meanwhile the non-polar molecules, H_2 and methane, also benefit from doping of the pristine substrates but in particular from C doping in h-BN. This appears to be because the alkene-like bond between the two C atoms, which is susceptible to alkene addition reactions, is particularly effective at breaking weakly polarised bonds. Methane and H_2 follow exactly the same trend but H_2 is adsorbed around 0.6 eV more strongly overall.

By tracking the lowest adsorption states across the substrates in Fig. 7.4(a), we see that the preference for H_2 and water switch; H_2 adsorbs preferably on graphene and water is preferred on BNDG and pure h-BN. H_2 and water have almost the same dissociative adsorption energies on 2CBN (~ 0.5 eV). The different adsorption preferences that depend on the isoelectronic substrate doping is a significant outcome, especially given that these materials are composed of sustainable and abundant elements, making them desirable candidates for catalysis.

Finally, as with water adsorption we also examined the effect of hydrogen atom pre-adsorption on the dissociative adsorption energy of these small molecules. We found in a similar manner to water that dissociative adsorption becomes more favourable by $0.7 - 1.5$ eV on the hydrogenated surfaces, such that H_2, water, and methanol have exothermic dissociative adsorption energies on BNDG, 2CBN, and h-BN. Thus, as with water, doping and hydrogenation significantly improves the energetics of dissociative adsorption on graphene and h-BN.

7.5 Discussion and general framework

Some important trends can be observed from the adsorption structures and energies of water and the other molecules studied here, which are likely to apply in general to polar and non-polar adsorbates on BNDG and C doped h-BN systems. Although we have studied water adsorption more extensively, the trends also hold for H_2, methanol, and methane. To summarise:

- Isoelectronic doping of graphene with BN increases the reactivity with polar adsorbates (*i.e.* water and methanol) by ~ 1.4 eV but only changes the reactivity with non-polar adsorbates by ~ 0.5 eV. Conversely, isoelectronic doping of h-BN with C increases the reactivity most with H_2 and methane, by $1.2 - 1.8$ eV.

- Hydrogen atom (or proton) pre-adsorption on the substrate significantly improves the thermodynamics of dissociation for the molecules considered by ~ 1 eV (~ 0.8 eV), resulting in exothermic dissociative adsorption, and suggesting that acidic conditions aid dissociation on the substrates.

- The most exothermic adsorption sites for polar adsorbates share the B–N–C construction, in which there is already a H atom pre-adsorbed on a N atom. Meanwhile, non-polar adsorbates favour C–C sites with localised electrons (as in 2CBN).

- Local electronic inductive effects dominate over steric effects. In other words, para-positioning of molecule fragments is possible (however ortho is generally favoured) if the atoms in the substrate have a larger electrostatic potential in the para sites.

- Atoms in the substrate that change to sp^3 hybridisation as a result of chemisorption prefer to be in a more tetrahedral arrangement, *e.g.* the trans-ortho configuration is ~ 0.3 eV more stable than cis-ortho.

Some comments related to these trends are appropriate. First, all the numbers given have been derived from the PBE exchange-correlation functional. It is well known that bond strengths and adsorption energies vary from one functional to the next [43, 59] and PBE in particular neglects van der Waals dispersion forces and does not include exact exchange. Indeed, previous work on similar systems to those considered here, namely the physisorption of

water on h-BN [65] and on BN doped benzene [213], has shown that vdW interactions can be important. Here, however, we are concerned with strongly bonded chemisorption structures of the dissociated fragments of water and the other molecules involving an energy scale of several electronvolts. Nonetheless we have investigated the dissociative adsorption energies for all states in Fig. 7.4 using the vdW-inclusive optB86b-vdW functional [32, 36, 214]. We find that the inclusion of vdW interactions makes the thermodynamics of dissociative adsorption energy more favourable by $0.2 - 0.5$ eV. With this functional some adsorption states are exothermic even in the absence of pre-adsorbed hydrogen. In contrast, when we look at the thermodynamics of water adsorption with B3LYP [185–188], that accounts for some exact exchange but not dispersion, dissociative adsorption is less favourable by *circa* 0.2 to 0.4 eV. It is clear therefore that the thermodynamics of dissociative adsorption is sensitive to the choice of exchange-correlation functional, with the PBE values presented here resting in the middle of three functionals considered. Importantly, the relative energies and trends across the surfaces remains unchanged whether or not dispersion interactions or exact exchange are accounted for.

Second, when probed experimentally 2D materials like graphene and h-BN are often adsorbed on a support material such as metals or silicon carbide. We have not included supporting materials in this chapter but the electronic properties of graphene and h-BN can be influenced by the choice of support [138, 292–298]. Metals for instance, can hybridise the p_z-states in graphene and the N atoms in h-BN, and thus alter the reactivity of the surfaces [292, 294, 295]. It is also known that differences in the lattice constants of the 2D material and support can lead to an undulating moiré structure in which different regions of the 2D overlayer interact differently with the substrate [138, 293, 296, 298, 299]. It would be interesting in future work to explore how the presence of a substrate alters the trends observed here.

Third, we have seen that depending on the type of doping the thermodynamics of dissociation of either polar or non-polar molecules can be enhanced. This would potentially be exploited in heterogeneous catalysis where it is generally desirable to identify catalysts that can cleave specific bonds and as a result enhance the selectivity towards a particular reaction product. In future work it would be interesting to explore this possibility through calculations of the kinetics of dissociation on the substrates considered here. However, since it is now well

established that reaction barriers for chemical reactions at surfaces correlate well with the thermodynamics, it is not unreasonable to suggest that the thermodynamic trends identified here could lead to interesting catalytic behaviour.

7.6 Conclusion

To conclude, the dissociative adsorption of water, H_2, methane, and methanol has been studied on pristine graphene and h-BN, and on their doped counterparts: BNDG and 2CBN. By calculating the absolute adsorption energies of numerous configurations using DFT, we have identified some interesting trends. Most notably, isoelectronic doping of the pristine surfaces makes the dissociation process more favourable generally by at least 1 eV. Based on electronic structure analyses, we conclude that the increased reactivity of the surface is because B atoms (as a doping species) are more susceptible to nucleophilic attack, and in 2CBN the C–C double bond is more susceptible to alkene addition-like reactions. These changes in the local electronic structure favour particular adsorption configurations. The OH component bonds strongly to the doping B atom, whilst H atoms bond preferentially to C compared to either B or N atoms. Hence, methanol behaves very similarly to water as a polar molecule, because of the OH group. In the same vein, H_2 and methane follow the same trend across the different surfaces, with both binding preferentially on 2CBN, where there is a high energy C–C double bond.

The results presented in this chapter also suggest that adsorption is exothermic in the presence of adsorbed H atoms (or protons) on the surface. Thus, there could be important implications for the transport properties and chemical reactions of water and other molecules across doped graphene and h-BN membranes, and conditions (acidic or basic) are likely to be useful gauges for altering the interaction with molecules. In addition, it is more thermodynamically favourable to adsorb molecules in a trans configuration, with components alternating above and below the sheet in order to adhere to a tetrahedral arrangement around sp^3 hybridised substrate atoms. Although it is some way from the freestanding systems considered here, this hints that 2D sheets suspended freely in solution could be more suited for dissociative adsorption of molecules.

Finally, we observe variations in the thermodynamics for the set of molecules considered

depending on the surface. Again we caution that the calculation of reaction barriers and even rates is an important next step but these results suggest that one can vary the preference for H_2 dissociative adsorption to that of water or methanol for example, and consequently alter the course of reaction pathways in either H_2 or methanol formation processes. Consider for example the wasteful dehydration and methanation reactions in Cortright *et al.*'s reaction pathways catalysed by a metal for H_2 production [282]; wherein H_2 is consumed by reacting with CO_2 at low temperatures to produce alkanes and water. This reaction can be avoided if methanol, methane, and water are split more readily than H_2. According to our findings this might be achievable for methanol and water by doping graphene with BN. Overall, our results indicate that isoelectronically doped graphene and h-BN could exhibit interesting chemical and catalytic activities which could potentially be exploited.

Chapter 8

Using alchemical derivatives for efficient screening

The design and production of novel 2-dimensional materials has seen great progress in the last decade, prompting further exploration of the chemistry at such materials. High throughput screening methods can provide particularly effective ways to explore chemical compound space. Here, alchemical derivatives are used as a method to screen the dissociative adsorption energy of water on various BN doped topologies of hydrogenated graphene. The predictions from alchemical derivatives are assessed by comparison to density functional theory. This screening method is found to predict dissociative adsorption energies that span a range of -2.8 to -0.5 eV, with a mean absolute error < 0.1 eV. Furthermore, the quality of such a prediction can be readily assessed by examination of the Kohn-Sham highest occupied molecular orbital in the initial states. In this way, the root mean square error in the dissociative adsorption energies of water is reduced by up to an order of magnitude (down to ~ 0.02 eV) after filtering out poor predictions. The findings point the way towards a reliable use of first order alchemical derivatives for efficient screening procedures.

8.1 Introduction

Recognising the enormous number of ways in which elements can be combined is both exciting and daunting in the search for more efficient, more sustainable, and more elegant materials for medical, engineering, and catalytic applications. High throughput screening in compu-

tational chemistry, otherwise known as virtual screening, is paving the way for materials discovery across academic and industrial research. Greeley *et al.* exemplified it by computationally screening through 700 binary surface alloys to find a material with high activity for H_2 evolution [31]. The computational screening lead to the discovery and subsequent synthesis of BiPt which experimentally showed comparable activity to pure Pt. Yet there are various ways to screen through materials for which the reader is referred to some recent perspectives, see Refs. 30, 302, 303.

Focusing on 2-dimensional materials, there are countless ways in which elements can be combined, surfaces doped, and substrates tuned. In Chapter 7 for example, it was shown that pure graphene is inert to the dissociative adsorption of water whereas, BN doped and hydrogenated graphene is far more likely to dissociate water. Here we investigate how BN doping, away from the adsorption site, affects the adsorption energy of water. In a unit cell of graphene containing 50 atoms, there are already hundreds of ways to arrange a pair of boron and nitrogen atoms - even after accounting for redundancies by symmetry. It follows that high-throughput screening is an ideal method to invoke for exploring such a system.

The isoelectronic nature of doping in this study, and the closeness of boron, nitrogen, and carbon in proton number, can be utilised for efficient screening. Specifically, we can look to alchemical derivatives within molecular grand-canonical ensemble density functional theory (DFT). This method relies on exploiting *free information* in the form of the average electrostatic potential at each atom from DFT calculations. Such conceptual DFT has been discussed comprehensively in some works [304–307], but here we give a brief introduction to the method employed.

Firstly, a system within chemical compound space can be referred to as a discrete chemical thermodynamic state. In DFT, such a state is defined by the charge density, that is calculated from the proton distribution $Z(\mathbf{r})$ and the number of electrons N_e. As such, $Z(\mathbf{r})$ and N_e are the extensive particle variables. In accordance with thermodynamic integration and perturbation methods, the mutation of a chemical thermodynamic system into another can be approximated using a Taylor expansion around the initial system, and a switching parameter λ,

$$E(\lambda = 1) = E^0 + \partial_\lambda E^0 \Delta\lambda + \frac{1}{2}\partial_\lambda^2 E^0 \Delta\lambda^2 + \ldots, \tag{8.1}$$

where $\lambda = 0$ corresponds to the initial system, $\lambda = 1$ corresponds to the target system and hence, $\Delta\lambda = 1$. Importantly, as we see below, the first order term in Eq. 8.1 can be evaluated from a single DFT calculation of the initial state. In general, the first order term ($\partial_\lambda E^0$) includes the variance of the energy with changes in the proton density, the nuclear positions, and the number of electrons. However, here we consider the isoelectronic doping of a graphene sheet, with fixed atomic positions. Therefore, terms involving changes in atomic positions $\{\mathbf{R}_I\}$ and N_e can be neglected leaving,

$$\partial_\lambda E = \int d\mathbf{r} \delta_{Z(\mathbf{r})} E \partial_\lambda Z(\mathbf{r}), \tag{8.2}$$

where the variation of the energy with respect to a small change in proton density is known as the nuclear chemical potential, $\mu_n(\mathbf{r})$,

$$\partial_\lambda E = \int d\mathbf{r} \mu_n(\mathbf{r}) Z(\mathbf{r}). \tag{8.3}$$

At a given atomic position then, $\mu_n(\mathbf{R}_I)$ is the derivative of the energy with respect to the change in the nuclear charge, $Z(\mathbf{R}_I)$. This is referred to as the alchemical potential since it describes the energy change as a result of an alchemical mutation at an atomic site. Thus, in isoelectronic doping, the derivative of the energy can be expressed as,

$$\partial_\lambda E = \sum_I \mu_n(\mathbf{R}_I) \partial_\lambda N_I. \tag{8.4}$$

Here, the first derivative of the energy is equated to the sum of the product of alchemical potentials at each atom with the change in atomic number. In fact, the nuclear chemical potential has been previously derived as the electrostatic potential, $\bar{V}_{ESP}(\mathbf{r})$. Furthermore, the average electrostatic potential at each atom - or alchemical potential - is available at the end of a self consistent field (SCF) cycle (at least in the VASP code). As a result, we can compute Eq. 8.4 from the information provided in a single DFT calculation containing all of the atoms involved in the doping.

Alchemical derivatives have been used in this way to predict various properties such as, doping in benzene [308], reaction energies [309], eigenvalues of doped benzene [156], covalent bonds [310], and phases of alkali halide crystals [311]. However, the quality of predictions can

vary significantly and it is expected that the second order derivative in Eq. 8.1 can improve the accuracy of predictions. The second order term contains second order pure and mixed derivatives of the energy of which the alchemical hardness ($\eta_n(\mathbf{r}, \mathbf{r}')$) is of relevance to this study,

$$\eta_n(\mathbf{r}, \mathbf{r}') = \delta_{Z(\mathbf{r})}\delta_{Z(\mathbf{r}')}E = \delta_{Z(\mathbf{r}')}\mu_n(\mathbf{r}). \tag{8.5}$$

As it can be seen, the alchemical hardness is a kernel that requires computation of the target system (by $\mathbf{r}'$) as well as the initial system. Such a calculation would render this scheme inefficient, and alternative relations to this quantity are sought. Drawing insight from the work of Ayers [312] and Cárdenas *et al.* [313], the alchemical hardness can be described either by the variation of the alchemical potential with respect to proton density, or with respect to electron density [313]. The variation of the alchemical potential with respect to electron density is a Fukui function [312] and by Janak's theorem [314], it is the density of the highest occupied molecular orbital (HOMO), ρ_{HOMO}.

In this chapter, the first order alchemical derivative is used to predict the dissociative adsorption energy of water on BN doped graphene, with doping occuring at different sites in the substrate. The predicted energies are compared to explicitly calculated energies to reveal the quality of predictions and to identify any outliers. Moreover, it is shown that outliers can be identified without additional calculations from the knowledge of the electronic structure of the initial state. The study begins with a description of the methods and the system setup in Section 8.2, followed by the results of alchemical predictions in Section 8.3. After identifying the main trends, further questions about the procedure and implications for water adsorption are discussed in Section 8.4 before concluding in Section 8.5.

8.2 Methods

As in Chapter 7, the dissociative adsorption of a water monomer on boron nitride doped graphene (BNDG) was calculated using density functional theory (DFT) and the Vienna *Ab-Initio* Simulation Package (VASP) 5.3.2 [177–180]. VASP uses plane-wave basis sets, and projector augmented wave (PAW) potentials [181, 182] to model the core region of atoms. Standard PBE PAW potentials were used here with a plane-wave energy cut-off of 500 eV. The PBE exchange-correlation functional is used throughout. A (7×7) unit cell of graphene

is used, with 4 carbon atoms replaced by two boron and two nitrogen atoms. The dissociative adsorption energy of water is already converged with a (5×5) unit cell but using a larger cell provides more pathways for alchemical mutation of atoms. The separation between periodic images of the substrate in the z-direction is 15 Å. All calculations were performed at the Γ-point.

8.2.1 System Setup

The adsorption site in the substrate is activated using a pair of BN atoms in the surface and two adsorbed hydrogen atoms shown in Fig. 8.1, which remain unmoved in all paths considered. Doping and hydrogenating in this way has been shown previously to make the surface more reactive towards the dissociative adsorption of water. Dissociative adsorption energy is defined as,

$$E_{ads} = E^{tot}_{ads/sub} - E^{tot}_{sub} - E^{tot}_{ads} \tag{8.6}$$

where $E^{tot}_{ads/sub}$ is the total energy of the adsorption system, E^{tot}_{sub} is the total energy of the substrate (with two hydrogen atoms adsorbed), and E^{tot}_{ads} is the energy of the intact water molecule in the gas phase.

Four schemes of alchemical mutation between carbon, boron, and nitrogen are considered here, illustrated in Fig. 8.2. BN pair 1 and BN pair 2 both involve the prediction of a BN pair in place of two carbon atoms across the surface, starting from a BN pair at the edge of a unit cell. In this way, the prediction involves substituting the BN pair at the edge with two carbon atoms, and correspondingly, two carbon atoms in the surface with a BN a pair. The difference between BN pair 1 and 2 is the position of BN at the dissociation site with respect to the BN pair at the edge of the cell in the initial state; they are distinguishable due to the two sublattices of graphene. The third scheme, "B wander", refers to the swapping of a carbon and boron atom. Similarly "N wander" refers to the swapping of an individual carbon atom with nitrogen. In each case there are 94 possible paths for this unit cell size, such that a total of 376 paths have been looked at here. The initial states are always the same and only two single point DFT calculations are needed per scheme.

Thanks to the geometrical closeness of graphene and hexagonal boron nitride, doping graphene with BN atoms has a small impact on the structure. The largest change in bond

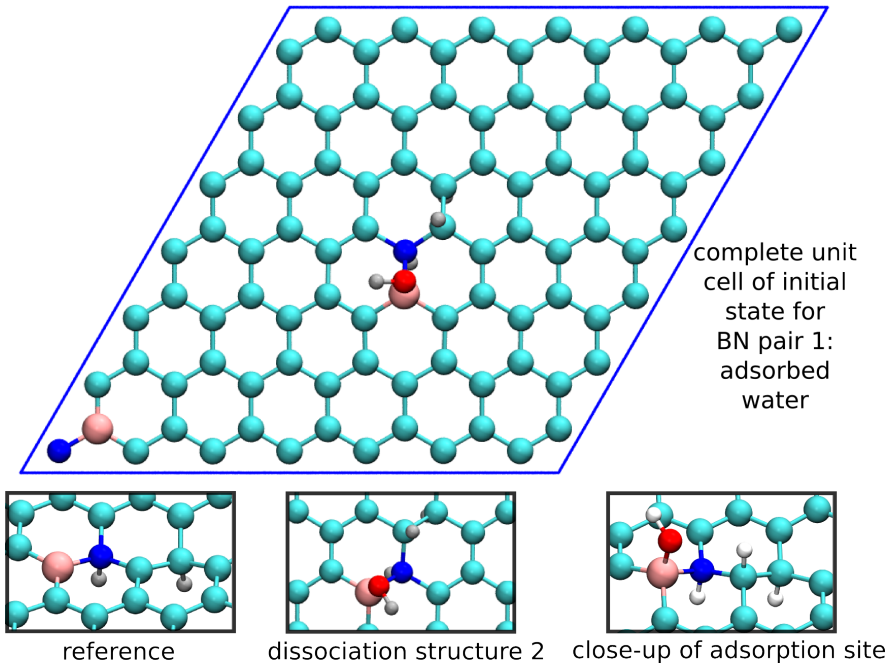

Figure 8.1: Top panel: (7×7) unit cell of graphene doped with two pairs of BN and two hydrogen atoms adsorbed. Water is dissociatively adsorbed on oppostide side to hydrogen atoms. Lower panel: the reference substrate with two hydrogen atoms adsorbed; the adsorption configuration for BN pair 2 using different sublattice; and a close-up of the dissociative adsorption. Carbon is in light blue, nitrogen in dark blue, boron in pink, oxygen in red and hydrogen in grey.

lengths upon relaxation of target systems was seen for boron-carbon bonds, which changed by up to 0.06 Å[1]. This makes fixing the geometry in all calculations a reasonable approximation to begin with.

8.3 Results

For each path the PBE energy of water dissociation has been calculated without relaxing the positions of atoms and compared with the alchemically predicted dissociation energy. Fig. 8.5 shows a scatter plot, comparing these energies, for BN pair 1 (the other schemes produced similar results). From the figure it is clear the majority of predictions are good, but there are some outliers, resulting in an overall poor R^2 correlation coefficient of 0.14. For the other schemes, the R^2 coefficients are similarly unimpressive between 0.17-0.49, and in all cases there are clear outliers. For an effective screening process it would be better to identify outliers *a priori* without further computational cost. Here it is demonstrated how that is possible using

[1]The energy of relaxation gained from this is up to ~ 0.3 eV.

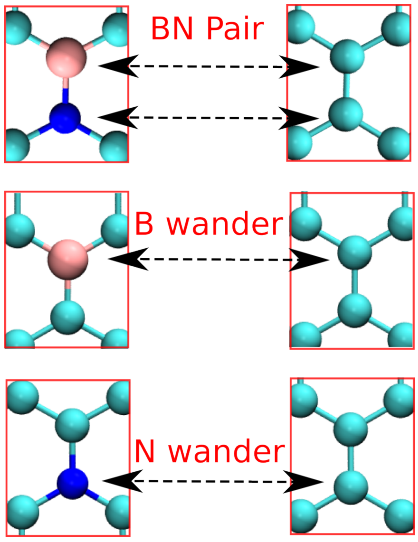

Figure 8.2: Schematics of the alchemical mutations that have been considered: BN pair swapping with two carbon atoms; boron atom swapping with a carbon atom (B wander); and a nitrogen atom swapping with carbon (N wander).

the highest occupied molecular orbital (HOMO) in the initial states.

A Bader charge density partition per atom of the HOMO charge density indicates the prominence of the HOMO at a given atom site. This is indicative of the mesomeric role of the atoms in the carbon substrate: atoms with some charge density in the HOMO are mesomerically active, and those without are mesomerically passive. For a given path, the charge at the sites of mutation in the initial state can be summed to obtain a measure of the extent of mesomeric activity. This combined charge for each path is shown in Fig. 8.4 against the relative absolute error (RAE) for each path. It can be seen that the majority of paths have a RAE less than 0.01 whilst those which have substantial errors also have large HOMO charge associated with them. As a result, the partitioned HOMO charge can be used to strip off the outliers. Note that the correlation is not direct, there are some paths with a high associated HOMO charge but small errors. By choosing a threshold RAE of 0.1, the corresponding charge required to stay below this threshold is ∼0.05 e for the different schemes. In Fig. 8.5, red squares represent HOMO charge of more than 0.05 e and evidently all the poor predictions correspond to mesomerically active sites.

The effectiveness of this procedure is more clearly seen in Table 8.1 where the R^2, Spearman's rank coefficient (ρ), mean absolute errors (MAE) and root mean square errors (RMSE) are reported for each scheme. The MAE and RMSE are an order of magnitude larger for

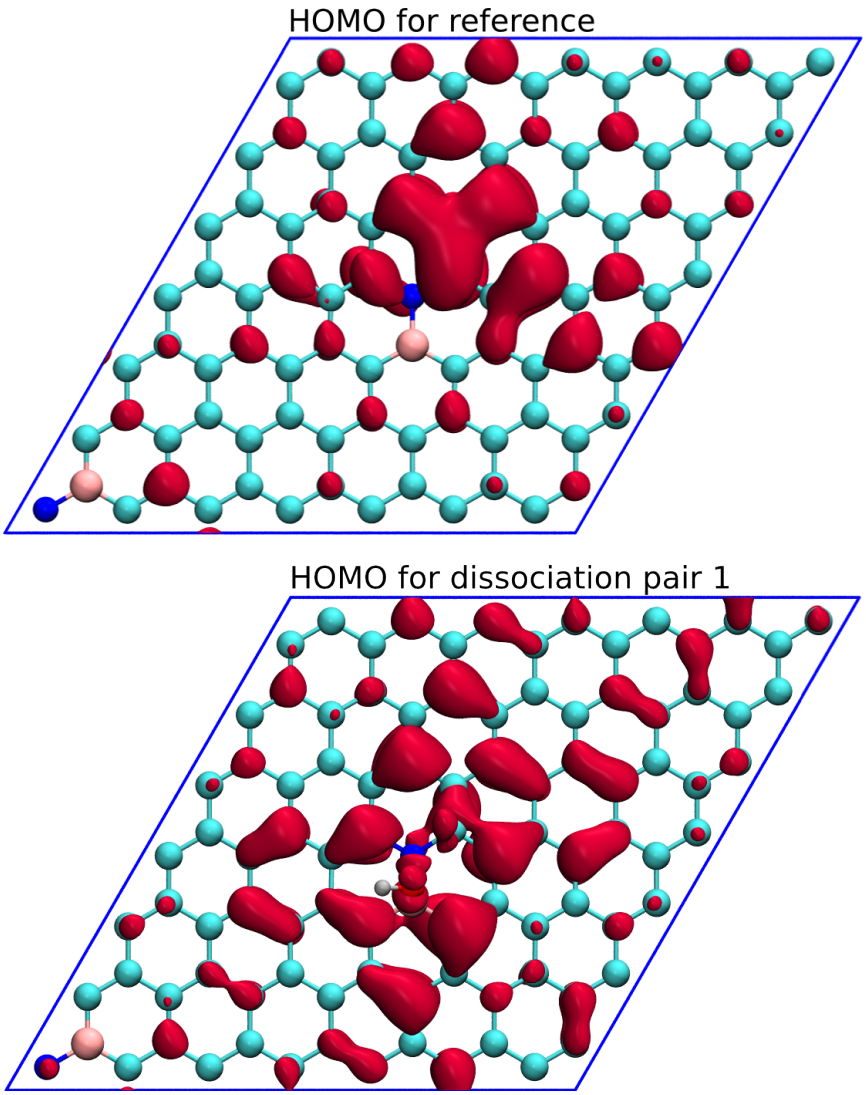

Figure 8.3: Charge density plot of the Kohn-Sham highest occupied molecular orbital (HOMO) for the initial states in BN pair 1 scheme. An isovalue of 0.005 eV/Å^3 was used for the figures.

paths involving mesomerically active sites compared to passive sites. The MAE for mesomerically passive sites is less than 30 meV for the BN pair and B wander schemes, and thus even lower than the gold standard of accuracy in chemistry (1 kcal mol^{-1}). Interestingly, the errors are overall larger for N wander (see in Fig. 8.4(b) the comparison with B wander) and the impact of classifying combined HOMO charges of more than 0.05 e as mesomerically active is less pronounced in the correlation coefficients R^2 and ρ, for N wander. However, the errors still benefit from an order of magnitude reduction in size. The larger errors for N wander may seem conflicting with the excellent ρ coefficient for both mesomerically active (0.92) and passive (0.89) sites. However, it has been shown previously that predictions for right-to-left transformations in the periodic table are not equivalent to the reverse and entail larger errors [310]. Encouragingly, the strong correlation is maintained despite the larger shift from the calculated energies.

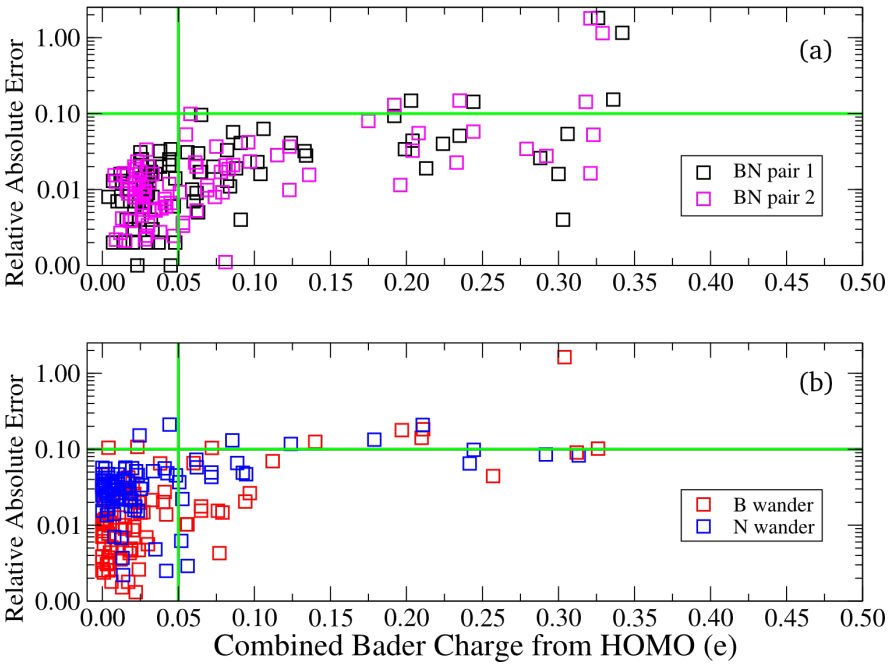

Figure 8.4: The relative absolute error and combined HOMO charge is shown for each path. Top panel includes BN pair 1 and 2, whilst lower panel includes B wander and N wander. Green lines indicate the threshold values used to distinguish between mesomerically active and passive sites.

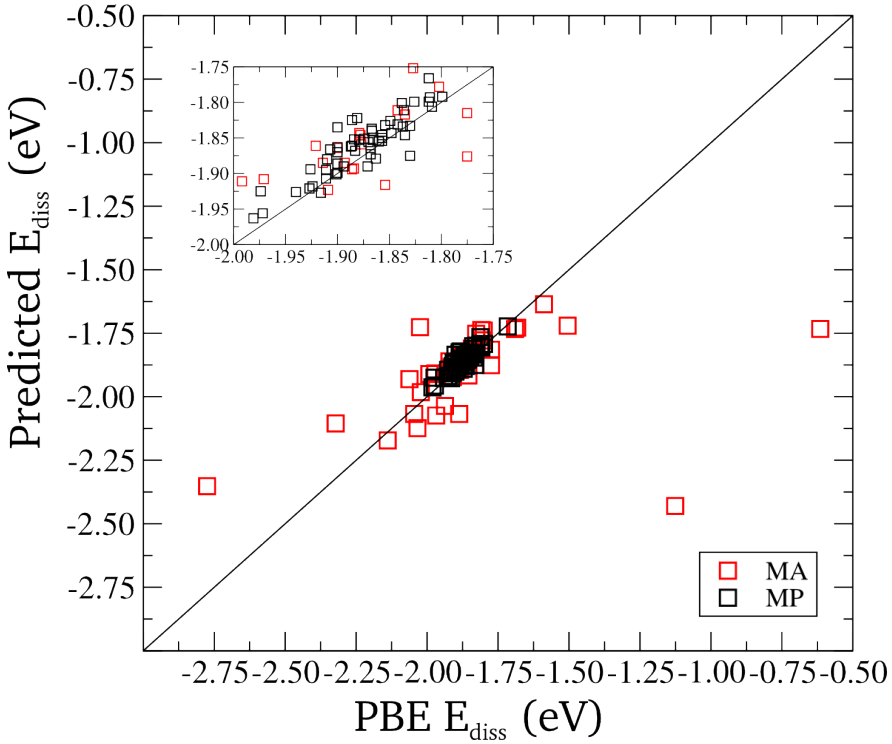

Figure 8.5: Calculated PBE dissociative adsorption energies of water for paths in the BN pair 1 scheme against the alchemically predicted energies. Black squares correspond to mesomerically passive sites in the initial state, and red squares correspond to mesomerically active sites in the initial state.

8.4 Discussion

Partitioning the HOMO charge density for the initial states is shown to be an effective means of filtering out particularly weak predictions. At least two important questions need to be addressed with regards to this process and we also draw some chemical insights later in the discussion.

First, how should the initial threshold value for the HOMO charge density be chosen without performing further calculations? This is somewhat of an arbitrary choice but some guidelines can be used. For example, the threshold charge can be chosen by looking at the distribution of HOMO charges for paths and considering the point at which the combined charge begins to deviate from the majority of paths. For example in Fig. 8.4, the majority of combined charges are below 0.15 e. Although this is a higher threshold than what has been chosen for Table 8.1, it would still correspond to small errors according to Fig. 8.5.

Second, can the filtered mesomerically active paths be salvaged? In the current context that would be very useful because the highest dissociation energies arise from doping at me-

Table 8.1: Statistical analysis of data from four schemes and resolved for mesomaerically active and passive classification using a threshold HOMO charge of 0.05 e. R^2 coefficient, Spearman's rank correlation coefficient (ρ), mean absolute error (MAE) in eV, and root mean square error (RMSE) in eV are listed. Inset shows a zoomed-in region for clarity.

	R^2	ρ	MAE (eV)	RMSE (eV)
BN pair 1				
total	0.14		0.07	0.19
MA	0.13	0.68	0.14	0.30
MP	0.81	0.85	0.02	0.03
BN pair 2				
total	0.17		0.06	0.19
MA	0.15	0.71	0.12	0.28
MP	0.89	0.89	0.02	0.02
B wander				
total	0.27		0.06	0.16
MA	0.05	0.45	0.18	0.33
MP	0.90	0.91	0.03	0.04
N wander				
total	0.49		0.09	0.18
MA	0.53	0.92	0.19	0.34
MP	0.67	0.89	0.06	0.08

somerically active sites (see Fig. 8.5). Two particular solutions can be utilised here. One is to simply perform DFT calculations for the mesomerically active paths - this is somewhat unimaginative but straightforward. The second possibility is to go beyond the first order alchemical derivative, and improve the prediction by including second order terms. Recently Chang *et al.* compared three approximations to the second order term namely, the coupled perturbed (CP) approach, the independent particle approximation (IPA) and the finite difference method, for the density response to alchemical coupling [310]. The CP approach is shown therein to be superior to IPA for horizontal isoelectronic transformations in many electron systems. However, all higher order alchemical derivative terms require additional computational cost, and hence it could be a matter of implementation of second order derivative approaches to see if they would be more efficient than to directly calculate the DFT energies for such paths.

Beyond the implications of efficiently screening isoelectronically doped configurations of graphene, one can take a closer look at the resulting favourable dissociative adsorption config-

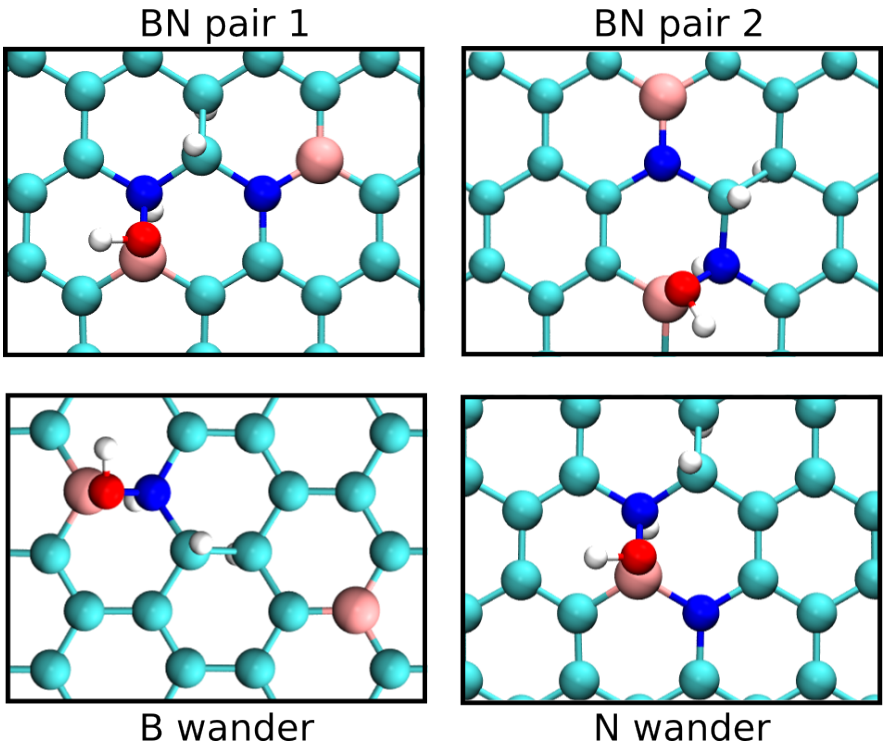

Figure 8.6: Configurations of dissociative adsorption from alchemical screening.

urations to gain some insight. Fig. 8.6 shows the configuration with the most favourable water adsorption energies obtained for each scheme, which range from −2.1 to −2.8 eV. Despite different starting sublattices for BN pair 1 and BN pair 2, the same configuration is identified as the most favourable for water dissociation. In this state, the hydrogen atom of water adsorbs on a carbon atom between two nitrogen atoms. This is not surprising given that the central carbon atom becomes more positive as a result of the electronegative nitrogen atoms, and is stabilised by bonding to a hydrogen atom. This is in agreement with the patterns identified in the previous chapter. Similar reasoning can explain the configuration found for N wander wherein, the boron atom is between two nitrogen atoms and thus forms a stronger bond with the OH fragment of water. More interestingly, the favourable configuration from B wander is less intuitive (see Fig. 8.6) and highlights the usefulness of screening through various topological possibilities. This particular configuration corresponds to an adsorption energy of −2.12 eV.

8.5 Conclusion

It has been shown that predictions using alchemical derivatives in DFT can be used to explore the impact of isoelectronic doping in activated graphene on the dissociative adsorption of water. Doping at different sites around the adsorption site in the substrate leads to a spread of $\sim$2 eV in the adsorption energy. Importantly, it has been demonstrated that poor predictions can be filtered *a priori* by identifying mesomerically active and passive sites using a Bader analysis of the HOMO in the initial state. In this way, one can efficiently screen through the majority of configurations with very good accuracy - for instance in this study the MAE is less than 30 meV in the dissociative adsorption energy of water.

Chapter 9

Conclusions and Outlook

Let us summarise the findings in this thesis and consider the implications. Chapters 3-6 have focused primarily on establishing accurate benchmark adsorption energies. In Chapter 3, the interaction energy and configuration of a water monomer and BN doped benzene (1,2-azaborine) was studied using a range of *ab initio* methods. In particular, ΔCCSD(T) was used to establish accurate interaction energies for three distinct configurations, with differences in energy ranging by less than 20 meV. DMC was found to agree well with ΔCCSD(T), whilst MP2 slightly overbound. Importantly, all of the exact exchange methods predicted the same energy ordering of the configurations. In contrast, almost all of the DFT xc functionals we considered, with and without dispersion, predict the wrong order. This study highlights the importance of the delocalisation error for even small, weakly interacting systems. The wrong energy ordering of weakly interacting molecular systems, given by a number of widely used xc functionals, has implications for the crystal structure prediction of organic polymorphs. Indeed, a very high fraction of exact exchange was required in this study to achieve the correct ordering. As such, it is difficult to prescribe a standard hybrid functional since the amount of exact exchange is likely to be system dependent. However, it is worth remembering that some xc functionals within the vdW-DFs predicted interaction energies in close agreement with benchmarks, despite the wrong ordering.

With the promising results from DMC in Chapter 3, DMC was used in chapter 4 to establish the interaction energy of a water molecule on a (4×4) unit cell of h-BN. This can be considered as a fairly large system for DMC, and certainly for any other benchmark method. The interaction of water is predicted to be stronger above a nitrogen site in the h-BN surface

(-84 ± 5 meV), than at a boron site (-63 ± 5 meV). Since the computation of these interaction energy curves, force field parameters have been fit to our values for the interaction potential of water with h-BN [71]. Promising results have been obtained via the DMC fitted force fields, predicting water contact angles in far better agreement with experiment than other conventional force fields [71]. Thus, demonstrating that benchmark DMC energies can serve not only as validation for the development of computational methods, but also as a reliable basis to build a model on.

However, we are reminded in Chapter 5, that even so-called benchmark calculations have their limitations. Starting with molecular BN substrates and water, interaction energy curves from DMC, RPA, ΔCCSD(T), and MP2 were compared. Excellent agreement is achieved amongst the methods, although the RPA underbinds. This is however, alleviated by the inclusion of single excitations. In addition, a number of dispersion inclusive functionals were found to predict the interaction energy of water with borazine accurately - similarly to what was seen in Chapter 3. However, for the larger molecule boronene, the predictions from DFT xc functionals are disappointing. This is despite the similarity between boronene and borazine interacting with water. Such a peculiar result demonstrates once again, the inconsistent performance of xc functionals. This is particularly relevant for studies that use molecules of increasing size, to extrapolate to an extended surface. In such schemes, it is not given that one can rely on xc functionals to give accurate predictions. Instead, embedding schemes that employ different levels of theory such as CCSD(T) alongside DFT could be more reliable [315–317].

Taking the water/h-BN system further, we investigated the effect of long-range correlation that is not captured within a given unit cell size. With the help of the RPA and LMP2 results provided by collaborators, much larger unit cells with almost 100 atoms were modelled. An additional 20 meV is gained in the water/h-BN interaction by considering larger unit cells. This is clearly a sizeable proportion of the interaction energy predicted initially for a (4×4) unit cell of h-BN. Moreover, the scaling of the interaction energy with system size is not reproduced by LMP2, due to the lack of higher order excitations within this method. Interestingly, the MBD correction in DFT calculations does reproduce the correct scaling as predicted by the RPA. This finding could be very useful for future DMC calculations, where large unit cells might be too expensive, but we seek a reliable estimate of the finite size effect.

It is also interesting to note that we see such prominent long-range correlation for h-BN that is a 2D insulator. It suggests that a semi-metal like graphene requires even larger unit cells to capture the long-range interactions. Indeed, to accurately inform experimentalists, it is important to establish the extent of these size effects.

Although long-range correlation has been the focus of many studies on low dimensional materials, in Chapter 6 we saw that medium-range correlation is also a big challenge. Specifically, benchmark DMC interaction energies were computed for water and molecular hydrogen, inside and outside of a zigzag CNT. These are the first reference interaction energies for these molecules with a periodic CNT. The interaction of molecular hydrogen is found to be approximately half of that of water. A range of xc functionals is found to predict the interaction energy of either molecule outside of the CNT relatively well. Strikingly, the predictions from vdW inclusive functionals are particularly bad when the molecules are placed inside the CNT. In contrast, the vdW corrected xc functionals perform much better. This is somewhat unexpected as vdW-DFs are thought to be appropriate for vdW dominated interactions. By examining the interactions with different sized CNTs, the medium-range correlation appears to be a particular problem for vdW-DFs. This can be partly explained by the development of these functionals being focused on reproducing interaction energies for small molecules mostly. As a result, for systems where there is a lot of electron correlation in the medium-range, current vdW-DFs might not provide accurate predictions. In vdW corrected functionals, the medium-range correlation can be expected to depend on the damping function used.

The study of physisorption interactions in this thesis might leave the reader thinking that xc functionals are a long way from providing us with accurate predictions for vdW materials. In fact, some xc functionals are found to work exceedingly well depending on the property of interest and the system. Of course, in performing *ab initio* simulations we desire a consistent and reliable method. In the absence of the exact xc functional however, it is likely that we must always choose our xc functional carefully and consider the application. Fortunately, the many successful years of applying DFT to various problems can provide us with some insight when choosing xc functionals. As we look to model more exotic and novel materials however, reference information from DMC, RPA based methods, and embedded quantum chemical calculations, become invaluable. Moreover, the rise of machine learning techniques suggests that accurate reference data could be needed for reliable training sets. With this, we may see

fast and accurate potentials be designed in the near future.

Finally let us recall the findings in Chapters 7 and 8 on the chemisorption of molecules on 2D surfaces. In Chapter 7, conventional DFT with the PBE xc functional was used to study the reactivity of graphene and h-BN based substrates. Graphene was doped with BN, and h-BN was doped with carbon atoms to compare the reactivity on pristine and doped substrates. This isoelectronic doping in the surfaces was found to make the dissociative adsorption energy of water more favourable by more than 0.5 eV. In addition, we considered the hydrogenation or protonation of the surfaces prior to water adsorption. It was found to makes all surfaces significantly better at dissociatively adsorbing water. In addition to water, we also considered the adsorption of molecular hydrogen, methane, and methanol. Unlike typical metal catalysts, these 2D surfaces were found to selectively adsorb these molecules. Specifically, the adsorption of polar molecules is promoted by BN doping in graphene, and non-polar molecules adsorb more favourably on C doped h-BN. These simple calculations neglect energy barriers, the effect of a substrate under the materials, and no solvent is modelled. Nonetheless, they point towards the use of these 2D materials as selective catalytic substrates.

Considering the role of isoelectronic doping further, the dissociative adsorption energy of water on BN doped graphene was used in Chapter 8. Here, alchemical derivatives have been used as part of a screening method to explore the impact of BN doping in the graphene surface, on the adsorption of water. The predictions from this scheme were compared with explicit DFT calculations. At most doping sites in the surface, the predictions were very good (within a few percent of the DFT adsorption energies). More notably, we were able to use the highest occupied molecular orbital of the initial system as an indicator for the quality of predictions. This filtering process greatly reduces the number of bad predictions and provides an effective way to identify potential outliers.

On the whole, graphene and h-BN related materials have been fascinating to model. Various aspects of these materials have been outside the scope of this thesis, but are nonetheless very important. These other factors include the intrinsic rippling of 2D materials, the role of substrates that support these materials, the presence of structural defects, and the effect of solvents. Whilst the pristine materials may have great potential (that is yet to be industrially realised), the findings here suggest that the doping and tuning of these 2D materials open up numerous avenues for some exciting surface chemistry.

Bibliography

[1] G. A. Somorjai and Y. Li, Proc. Natl. Acad. Sci. **108**, 917 (2011).

[2] E. N. Wang and R. Karnik, Nature Nanotech. **7**, 552 (2012).

[3] W. Lei, D. Portehault, D. Liu, S. Qin, and Y. Chen, Nat. Commun. **4**, 1777 (2013).

[4] M. Yusuf, F. Elfghi, S. A. Zaidi, E. Abdullah, and M. A. Khan, RSC Advances **5**, 50392 (2015).

[5] R. Raccichini, A. Varzi, S. Passerini, and B. Scrosati, Nat. Mater. **14**, 271 (2015).

[6] B. B. Sales, M. Saakes, J. W. Post, C. J. N. Buisman, P. M. Biesheuvel, and H. V. M. Hamelers, Environ. Sci. Technol. **44**, 5661 (2010).

[7] P. Dhiman, F. Yavari, X. Mi, H. Gullapalli, Y. Shi, P. M. Ajayan, and N. Koratkar, Nano Lett. **11**, 3123 (2011).

[8] J. Yin, Z. Zhang, X. Li, J. Zhou, and W. Guo, Nano Lett. **12**, 1736 (2012).

[9] J. Yin, X. Li, J. Yu, Z. Zhang, J. Zhou, and W. Guo, Nature Nanotech. **9**, 378 (2014).

[10] A. Siria, P. Poncharal, A.-L. Biance, R. Fulcrand, X. Blase, S. T. Purcell, and L. Bocquet, Nature **494**, 455 (2013).

[11] X. Li, J. Zhao, and J. Yang, Sci. Rep. **3**, 1 (2013).

[12] Y. Sun, Q. Wu, and G. Shi, Ener. Environ. Sci. **4**, 1113 (2011).

[13] Q. Li, B. Guo, J. Yu, J. Ran, B. Zhang, H. Yan, and J. R. Gong, J. Am. Chem. Soc. **133**, 10878 (2011).

[14] F. Jamieson, Transl. Mater. Res. **1**, 020204 (2014).

[15] A. K. Geim, Science **324**, 1530 (2009).

[16] G. R. Bhimanapati, Z. Lin, V. Meunier, Y. Jung, J. Cha, S. Das, D. Xiao, Y. Son, M. S. Strano, V. R. Cooper, *et al.*, ACS Nano **9**, 11509 (2015).

[17] V. V. Gobre and A. Tkatchenko, Nature Commun. **4**, 2341 (2013).

[18] L. Ci, L. Song, C. Jin, D. Jariwala, D. Wu, Y. Li, A. Srivastava, Z. Wang, K. Storr, L. Balicas, *et al.*, Nat. Mater. **9**, 430 (2010).

[19] Z. Liu, L. Ma, G. Shi, W. Zhou, Y. Gong, S. Lei, X. Yang, J. Zhang, J. Yu, K. P. Hackenberg, *et al.*, Nature Nanotech. **8**, 119 (2013).

[20] G. A. Somorjai and Y. Li, Top. Catal. **53**, 311 (2010).

[21] C. T. Campbell and J. R. V. Sellers, J. Am. Chem. Soc. **134**, 18109 (2012).

[22] C. T. Campbell and J. R. Sellers, Chem. Rev. **113**, 4106 (2013).

[23] W. Brown, R. Kose, and D. King, Chem. Rev. **98**, 797 (1998).

[24] J. Wellendorff, T. L. Silbaugh, D. Garcia-Pintos, J. K. Nørskov, T. Bligaard, F. Studt, and C. T. Campbell, Surf. Sci. **640**, 36 (2015).

[25] P. Hohenberg and W. Kohn, Phys. Rev. **136**, B864 (1964).

[26] W. Kohn and L. J. Sham, Phys. Rev. **140**, A1133 (1965).

[27] V. I. Anisimov, J. Zaanen, and O. K. Andersen, Phys. Rev. B **44**, 943 (1991).

[28] F. Aryasetiawan, K. Karlsson, O. Jepsen, and U. Schönberger, Phys. Rev. B **74**, 125106 (2006).

[29] Editorial, Nat. Mater. **15**, 365 (2016).

[30] S. Curtarolo, G. L. Hart, M. B. Nardelli, N. Mingo, S. Sanvito, and O. Levy, Nat. Mater. **12**, 191 (2013).

[31] J. Greeley, T. F. Jaramillo, J. Bonde, I. Chorkendorff, and J. K. Nørskov, Nat. Mater. **5**, 909 (2006).

[32] M. Dion, H. Rydberg, E. Schröder, D. C. Langreth, and B. I. Lundqvist, Phys. Rev. Lett. **92**, 246401 (2004).

[33] K. Lee, É. D. Murray, L. Kong, B. I. Lundqvist, and D. C. Langreth, Phys. Rev. B **82**, 081101 (2010).

[34] S. Grimme, S. Ehrlich, and L. Goerigk, J. Comp. Chem. **32**, 1456 (2011).

[35] S. Grimme, J. Antony, S. Ehrlich, and H. Krieg, J. Chem. Phys. **132**, 154104 (2010).

[36] J. Klimeš, D. R. Bowler, and A. Michaelides, Phys. Rev. B **83**, 195131 (2011).

[37] J. Klimeš, D. R. Bowler, and A. Michaelides, J. Phys.: Condens. Matter **22**, 022201 (2010).

[38] A. Tkatchenko and M. Scheffler, Phys. Rev. Lett. **102**, 073005 (2009).

[39] A. Tkatchenko, R. A. Di Stasio, R. Car, and M. Scheffler, Phys. Rev. Lett. **108**, 236402 (2012).

[40] A. Ambrosetti, A. M. Reilly, R. A. DiStasio, and A. Tkatchenko, J. Chem. Phys. **140**, 018A508 (2014).

[41] R. Sabatini, T. Gorni, and S. de Gironcoli, Phys. Rev. B **87**, 041108 (2013).

[42] O. A. Vydrov and T. Van Voorhis, J. Chem. Phys. **133**, 244103 (2010).

[43] J. Klimeš and A. Michaelides, J. Chem. Phys. **137**, 120901 (2012).

[44] S. Grimme, WIREs Comput. Mol. Sci. **1**, 211 (2011).

[45] S. Grimme, A. Hansen, J. G. Brandenburg, and C. Bannwarth, Chem. Rev. **116**, 5105 (2016).

[46] J. F. Dobson and T. Gould, J. Phys.: Condens. Matter **24**, 073201 (2012).

[47] K. Berland, V. R. Cooper, K. Lee, E. Schröder, T. Thonhauser, P. Hyldgaard, and B. I. Lundqvist, Rep. Prog. Phys. **78**, 066501 (2015).

[48] E. Whalley, J. Chem. Phys. **81**, 4087 (1984).

[49] E. D. Murray and G. Galli, Phys. Rev. Lett. **108**, 105502 (2012).

[50] B. Santra, J. Klimeš, D. Alfè, A. Tkatchenko, B. Slater, A. Michaelides, R. Car, and M. Scheffler, Phys. Rev. Lett. **107**, 185701 (2011).

[51] B. Santra, J. Klimeš, A. Tkatchenko, D. Alfè, B. Slater, A. Michaelides, R. Car, and M. Scheffler, J. Chem. Phys. **139**, 154702 (2013).

[52] M. J. Gillan, D. Alfè, P. J. Bygrave, C. R. Taylor, and F. R. Manby, J. Chem. Phys. **139**, 114101 (2013).

[53] B. Slater and D. Quigley, Nat. Mater. **13**, 670 (2014).

[54] B. Santra, A. Michaelides, M. Fuchs, A. Tkatchenko, C. Filippi, and M. Scheffler, J. Chem. Phys. **129**, 194111 (2008).

[55] J. M. Pedulla, K. Kim, and K. D. Jordan, Chem. Phys. Lett. **291**, 78 (1998).

[56] S. L. Price, Acc. Chem. Res. **42**, 117 (2009).

[57] S. L. Price, Chem. Soc. Rev. **43**, 2098 (2014).

[58] S. N. Timasheff, Annu. Rev. Biophys. Biomol. Struct. **22**, 67 (1993).

[59] L. Schimka, J. Harl, A. Stroppa, A. Grüneis, M. Marsman, F. Mittendorfer, and G. Kresse, Nat. Mater. **9**, 741 (2010).

[60] J. Harl and G. Kresse, Phys. Rev. Lett. **103**, 056401 (2009).

[61] J. Harl, L. Schimka, and G. Kresse, Physical Review B **81**, 115126 (2010).

[62] S. J. Binnie, *Ab initio surface energetics: beyond chemical accuracy*, Ph.D. thesis, UCL (University College London) (2011).

[63] J. Ma, A. Michaelides, D. Alfè, L. Schimka, G. Kresse, and E. Wang, Phys. Rev. B **84**, 033402 (2011).

[64] E. Voloshina, D. Usvyat, M. Schütz, Y. Dedkov, and B. Paulus, Phys. Chem. Chem. Phys. **13**, 12041 (2011).

[65] Y. S. Al-Hamdani, M. Ma, D. Alfè, O. A. von Lilienfeld, and A. Michaelides, J. Chem. Phys. **142**, 181101 (2015).

[66] P. Ganesh, J. Kim, C. Park, M. Yoon, F. A. Reboredo, and P. R. C. Kent, J. Chem. Theory Comput. **10**, 5318 (2014).

[67] M. C. Gordillo, Phys. Rev. B **88**, 041406 (2013).

[68] S. Lei, B. Paulus, S. Li, and B. Schmidt, J. Comput. Chem. **37**, 1313 (2016).

[69] J. Ma, A. Michaelides, and D. Alfè, J. Chem. Phys. **134**, 134701 (2011).

[70] Y. Wu, L. K. Wagner, and N. R. Aluru, J. Chem. Phys. **142**, 234702 (2015).

[71] Y. Wu, L. K. Wagner, and N. R. Aluru, J. Chem. Phys. **144**, 164118 (2016).

[72] D. R. Hartree, in *Mathematical Proceedings of the Cambridge Philosophical Society*, Vol. 24 (Cambridge Univ Press, 1928) pp. 89–110.

[73] V. Fock, Phys. Rev. **35**, 210 (1930).

[74] L. H. Thomas, in *Mathematical Proceedings of the Cambridge Philosophical Society*, Vol. 23 (Cambridge Univ Press, 1927) pp. 542–548.

[75] E. Fermi, Rend. Accad. Naz. Lincei **6**, 32 (1927).

[76] M. Born and R. Oppenheimer, Ann. Phys **84**, 457 (1927).

[77] M. Ceriotti, W. Fang, P. G. Kusalik, R. H. McKenzie, A. Michaelides, M. A. Morales, and T. E. Markland, Chem. Rev. **116**, 7529 (2016).

[78] S. Pisana, M. Lazzeri, C. Casiraghi, K. S. Novoselov, A. K. Gei m, A. C. Ferrari, and F. Mauri, Nat. Mater. **6**, 198 (2007).

[79] G. H. Booth, A. J. Thom, and A. Alavi, J. Chem. Phys. **131**, 054106 (2009).

[80] D. Cleland, G. H. Booth, C. Overy, and A. Alavi, J. Chem. Theory Comput. **8**, 4138 (2012).

[81] R. E. Thomas, G. H. Booth, and A. Alavi, Phys. Rev. Lett. **114**, 033001 (2015).

[82] P. Jurečka and P. Hobza, Chem. Phys. Lett. **365**, 89 (2002).

[83] P. Hobza and J. Šponer, J. Am. Chem. Soc. **124**, 11802 (2002).

[84] I. Dąbkowska, P. Jurečka, and P. Hobza, J. Chem. Phys. **122**, 204322 (2005).

[85] A. Grüneis, M. Marsman, and G. Kresse, J. Chem. Phys. **133**, 074107 (2010).

[86] H.-J. Werner, F. R. Manby, and P. J. Knowles, J. Chem. Phys. **118**, 8149 (2003).

[87] H.-J. Werner and F. R. Manby, J. Chem. Phys. **124**, 054114 (2006).

[88] M. Schütz, G. Hetzer, and H.-J. Werner, J. Chem. Phys. **111**, 5691 (1999).

[89] C. Hampel and H.-J. Werner, J. Chem. Phys. **104**, 6286 (1996).

[90] C. Riplinger, B. Sandhoefer, A. Hansen, and F. Neese, J. Chem. Phys. **139**, 134101 (2013).

[91] C. Riplinger and F. Neese, J. Chem. Phys. **138**, 034106 (2013).

[92] F. R. Manby, *Accurate Condensed-Phase Quantum Chemistry* (CRC Press, 2010).

[93] R. A. Mata and H.-J. Werner, Mol. Phys. **105**, 2753 (2007).

[94] J. W. Boughton and P. Pulay, J. Comp. Chem. **14**, 736 (1993).

[95] T. B. Adler and H.-J. Werner, J. Chem. Phys. **130**, 241101 (2009).

[96] D. G. Liakos, M. Sparta, M. K. Kesharwani, J. M. Martin, and F. Neese, J. Chem. Theory Comput. **11**, 1525 (2015).

[97] M. Schütz and F. R. Manby, Phys. Chem. Chem. Phys. **5**, 3349 (2003).

[98] W. Klopper, F. R. Manby, S. Ten-No, and E. F. Valeev, Int. Rev. Phys. Chem. **25**, 427 (2006).

[99] K. Burke, J. Chem. Phys. **136**, 150901 (2012).

[100] A. D. Becke, J. Chem. Phys. **140**, 18A301 (2014).

[101] D. Alfè and M. Gillan, J. Phys.: Condens. Matter **18**, L435 (2006).

[102] S. J. Binnie, E. Sola, D. Alfè, and M. J. Gillan, Mol. Simulat. **35**, 609 (2009).

[103] J. F. Dobson, K. McLennan, A. Rubio, J. Wang, T. Gould, H. M. Le, and B. P. Dinte, Aust. J. Chem. **54**, 513 (2002).

[104] A. Ambrosetti, N. Ferri, R. A. DiStasio, and A. Tkatchenko, Science **351**, 1171 (2016).

[105] A. Grüneis, M. Marsman, J. Harl, L. Schimka, and G. Kresse, J. Chem. Phys. **131**, 154115 (2009).

[106] X. Ren, P. Rinke, C. Joas, and M. Scheffler, J. Mater. Sci. **47**, 7447 (2012).

[107] J. Paier, X. Ren, P. Rinke, G. E. Scuseria, A. Grüneis, G. Kresse, and M. Scheffler, New J. Phys. **14**, 043002 (2012).

[108] V. A. Parsegian, *Van der Waals forces: a handbook for biologists, chemists, engineers, and physicists* (Cambridge University Press, 2005).

[109] P. J. Feibelman, B. Hammer, J. K. Nørskov, F. Wagner, M. Scheffler, R. Stumpf, R. Watwe, and J. Dumesic, J. Phys. Chem. B **105**, 4018 (2001).

[110] X. Ren, A. Tkatchenko, P. Rinke, and M. Scheffler, Phys. Rev. Lett. **106**, 153003 (2011).

[111] F. Furche, Phys. Rev. B **64**, 195120 (2001).

[112] M. Towler, physica status solidi (b) **243**, 2573 (2006).

[113] R. Jastrow, Phys. Rev. **98**, 1479 (1955).

[114] N. Drummond, M. Towler, and R. Needs, Phys. Rev. B **70**, 235119 (2004).

[115] T. Kato, Commun. Pure Appl. Math. **10**, 151 (1957).

[116] R. T. Pack and W. B. Brown, J. Chem. Phys. **45**, 556 (1966).

[117] N. Nemec, M. D. Towler, and R. J. Needs, J. Chem. Phys. **132**, 034111 (2010).

[118] M. Dubecký, P. Jurečka, R. Derian, P. Hobza, M. Otyepka, and L. Mitas, J. Chem. Theory Comput. **9**, 4287 (2013).

[119] V. Brázdová and D. R. Bowler, *Atomistic computer simulations: a practical guide* (John Wiley & Sons, 2013).

[120] D. G. Truhlar, Chem. Phys. Lett. **294**, 45 (1998).

[121] A. Halkier, W. Klopper, T. Helgaker, P. Jørgensen, and P. R. Taylor, J. Chem. Phys. **111**, 9157 (1999).

[122] A. Halkier, T. Helgaker, P. JÃÿrgensen, W. Klopper, H. Koch, J. Olsen, and A. K. Wilson, Chem. Phys. Lett. **286**, 243 (1998).

[123] A. Halkier, T. Helgaker, P. Jørgensen, W. Klopper, and J. Olsen, Chem. Phys. Lett. **302**, 437 (1999).

[124] D. Feller and K. A. Peterson, J. Chem. Phys. **110**, 8384 (1999).

[125] T. H. Dunning Jr, J. Chem. Phys. **90**, 1007 (1989).

[126] R. A. Kendall, T. H. Dunning Jr, and R. J. Harrison, J. Chem. Phys. **96**, 6796 (1992).

[127] D. E. Woon and T. H. Dunning Jr, J. Chem. Phys. **98**, 1358 (1993).

[128] S. F. Boys and F. d. Bernardi, Mol. Phys. **19**, 553 (1970).

[129] J. VandeVondele, U. Borstnik, and J. Hutter, J. Chem. Theory Comput. **8**, 3565 (2012).

[130] D. R. Bowler and T. Miyazaki, J. Phys.: Condens. Matter **22**, 074207 (2010).

[131] D. Bowler and T. Miyazaki, Rep. Prog. Phys. **75**, 036503 (2012).

[132] D. Alfè and M. Gillan, Phys. Rev. B **70**, 161101 (2004).

[133] S. L. Price, Acta Cryst. B **69**, 313 (2013).

[134] D. Singhal and W. Curatolo, Adv. Drug Deliv. Rev. **56**, 335 (2004).

[135] L. Ci, L. Song, C. Jin, D. Jariwala, D. Wu, Y. e. Li, A. Srivastava, Z. Wang, K. Storr, L. Balicas, *et al.*, Nat. Mater. **9**, 430 (2010).

[136] Z. Liu, L. Ma, G. Shi, W. Zhou, Y. Gong, S. Lei, X. Yang, J. Zhang, J. Yu, K. P. Hackenberg, *et al.*, Nature Nanotech. **8**, 119 (2013).

[137] Y. Zheng, Y. Jiao, L. Ge, M. Jaroniec, and S. Z. Qiao, Angew. Chem. **125**, 3192 (2013).

[138] Y. Ding, M. Iannuzzi, and J. Hutter, J. Phys. Chem. C **115**, 13685 (2011).

[139] L. B. Boinovich, A. M. Emelyanenko, A. S. Pashinin, C. H. Lee, J. Drelich, and Y. K. Yap, Langmuir **28**, 1206 (2012).

[140] M. C. Gordillo and J. Martí, Phys. Rev. E **84**, 011602 (2011).

[141] F. Taherian, V. Marcon, N. F. A. van der Vegt, and F. Leroy, Langmuir **29**, 1457 (2013).

[142] J. Shim, C. H. Lui, T. Y. Ko, Y.-J. Yu, P. Kim, T. F. Heinz, and S. Ryu, Nano Lett. **12**, 648 (2012).

[143] J. Rafiee, X. Mi, H. Gullapalli, A. V. Thomas, F. Yavari, Y. Shi, P. M. Ajayan, and N. A. Koratkar, Nat. Mater. **11**, 217 (2012).

[144] Z. Li, Y. Wang, A. Kozbial, G. Shenoy, F. Zhou, R. McGinley, P. Ireland, B. Morganstein, A. Kunkel, S. P. Surwade, *et al.*, Nat. Mater. **12**, 925 (2013).

[145] G. R. Jenness, O. Karalti, and K. D. Jordan, Phys. Chem. Chem. Phys. **12**, 6375 (2010).

[146] I. Hamada, Phys. Rev. B **86**, 195436 (2012).

[147] M. Rubeš, P. Nachtigall, J. Vondrášek, and O. Bludský, J. Phys. Chem. C **113**, 8412 (2009).

[148] D. Feller and K. D. Jordan, J. Phys. Chem. A **104**, 9971 (2000).

[149] S. Xu, S. Irle, D. G. Musaev, and M. C. Lin, J. Phys. Chem. A **109**, 9563 (2005).

[150] I. W. Sudiarta and D. J. W. Geldart, J. Phys. Chem. A **110**, 10501 (2006).

[151] Y. Zhao, O. Tishchenko, and D. G. Truhlar, J. Phys. Chem. B **109**, 19046 (2005).

[152] S. K. Min, E. C. Lee, H. M. Lee, D. Y. Kim, D. Kim, and K. S. Kim, J. Comput. Chem. **29**, 1208 (2008).

[153] D. Feller, J. Phys. Chem. A **103**, 7558 (1999).

[154] J. Ma, D. Alfè, A. Michaelides, and E. Wang, J. Chem. Phys. **130**, 154303 (2009).

[155] J. Wu, H. Yan, H. Chen, G. Dai, and A. Zhong, Comput. Theor. Chem. **984**, 51 (2012).

[156] V. Marcon, O. A. von Lilienfeld, and D. Andrienko, J. Chem. Phys. **127**, 064305 (2007).

[157] T. Björkman, A. Gulans, A. V. Krasheninnikov, and R. M. Nieminen, Phys. Rev. Lett. **108**, 235502 (2012).

[158] T. Björkman, J. Chem. Phys. **141**, 074708 (2014).

[159] J. Antony and S. Grimme, Phys. Chem. Chem. Phys. **8**, 5287 (2006).

[160] G. Graziano, J. Klimeš, F. Fernandez-Alonso, and A. Michaelides, J. Phys. Condens. Matter **24**, 424216 (2012).

[161] J. Carrasco, J. Klimeš, and A. Michaelides, J. Chem. Phys. **138**, 024708 (2013).

[162] T. Thonhauser, A. Puzder, and D. C. Langreth, J. Chem. Phys. **124**, 164106 (2006).

[163] Y. Kanai and J. C. Grossman, Phys. Rev. A **80**, 032504 (2009).

[164] B. Santra, A. Michaelides, and M. Scheffler, J. Chem. Phys. **131**, 124509 (2009).

[165] A. J. Cohen, P. Mori-Sánchez, and W. Yang, Science **321**, 792 (2008).

[166] K. Burke, J. Chem. Phys. **136**, 150901 (2012).

[167] L. A. Burns, M. S. Marshall, and C. D. Sherrill, J. Chem. Theory Comput. **10**, 49 (2014).

[168] M. J. Frisch, G. W. Trucks, H. B. Schlegel, G. E. Scuseria, M. A. Robb, J. R. Cheeseman, J. A. Montgomery, Jr., T. Vreven, K. N. Kudin, J. C. Burant, and J. M. M. *et al.*, "Gaussian 03, Revision C.02," (2004), Gaussian, Inc., Wallingford, CT, 2004.

[169] P. Giannozzi, S. Baroni, N. Bonini, M. Calandra, R. Car, C. Cavazzoni, D. Ceresoli, *et al.*, J. Phys.: Condens. Matter **21**, 395502 (2009).

[170] J. R. Trail and R. J. Needs, J. Chem. Phys. **122**, 174109 (2005).

[171] J. R. Trail and R. J. Needs, J. Chem. Phys. **122**, 014112 (2005).

[172] J. P. Perdew and A. Zunger, Phys. Rev. B **23**, 5048 (1981).

[173] J. P. Perdew, K. Burke, and M. Ernzerhof, Phys. Rev. Lett. **77**, 3865 (1996).

[174] D. Alfè and M. J. Gillan, Phys. Rev. B **70** (2004).

[175] R. J. Needs, M. D. Towler, N. D. Drummond, and P. L. Ríos, "Casino version 2.13," (2010).

[176] L. Mitas, E. L. Shirley, and D. Ceperley, J. Chem. Phys. **95** (1991).

[177] G. Kresse and J. Hafner, Phys. Rev. B **47**, 558 (1993).

[178] G. Kresse and J. Hafner, Phys. Rev. B **49**, 14251 (1994).

[179] G. Kresse and J. Furthmüller, Comp. Mater. Sci. **6**, 15 (1996).

[180] G. Kresse and J. Furthmüller, Phys. Rev. B **54**, 11169 (1996).

[181] P. E. Blöchl, Phys. Rev. B **50**, 17953 (1994).

[182] G. Kresse and D. Joubert, Phys. Rev. B **59**, 1758 (1999).

[183] C. Adamo and V. Barone, J. Chem. Phys. **110**, 6158 (1999).

[184] J. P. Perdew, M. Ernzerhof, and K. Burke, J. Chem. Phys. **105**, 9982 (1996).

[185] A. D. Becke, J. Chem. Phys. **98**, 5648 (1993).

[186] C. Lee, W. Yang, and R. G. Parr, Phys. Rev. B **37**, 785 (1988).

[187] S. H. Vosko, L. Wilk, and M. Nusair, Can. J. Phys. **58**, 1200 (1980).

[188] P. J. Stephens, F. J. Devlin, C. F. Chabalowski, and M. J. Frisch, J. Phys. Chem. **98**, 11623 (1994).

[189] S. Grimme, J. Comp. Chem. **27**, 1787 (2006).

[190] C.-S. Liu, G. Pilania, C. Wang, and R. Ramprasad, J. Phys. Chem. A **116**, 9347 (2012).

[191] T. Bučko, J. Hafner, S. Lebègue, and J. G. Angyán, J. Phys. Chem. A **114**, 11814 (2010).

[192] D. Tunega, T. BuÄĎko, and A. Zaoui, J. Chem. Phys. **137**, 114105 (2012).

[193] A. Benali, L. Shulenburger, N. A. Romero, J. Kim, and O. A. von Lilienfeld, J. Chem. Theory Comput. **10**, 3417 (2014).

[194] S. Nolan, M. Gillan, D. Alfè, N. Allan, and F. Manby, Phys. Rev. B **80**, 165109 (2009).

[195] O. A. von Lilienfeld and A. Tkatchenko, J. Chem. Phys. **132**, 234109 (2010).

[196] Y. Wang, S. de Gironcoli, N. S. Hush, and J. R. Reimers, J. Am. Chem. Soc. **129**, 10402 (2007).

[197] C. Di Valentin, G. Pacchioni, and A. Selloni, Phys. Rev. Lett. **97**, 166803 (2006).

[198] A. Pakdel, Y. Bando, and D. Golberg, Chem. Soc. Rev. **43**, 934 (2014).

[199] A. Pakdel, C. Zhi, Y. Bando, T. Nakayama, and D. Golberg, ACS Nano **5**, 6507 (2011).

[200] G. Tocci, L. Joly, and A. Michaelides, Nano Lett. **14**, 6872 (2014).

[201] H. Li and X. C. Zeng, ACS Nano **6**, 2401 (2012).

[202] C. Y. Won and N. R. Aluru, J. Am. Chem. Soc. **129**, 2748 (2007).

[203] C. Won and N. Aluru, J. Phys. Chem. C **112**, 1812 (2008).

[204] M. C. Gordillo and J. Martí, Phys. Rev. E **84** (2011).

[205] R. C. Dutta, S. Khan, and J. K. Singh, Fluid Phase Equilibr. **302**, 310 (2011).

[206] C.-J. Shih, Q. H. Wang, S. Lin, K.-C. Park, Z. Jin, M. S. Strano, and D. Blankschtein, Phys. Rev. Lett. **109**, 176101 (2012).

[207] A. Hodgson and S. Haq, Surf. Sci. Rep. **64**, 381 (2009).

[208] C. T. Campbell and J. R. V. Sellers, Chem. Rev. **113**, 4106 (2013).

[209] J. Carrasco, A. Hodgson, and A. Michaelides, Nat. Mater. **11**, 667 (2012).

[210] B. Li, A. Michaelides, and M. Scheffler, Surf. Sci. **602**, L135 (2008).

[211] L. Shulenburger and T. R. Mattsson, Phys. Rev. B **88** (2013).

[212] D. Lu, Y. Li, D. Rocca, and G. Galli, Phys. Rev. Lett. **102** (2009).

[213] Y. S. Al-Hamdani, D. Alfè, O. A. von Lilienfeld, and A. Michaelides, J. Chem. Phys. **141**, 18C530 (2014).

[214] A. D. Becke, J. Chem. Phys. **84**, 4524 (1986).

[215] A. Y. Stark, T. W. Sullivan, and P. H. Niewiarowski, J. Exper. Biol. **215**, 3080 (2012).

[216] A. Y. Stark, I. Badge, N. A. Wucinich, T. W. Sullivan, P. H. Niewiarowski, and A. Dhinojwala, Proc. Nat. Ac. Sci. **110**, 6340 (2013).

[217] I. Badge, A. Y. Stark, E. L. Paoloni, P. H. Niewiarowski, and A. Dhinojwala, Sci. Rep. **4**, 6643 (2014).

[218] A. Tkatchenko, A. Ambrosetti, and R. A. DiStasio, J. Chem. Phys. **138**, 074106 (2013).

[219] I. Hamada, Phys. Rev. B **89**, 121103 (2014).

[220] J. Sun, A. Ruzsinszky, and J. P. Perdew, Phys. Rev. Lett. **115**, 036402 (2015).

[221] V. Blum, R. Gehrke, F. Hanke, P. Havu, V. Havu, X. Ren, K. Reuter, and M. Scheffler, Comp. Phys. Commun. **180**, 2175 (2009).

[222] H.-J. Werner, P. J. Knowles, G. Knizia, F. R. Manby, M. Schütz, *et al.*, "Molpro, version 2015.1, a package of ab initio programs," (2015), see http://www.molpro.net.

[223] M. Valiev, E. J. Bylaska, N. Govind, K. Kowalski, T. P. Straatsma, H. J. Van Dam, D. Wang, J. Nieplocha, E. Apra, T. L. Windus, *et al.*, Comp. Phys. Commun. **181**, 1477 (2010).

[224] M. Marsman, A. Grüneis, J. Paier, and G. Kresse, J. Chem. Phys. **130**, 184103 (2009).

[225] D. Feller, J. Comp. Chem. **17**, 1571 (1996).

[226] F. B. Van Duijneveldt, J. G. van Duijneveldt-van de Rijdt, and J. H. van Lenthe, Chem. Rev. **94**, 1873 (1994).

[227] M. Kaltak, J. Klimeš, and G. Kresse, Phys. Rev. B **90**, 054115 (2014).

[228] M. Kaltak, J. KlimesĬŇ, and G. Kresse, J. Chem. Theory Comput. **10**, 2498 (2014).

[229] J. Klimeš, M. Kaltak, E. Maggio, and G. Kresse, J. Chem. Phys. **143**, 102816 (2015).

[230] J. K. Holt, H. G. Park, Y. Wang, M. Stadermann, A. B. Artyukhin, C. P. Grigoropoulos, A. Noy, and O. Bakajin, Science **312**, 1034 (2006).

[231] K. Falk, F. Sedlmeier, L. Joly, R. R. Netz, and L. Bocquet, Nano Lett. **10**, 4067 (2010).

[232] M. Whitby, L. Cagnon, M. Thanou, and N. Quirke, Nano Lett. **8**, 2632 (2008).

[233] M. Majumder, N. Chopra, R. Andrews, and B. J. Hinds, Nature **438**, 44 (2005).

[234] M. Ma, F. Grey, L. Shen, M. Urbakh, S. Wu, J. Z. Liu, Y. Liu, and Q. Zheng, Nature Nanotech. **10**, 692 (2015).

[235] J. Su and K. Yang, ChemPhysChem **16**, 3488 (2015).

[236] E. Secchi, S. Marbach, A. Niguès, D. Stein, A. Siria, and L. Bocquet, Nature **537**, 210 (2016).

[237] M. A. Tofighy and T. Mohammadi, Desalination **258**, 182 (2010).

[238] R. Das, M. E. Ali, S. B. A. Hamid, S. Ramakrishna, and Z. Z. Chowdhury, Desalination **336**, 97 (2014).

[239] B. Lee, Y. Baek, M. Lee, D. Jeong, H. Lee, J. Yoon, and Y. Kim, Nature Commun. **6**, 7109 (2015).

[240] A. G. Klechikov, G. Mercier, P. Merino, S. Blanco, C. Merino, and A. V. Talyzin, Micropor. Mesopor. Mat. **210**, 46 (2015).

[241] C. Liu, Y. Chen, C.-Z. Wu, S.-T. Xu, and H.-M. Cheng, Carbon **48**, 452 (2010).

[242] A. Striolo, A. Michaelides, and L. Joly, Annu. Rev. Chem. Biomol. Eng. **7**, 533 (2016).

[243] E. A. Müller, Curr. Opin. Chem. Eng. **2**, 223 (2013).

[244] S. Guo, E. R. Meshot, T. Kuykendall, S. Cabrini, and F. Fornasiero, Adv. Mater. **27**, 5726 (2015).

[245] L. Bocquet and E. Charlaix, Chem. Soc. Rev. **39**, 1073 (2010).

[246] G. Hummer, J. C. Rasaiah, and J. P. Noworyta, Nature **414**, 188 (2001).

[247] M. Munz, C. E. Giusca, R. L. Myers-Ward, D. K. Gaskill, and O. Kazakova, ACS Nano **9**, 8401 (2015).

[248] D. Kim, N. Pugno, M. Buehler, and S. Ryu, Sci. Rep. **5**, 15526 (2015).

[249] J. Driskill, D. Vanzo, D. Bratko, and A. Luzar, J. Chem. Phys. **141**, 18C517 (2014).

[250] C.-J. Shih, M. S. Strano, and D. Blankschtein, Nat. Mater. **12**, 866 (2013).

[251] A. Fedorov and A. Sadreev, Europ. Phys. J. B **69**, 363 (2009).

[252] T. Werder, J. Walther, R. Jaffe, T. Halicioglu, and P. Koumoutsakos, J. Phys. Chem. B **107**, 1345 (2003).

[253] F. Leroy, S. Liu, and J. Zhang, J. Phys. Chem. C **119**, 28470 (2015).

[254] Y. Zhang and W. Yang, Phys. Rev. Lett. **80**, 890 (1998).

[255] A. D. Becke, Phys. Rev. A **38**, 3098 (1988).

[256] J. Zhao, A. Buldum, J. Han, and J. P. Lu, Nanotechnology **13**, 195 (2002).

[257] D. Sung, S. Hong, Y.-H. Kim, N. Park, S. Kim, S. L. Maeng, and K.-C. Kim, App. Phys. Lett. **89**, 243110 (2006).

[258] B. Agrawal, V. Singh, A. Pathak, and R. Srivastava, Phys. Rev. B **75**, 195421 (2007).

[259] S. Plimpton, J. Comp. Phys. **117**, 1 (1995).

[260] M. W. Mahoney and W. L. Jorgensen, J. Chem. Phys. **112**, 8910 (2000).

[261] H. Berendsen, J. Grigera, and T. Straatsma, J. Phys. Chem. **91**, 6269 (1987).

[262] J. Los and A. Fasolino, Phys. Rev. B **68**, 024107 (2003).

[263] G. Pérez-Hernández and B. Schmidt, Phys. Chem. Chem. Phys. **15**, 4995 (2013).

[264] O. Leenaerts, B. Partoens, and F. Peeters, Phys. Rev. B **77**, 125416 (2008).

[265] F. Costanzo, P. L. Silvestrelli, and F. Ancilotto, J. Chem. Theory Comput. **8**, 1288 (2012).

[266] P. L. Silvestrelli and A. Ambrosetti, J. Chem. Phys. **140**, 124107 (2014).

[267] S. S. Han and H. M. Lee, Carbon **42**, 2169 (2004).

[268] Z. K. Horastani, S. J. Hashemifar, S. M. Sayedi, and M. H. Sheikhi, Int. J. Hydr. Ener. **38**, 13680 (2013).

[269] A. White and J. F. Dobson, Phys. Rev. B **77**, 075436 (2008).

[270] A. J. Misquitta, J. Spencer, A. J. Stone, and A. Alavi, Phys. Rev. B **82**, 075312 (2010).

[271] V. Fthenakis, Renew. Sustainable Energy Rev. **13**, 2746 (2009).

[272] C. Tsai, K. Chan, J. K. Nørskov, and F. Abild-Pedersen, Catal. Sci. Tech. **5**, 246 (2015).

[273] Y. H. Li, P. F. Liu, L. F. Pan, H. F. Wang, Z. Z. Yang, L. R. Zheng, P. Hu, H. J. Zhao, L. Gu, and H. G. Yang, Nat. Commun. **6**, 1 (2015).

[274] B. Yang, R. Burch, C. Hardacre, G. Headdock, and P. Hu, ACS Catal. **4**, 182 (2013).

[275] R. Subbaraman, D. Tripkovic, K.-C. Chang, D. Strmcnik, A. P. Paulikas, P. Hirunsit, M. Chan, J. Greeley, V. Stamenkovic, and N. M. Markovic, Nat. Mater. **11**, 550 (2012).

[276] A. U. Nilekar, K. Sasaki, C. A. Farberow, R. R. Adzic, and M. Mavrĩkakis, J. Am. Chem. Soc. **133**, 18574 (2011).

[277] L. C. Grabow and M. Mavrikakis, ACS Catal. **1**, 365 (2011).

[278] A. Vojvodic and J. K. Nørskov, Science **334**, 1355 (2011).

[279] C. Tsai, K. Chan, J. K. Nørskov, and F. Abild-Pedersen, J. Phys. Chem. Lett. **5**, 3884 (2014).

[280] J. K. Nørskov, T. Bligaard, A. Logadottir, S. Bahn, L. B. Hansen, M. Bollinger, H. Bengaard, B. Hammer, Z. Sljivancanin, M. Mavrikakis, *et al.*, J. Catal. **209**, 275 (2002).

[281] A. Michaelides, Z.-P. Liu, C. Zhang, A. Alavi, D. A. King, and P. Hu, J. Am. Chem. Soc. **125**, 3704 (2003).

[282] R. Cortright, R. Davda, and J. A. Dumesic, Nature **418**, 964 (2002).

[283] X. Guo, G. Fang, G. Li, H. Ma, H. Fan, L. Yu, . C. Ma, X. Wu, D. Deng, M. Wei, *et al.*, Science **344**, 616 (2014).

[284] P. P. Shinde and V. Kumar, Phys. Rev. B **84**, 125401 (2011).

[285] S. Hu, M. Lozada-Hidalgo, F. Wang, A. Mishchenko, F. Schedin, R. Nair, E. W. Hill, D. Boukhvalov, M. Katsnelson, R. Dryfe, *et al.*, Nature **516**, 227 (2014).

[286] P. Cabrera-Sanfelix and G. R. Darling, J. Phys. Chem. C **111**, 18258 (2007).

[287] Y. Lin, F. Ding, and B. I. Yakobson, Phys. Rev. B **78**, 041402 (2008).

[288] D. Boukhvalov, M. Katsnelson, and A. Lichtenstein, Phys. Rev. B **77**, 035427 (2008).

[289] R. Balog, B. Jørgensen, L. Nilsson, M. Andersen, M. Rienks, Emile andB̃ianchi, M. Fanetti, E. Lægsgaard, A. Baraldi, S. Lizzit, *et al.*, Nat. Mater. **9**, 315 (2010).

[290] Ž. Šljivančanin, M. Andersen, L. Hornekær, and B. k. Hammer, Phys. Rev. B **83**, 205426 (2011).

[291] P. Merino, M. SÌŇvec, J. Martínez, P. Mutombo, C. Gonzalez, J. Martín-Gago, P. de Andres, and P. Jelinek, Langmuir **31**, 233 (2015).

[292] B. Wang and M.-L. Bocquet, J. Phys. Chem. Lett. **2**, 2341 (2011).

[293] B. Wang, S. Günther, J. Wintterlin, and M.-L. Bocquet, New J. Phys. **12**, 043041 (2010).

[294] J. Wintterlin and M.-L. Bocquet, Surf. Sci. **603**, 1841 (2009).

[295] J. G. Díaz, Y. Ding, R. Koitz, A. P. Seitsonen, M. Iannuzzi, and J. Hutter, Theor. Chem. Acc. **132**, 1 (2013).

[296] S. Altenburg, J. Kröger, B. Wang, M.-L. Bocquet, N. Lorente, and R. Berndt, Phys. Rev. Lett. **105**, 236101 (2010).

[297] M. Lattelais and M.-L. Bocquet, J. Phys. Chem. C **119**, 9234 (2015).

[298] X. Li, J. Feng, E. Wang, S. Meng, J. Klimeš, A. Michaelı̃des, *et al.*, Phys. Rev. B **85**, 085425 (2012).

[299] S. Joshi, D. Ecija, R. Koitz, M. Iannuzzi, J. Seitsonen, Ari P andH̃utter, H. Sachdev, S. Vijayaraghavan, F. Bischoff, K. Seufert, and ot hers, Nano Lett. **12**, 5821 (2012).

[300] R. F. Bader, *Atoms in molecules* (Wiley Online Library, 1990).

[301] G. Henkelman, A. Arnaldsson, and H. Jónsson, Comput. Mater. Sci. **36**, 354 (2006).

[302] E. O. Pyzer-Knapp, C. Suh, R. Gómez-Bombarelli, J. Aguilera-Iparraguirre, and A. Aspuru-Guzik, Annu. Rev. Mater. Res. **45**, 195 (2015).

[303] E. Pfeif and K. Kroenlein, APL Materials **4**, 053203 (2016).

[304] O. A. von Lilienfeld, Int. J. Quant. Chem. **113**, 1676 (2013).

[305] P. Geerlings, S. Fias, Z. Boisdenghien, and F. De Proft, Chem. Soc. Rev. **43**, 4989 (2014).

[306] O. A. Von Lilienfeld and M. E. Tuckerman, J. Chem. Phys. **125**, 154104 (2006).

[307] P. Geerlings, F. De Proft, and W. Langenaeker, Chem. Rev. **103**, 1793 (2003).

[308] R. Balawender, M. A. Welearegay, M. Lesiuk, F. De Proft, and P. Geerlings, J. Chem. Theory Comput. **9**, 5327 (2013).

[309] D. Sheppard, G. Henkelman, and O. A. von Lilienfeld, J. Chem. Phys. **133**, 084104 (2010).

[310] K. S. Chang, S. Fias, R. Ramakrishnan, and O. A. von Lilienfeld, J. Chem. Phys. **144**, 174110 (2016).

[311] A. Solovyeva and O. A. von Lilienfeld, arXiv preprint arXiv:1605.08080 (2016).

[312] P. W. Ayers, Faraday Discuss. **135**, 161 (2007).

[313] C. Cárdenas, W. Tiznado, P. W. Ayers, and P. Fuentealba, J. Phys. Chem. A **115**, 2325 (2011).

[314] J. Janak, Phys. Rev. B **18**, 7165 (1978).

[315] S. J. Bennie, M. W. van der Kamp, R. C. Pennifold, M. Stella, F. R. Manby, and A. J. Mulholland, J. Chem. Theory Comput. **12**, 2689 (2016).

[316] J. D. Goodpaster, T. A. Barnes, F. R. Manby, and T. F. Miller III, J. Chem. Phys. **140**, 18A507 (2014).

[317] P. Bygrave, N. Allan, and F. Manby, J. Chem. Phys. **137**, 164102 (2012).